# HIGH ENTROPY OXIDES (HEOs) FOR CHLORINE EVOLUTION REACTION

SUBASH KANDASAMY

MPhil

The Hong Kong Polytechnic University

2023

**The Hong Kong Polytechnic University**

**Department of Mechanical Engineering**

# High Entropy Oxides (HEOs) for Chlorine Evolution Reaction

**Subash Kandasamy**

**A Thesis Submitted in Partial Fulfilment of the Requirement for the Degree of Master of Philosophy**

**January 2023**

## CERTIFICATE OF ORIGINALITY

I hereby declare that this thesis is my own work and that, to the best of my knowledge and belief, it reproduces no material previously published or written, nor material that has been accepted for the award of any other degree or diploma, except where due acknowledgement has been made in the text.

**KANDASAMY, SUBASH**

# Abstract

This thesis reports the preparation and utilization of high entropy oxides in chlorine evolution reaction (CER) to increase the catalytic activity, chlorine selectivity and stability against corrosion in both concentrated and dilute chloride solutions. Single-phase, nanosized rutile structured high entropy oxides (HEO-R) containing five elements (Ru, Sn, Ti, V and Co) has been successfully synthesized through a one-step solvothermal method (180 °C), followed by calcination (350 °C - 700 °C) in air atmosphere. The synthesized material denoted as HEO-R-500 (calcination temperature=500 °C) displayed a single-phase rutile structure with affluent oxygen vacancies. The catalysts were coated on a carbon substrate and its activity was tested in acidic 5 M NaCl (pH=2) and dilute 0.5 M NaCl (pH=6) solutions. As a result, the HEO-R-500 delivered a high current density of 50 mA $cm^{-2}$ with a lower overpotential of 47 mV. In contrast, the commercial $RuO_2$-$TiO_2$ dimensionally stable anodes (DSA) required about 3 times higher overpotential value under the same testing conditions. The HEO-R-500 also exhibited a smaller Tafel value of 78.09 mV $dec^{-1}$ in 5 M NaCl solution (pH=2) and high chlorine selectivity in both acidic and dilute chloride solutions. The electrode delivered an excellent stability of 100 hours with a negligible increase in potential (0.9%) during the chronopotentiometry test at a current density ($j_{geo}$) of 50 mA $cm^{-2}$. Post-linear sweep voltammetry (LSV) tests revealed that there is no difference in the catalytic activity before and after the stability test. Overall, the HEO-R shows good electrocatalytic performance as anode in chlorine evolution reaction. The high catalytic activity and excellent stability are rooted in the confinement of five elements together in a single crystal lattice of the HEO.

## Acknowledgement

I would like to express my sincere gratitude to my chief supervisor Prof. Guohua Chen from the Hong Kong Polytechnic University for his valuable guidance and encouragement throughout my MPhil study. His kindness and support helped me to maintain a positive balance in both my work and personal life. I could not have succeeded without his guidance. I would like to express my gratitude to my co-supervisors, Dr. Qiang Liu and Dr. Liang An for supporting me in the completion of my study. I would like to thank my research group members (Dr. Xiaoliang Yu, Dr. Xusong Qin, Dr. Hassan Raza, Dr. Zhaowen Bai, Dr. Soumyadip Majumder, Dr. Zeqi Zhou, Dr. Man Wang, Miss Yutong Liu, Mr. Yinggang Zhu, Mr. Liang Hu, Miss Chuyi Xie, Mr. Qingsong Weng) for their generous support and friendship. Besides, I also would like to thank Mr. Benny CK Leung for his technical support in my research work.

My sincerest appreciation goes to my friends in the Fredrick's family, seniors and all the professors during my bachelor's study from CSIR-CECRI. I would like to thank my parents, my brother, and all other family members for their love, support and understanding.

Table of Contents

# List of Figures

# List of Tables

# Nomenclature

| | |
|---|---|
| ACC | Active chlorine content |
| AST | Accelerated stability test |
| CC | Carbon cloth |
| CER | Chlorine evolution reaction |
| CF | Crack-free |
| CNT | Carbon nano tubes |
| CV | Cyclic voltammogram |
| DEMS | Differential electrochemical mass spectroscopy |
| DFT | Density functional theory |
| DPD | n, n - diethyl-p-phenylenediamine |
| DSA | Dimensionally stable anodes |
| ECSA | Electrochemically active surface area |
| EDS | Energy dispersive spectroscopy |
| EIS | Electrochemical impedance spectroscopy |
| FE | Faradaic efficiency |
| FTO | Fluorine doped tin oxide |
| HAADF | High-angle annular dark field |
| HEO | High entropy oxide |
| HEO-R | High entropy rutile oxide |
| HER | Hydrogen evolution reaction |
| HRTEM | High resolution transmission electron microscopy |

| | |
|---|---|
| H-UPD | Hydrogen underpotential deposition |
| ICO | Iridium doped cobalt oxide ($IrO_2$-$Co_3O_4$) |
| LC | Less crack |
| LSV | Linear sweep voltammetry |
| MC | Mud-crack |
| MMO | Mixed metal oxides |
| MWCNT | Multi-walled carbon nano tubes |
| NSA | Nanostructured arrays |
| OER | Oxygen evolution reaction |
| ORR | Oxygen reduction reaction |
| RC | Reduced crack |
| RHE | Reversible hydrogen electrode |
| SAED | Selected area diffraction pattern |
| SCV | Scanning cyclic voltammetry |
| STEM | Scanning transmission electron microscopy |
| TEM | Transmission electron microscopy |
| TOF | Turnover frequency |
| XANES | X-ray absorption near-edge spectroscopy |
| XPS | X-ray photoelectron spectroscopy |
| XRD | X-ray diffraction |

# Chapter 1. Introduction

## 1.1 Background of electrocatalysis

The electrochemical production of chemicals is of great importance in considering the increased $CO_2$ emissions from the industries. The process of electrolysis involves applying electric charges to electrodes immersed in an electrolyte, a conductive medium and produces valuable chemicals as a result of the exchange of electrons between the electrode and the electrolyte. Typical examples are $Cl_2$ and $H_2$ production[1].

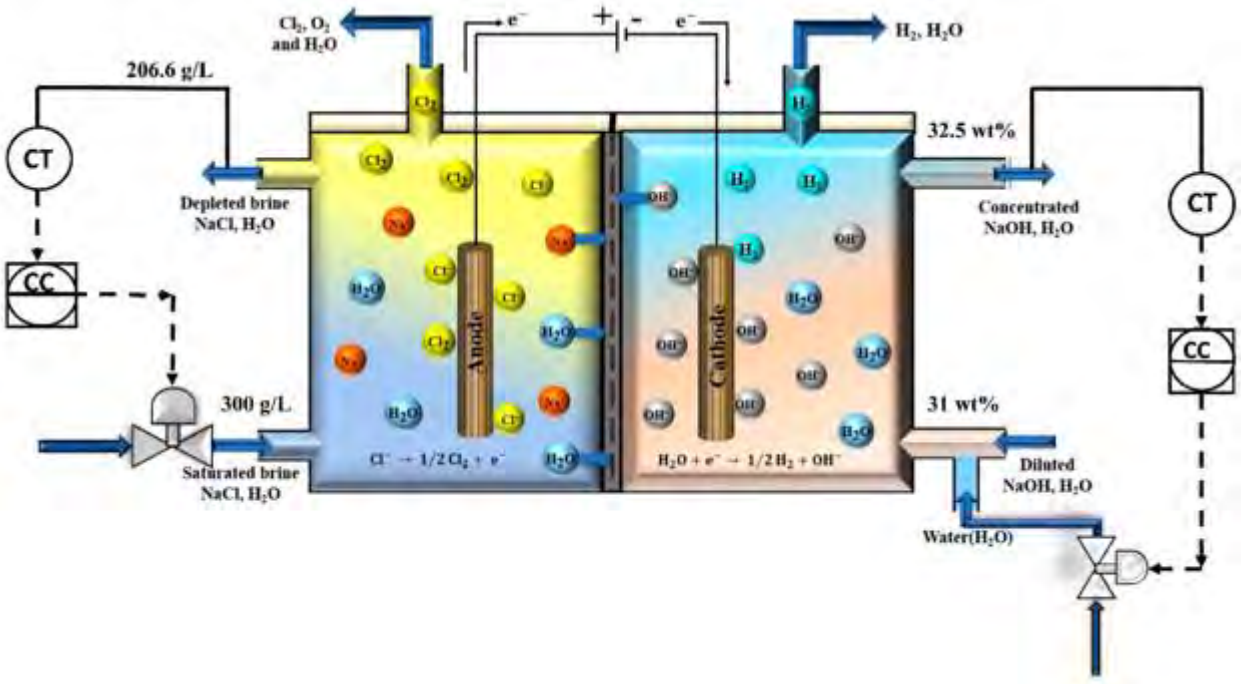


Figure 1.1: Schematic representation of chlor-alkali production. Reproduced with permission[2]. Copyright 2022, Multidisciplinary Digital Publishing Institute.

Among the electro-synthesized compounds, chlorine ($Cl_2$) is an indispensable ingredient in numerous industrial processes, including wastewater treatment[3-5], medicines[6, 7], disinfectants[8, 9], defense[7], and polymer/plastic synthesis[10], among others. The electrolytic generation of

chlorine ($Cl_2$) and sodium hydroxide (NaOH or caustic soda) began in 1888 and remained as one of the essential electrochemical processes, accounting for >97% of the world's chlorine production, consuming >150 TWh of electricity annually (**Figure 1.1**)[11]. Currently, the chlor-alkali industries use dimensionally stable anodes (DSA) because of their high selectivity and stability with a service life of more than four years. Although the selectivity and stability of DSA are high, their activity is low, resulting in increased energy consumption. It is thus, high operating voltage and temperature (>80 °C) are applied to the electrochemical reactor to meet the manufacturing demand[12]. Hence, it is vital to design and create an energy-efficient catalytic system due to the considerable operating costs associated with the electricity consumption. Even a 1% decrease in energy consumption will significantly affect cost savings[1, 10, 11, 13].

In addition to the industrial chlorine production, the presence of chloride ions in seawater represents an alternative supply of inexpensive reactants for chlorine oxidation reactions. By oxidizing the chloride ions present in the seawater or wastewater to free chlorine, on-site water disinfection and organic matter removal could be performed with reduced chemical and operational expenses[14, 15]. Apart from this, the electro-chlorination of seawater is also advantageous for the hydrogen-chlorine regenerative fuel cell on a wide scale[16, 17]. However, the presence of low chloride content, high pH(~8), and the impurities in seawater increases the overpotential of the reaction, which allows parasitic reactions such as oxygen evolution reaction (OER) to occur and also causes system failure through corrosion of anodes[13]. Even though a variety of approaches have been made to increase the performance of these anodes through changes in chemical compositions, morphology, and crystal structure, they are still not capable of replacing the typical $RuO_2$-$TiO_2$ or $RuO_2$-$IrO_2$-$TiO_2$ DSA's[11]. This is either because of their complicated manufacturing process incurring huge cost or as a result of failure in satisfying one of the following

factors, such as selectivity, stability, and activity. Therefore, searching for new anodes is a continuous effort, globally looking for materials with low overpotential for electrochemical redox reactions and high stability in harsh operating conditions.

Recently high entropy materials have been actively explored in hydrogen evolution reaction (HER) and oxygen evolution reaction (OER) because of their excellent catalytic activity and stability against corrosion. Random mixing of five or more elements and confining them in a single lattice in the HEOs, can lower the overall activation energy required in the electrochemical reactions. The physical, chemical, and electrochemical properties of the HEOs can be tuned by altering the elements used and their stoichiometry[18]. The incorporation of five or more cations with different atomic radii in the same lattice site creates a lattice constraint that induces more active sites on the surface including oxygen vacancies [18-20]. As oxygen defects play an important role in enhancing the activity of a catalyst, creating and controlling those defects in high entropy materials will be very useful for increasing the activity of anodes in chlorine evolution reaction (CER)[3]. Although the HEOs are structurally equivalent, the functions of the randomly distributed metal cations vary because some cations function as active sites where others act on modulating the electronic structure, which could be advantageous in catalytic reactions [18-22]. Additionally, the varying diffusion rate of the metal cations in the HEOs increases the phase stability of the catalyst that could be beneficial over the conventional DSAs[21]. However, high entropy oxides (HEOs) have never been studied for chlorine evolution reaction yet. Thus, this work would focus on designing energy-efficient anode materials based on high entropy systems for electro-chlorination, aiming to achieve an enhanced efficiency compared to typical DSAs.

## 1.2 Objectives.

This research aims to fabricate a highly stable anode with increased activity for electro-chlorination systems using a high-entropy oxide catalyst.

Nanosized single-phase high entropy oxide (HEO) materials based on rutile (HEO-R) structure will first be fabricated by solvothermal synthesis. The HEO will then be assessed for chlorine generation in both industrial 5 M NaCl solution (pH=2) and dilute 0.5 M NaCl (pH=6) solution. Highly concentrated 5 M NaCl solution is used in industrial conditions because the selectivity for $Cl_2$ gas increases with an increase in $Cl^-$ concentration, and >97% selectivity was measured when 4 M NaCl solution was used. In membrane cells, the concentration of NaCl in the feed brine is about 300 g $L^{-1}$. The pH value is maintained at ~2 because pH <2 can likely dissolve the Ti and metal elements. When the pH is >2, the oxygen evolution reaction's selectivity increases and dissolution of anodes occurs under alkaline conditions[12, 23]. For dilute chloride solutions, 0.5 M NaCl is chosen considering of the lower concentration of [$Cl^-$] = 0.5 M and higher pH of 8 in the sea water[14]. However, the pH value is maintained at 6 in this work instead of 8 to avoid the corrosion of the carbon substrate[24, 25]. Based on the above discussion, the following objectives are to be achieved:

1. To synthesize single phase and nanosized high entropy rutile oxides using solvothermal synthesis.
2. To achieve very high catalytic activity, enhanced service life, and high selectivity in acidic (5 M NaCl, pH =2) and dilute chloride (0.5 M NaCl, pH=6) solutions at a very low overpotential compared to the control sample.

# Chapter 2. Literature Review

## 2.1 Background of chlorine evolution reaction

Electrocatalysis is the process of enhancing the formation of new chemicals from the reactant material with a catalyst by passing electric charge (Q) to electrodes immersed in a reactant medium called electrolyte, where electron transfer occurs through the oxidation (+'ve) and reduction (-'ve) of the interested species via adsorption/desorption steps. Oxidation refers to the loss of electrons from the reactant at the anode, whereas reduction refers to the gain of electrons by another reactant at the cathode. The above reactions are performed in an electrochemical cell called the electrolysers. Therefore, the amount of electrical energy consumed is exactly proportional to the quantity of products obtained, which determines the efficiency of the process according to **Eq.2.1**.

$$Q = nFm/M \qquad \textbf{2.1}$$

Where,

Q = Electric charge, coulombs, C

n = The total number of electrons transported per reactant molecule or atom.

m = The mass of the electrochemically produced product, Kg.

F = Faraday's constant, equal to 96485.3 C $mol^{-1}$.

M = Molar mass of the reacting species, Kg $mol^{-1}$.

The activity, selectivity, and stability of an electrocatalyst are interrelated and are the three crucial parameters that determine its performance. Failure of an electrode to meet any of the aforementioned three requirements will result in unsatisfactory performance. Activity is the measurement of current density in relation to the applied overpotential. The selectivity is determined by the ratio of the faradaic current produced by chlorine generation to the total current

consumed during the electrolysis process. Lastly, stability denotes the service life of the electrode under the applied operating conditions.

The thermodynamic equilibrium potential of an electrode is quantified by the Nernst equation.(**Eq.2.2**):

$$E_0 = E_e^o + \frac{RT}{nF} \ln \frac{C_o^s}{C_R^s} \qquad \textbf{2.2}$$

Where,

$E_e$ = Equilibrium potential, V;

$E_e^o$ = Equilibrium potential under standard conditions, V;

R = Universal gas constant, 8.314 J $mol^{-1}K^{-1}$;

T = Temperature, K;

n = Total number of electrons transferred in the redox reaction;

F = Faraday's constant, 96485.3 C $mol^{-1}$;

$C_o^S$ = Surface concentration of oxidized product, mol $L^{-1}$;

$C_R^S$ = Surface concentration of reactant, mol $L^{-1}$.

## 2.2 Chlorine evolution reaction

Electrochemical chlorine evolution reaction (CER) is the process in which sodium chloride salt dissolved in water is used as the electrolyte (brine). The oxidation of $Cl^-$ at the anode releases chlorine gas (**Eq.2.3**) in conjunction with the reduction of $H^+$ at the cathode to form hydrogen gas (**Eq.2.4**) driven by the electrode potential via the following reactions:

Anodic reaction: $2Cl^- \longrightarrow Cl_2\ (gas) + 2e^-$ (1.356 V vs RHE) **2.3**

Cathodic reaction: $2H^{+} + 2e^{-} \longrightarrow H_2$ (gas) (0 V vs. RHE) **2.4**

Overall reaction: $2NaCl + 2H_2O \longleftrightarrow Cl_2 + H_2 + 2NaOH$ **2.5**

The membrane, diaphragm, and mercury cell electrolysis are the three essential two-electrode systems used in the chlor-alkali industrial processes[10]. The diaphragm cells were developed and operated from the early 1890s. In this cell, the diaphragm membrane made using asbestos fibre is used as a separator (**Figure 2.1**). Even though their energy consumption is lesser than the mercury cells, the diaphragm allows the brine to pass through the membrane from the anode compartment to the cathode compartment, contaminating the NaOH produced. Also, asbestos causes health issues like lung cancer[10, 12]. As a result, only 12.5% of the chlor-alkali industry uses diaphragm-based electrolysers until 2020.

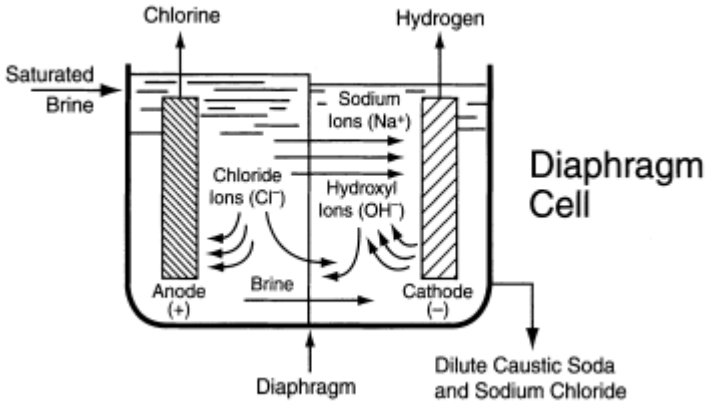


Figure 2.1. Schematic diagram of diaphragm chlor-alkali cells. Reproduced with permission[12]. Copyright 2005, Springer.

The mercury cells were designed in the late 1890s and dominated the chlor-alkali industry during the 20$^{th}$ century. In the mercury cells, sodium forms an amalgam with mercury after chlorine oxidation. Then, it is transported to another reactor, where it is decomposed into $H_2$ gas and NaOH

by reacting with water (**Figure 2.2**). However, because of environmental contamination and mercury poisoning, the mercury-based chlor-alkali industries have been phased out[10, 12].

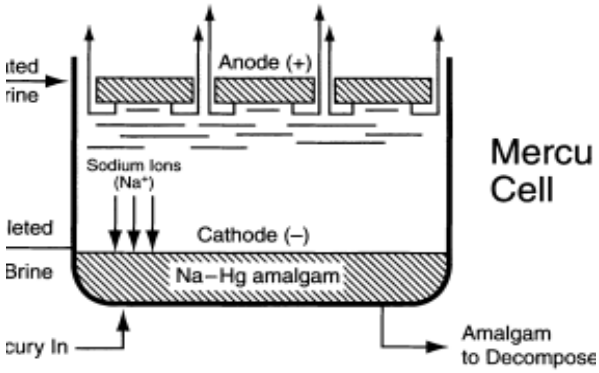


Figure 2.2: Schematic diagram of mercury chlor-alkali cells. Reproduced with permission[12]. Copyright 2005, Springer.

The membrane cells were developed by modifying the diaphragm cell by replacing the asbestos fiber with permselective membranes in the 1940s (**Figure 2.3**). It was commercialized after introducing perfluorinated ion exchange membranes called Nafion, which have enhanced ion-exchange properties, less energy consumption, and high resistance against corrosion under harsh operating conditions.

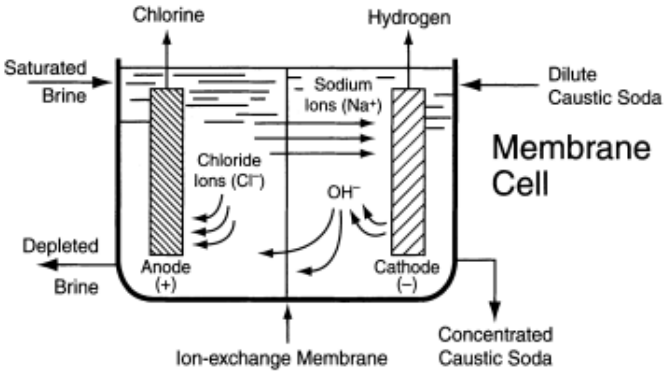


Figure 2.3: Schematic diagram of membrane chlor-alkali cells. Reproduced with permission[12]. Copyright 2005, Springer.

Two types of membrane electrolysers are available, monopolar, and bipolar. The monopolar electrolysers are operated at high amperage and low voltage and vice-versa for the bipolar electrolysers. However, the caustic efficiency of the perfluorinated membranes was less because of the back-migration of the $OH^-$ ions from the cathode to the anode compartment. To overcome this, the asymmetric membranes were designed, containing perfluoro-sulfonate polymer on the anode side and perfluoro-carboxylate polymer on the cathode side resistive for caustic migration. Almost 83% of the chlor-alkali industry uses the membrane electrolysis approach because of its less energy consumption, high efficiency, and high product purity[10, 12].

With the widespread usage of membrane electrolysis, the estimated annual power consumption is 150 TWh[11]. Therefore, the parameters mentioned in **Table 2.1** are optimized to achieve a very high selectivity of $Cl_2$ by circumventing oxygen evolution reactions (OER). OER is a parasitic reaction that causes an increase in electricity consumption by compromising the purity of the $Cl_2$ gas because of its low equilibrium potential than CER, and it proceeds through the following reaction (**Eq.2.6**).

$$2H_2O \rightarrow O_2 + 4H^+ + 4e^- \qquad \textbf{2.6}$$

Table 2.1. Typical operating conditions for chlor-alkali production in membrane processes[1, 12].

| | |
|---|---|
| Cell Voltage (V) | 2.4 – 2.7 |
| Applied current density ($kAm^{-2}$) | 1.5 – 7 (Usually 400 mA $cm^{-2}$) |
| Temperature (°C) | 80 – 90 |
| NaCl concentration in the analyte (g $L^{-1}$) | 200 – 300 |
| Analyte pH | 2 – 4 |
| NaOH concentration in the catholyte | 30 – 40% |

However, the oxygen gas produced reduces the effectiveness of chlorine production and causes the anode material to degrade by corrosion. By using electrodes that selectively adsorb chloride ions, chlor-alkali processes can reach a faradaic efficiency close to 99%[26]. The chloride ions release electrons to the anode as a result of their oxidation at the anode surface, which in turn is consumed by the $H^+$ ions on the cathode surface, producing hydrogen gas ($H_2$ gas) and precipitation of sodium hydroxide (NaOH) in the cathode compartment. The chlor-alkali industry currently utilizes ruthenium-based Mixed Metal Oxides (MMO) as anodes because of their high electronic conductivity and tendency to operate at industrial current densities with high selectivity and a service life of more than ten years[1, 12]. Nickel plates are used as cathodes for hydrogen evolution reaction (HER) because of their resistivity towards corrosion in concentrated alkali solutions[12].

### 2.2.1 Reaction mechanisms

Even though the CER is a simple two-electron transfer reaction, the in-depth understanding of the reaction mechanism is very limited because of the lack of in situ-spectroscopic studies to probe the reactant intermediates during the reaction. First principle calculations using DFT calculations primarily focused on investigating the CER on the rutile oxides[1, 10, 11]. To date, only the following three mechanisms, which are derived, based on the kinetics of CER, have been proposed and accepted.

#### 2.2.1.1 Volmer-Tafel mechanism

In step (I), the chloride ions in the brine bind to two adjacent active sites in the catalyst layer (**Eq.2.7**), indicated as the Volmer step. Then the two adsorbed chloride ions combine and evolve as a chloride molecule (**Eq.2.8**) known as the Tafel step[27, 28].

S* Active site for chlorine ions in the catalyst.

Step (I) $$2S^* + 2Cl^- \rightarrow 2Cl^* + 2e^-$$ **2.7**

Step (II) $$2Cl^* \rightarrow 2^* + Cl_2$$ **2.8**

### 2.2.1.2 Volmer-Heyrovsky mechanism

In the Volmer-Heyrovsky mechanism [27, 29], same as the previous one, the chloride ion gets adsorbed in the Volmer step (**Eq.2.9**). Then, in the second step, another chloride ion binds to the adsorbed chloride ion and turns into a chlorine molecule (**Eq.2.10**).

S* Active site for chlorine ions in the catalyst.

Step (I) $$S* + Cl^- \rightarrow Cl^* + e^-$$ **2.9**

Step (II) $$Cl^* + Cl^- \rightarrow S* + Cl_2 + e^-$$ **2.10**

### 2.2.1.3 Krishtalik mechanism

Similar to the Volmer-Heyrovsky, the Krishtalik mechanism also requires only one active site to produce one $Cl_2$ molecule[27, 30]. After the adsorption of the chloride ion in the first step (**Eq.2.11**), it forms a chloronium ion by losing an electron in the second step (**Eq.2.12**) followed by the recombination with another $Cl^-$ ion from the electrolyte and evolves as $Cl_2$ (**Eq.2.13**).

S* Active site for chlorine ions in the catalyst.

Step (I) $$S* + Cl^- \rightarrow Cl^* + e^-$$ **2.11**

Step (II) $$Cl^* \rightarrow Cl^* + e^-$$ **2.12**

Step (III) $$Cl^* + Cl^- \rightarrow * + Cl_2$$ **2.13**

Different reaction mechanisms occur depending on the catalyst structure. In the above three mechanisms, the Volmer-Heyrovsky mechanism is being reported for most of the oxide catalysts (Rutile) in CER.

### 2.2.2 Mechanism of parasitic oxygen evolution reaction

In the oxygen evolution reaction, $O_2$ gas and $H^+$ ions are generated in the anodic compartment as a result of water oxidation on anode surface at a thermodynamic potential of 1.23 V vs. RHE[31, 32]. While the CER proceeds via 2-electron transfer process, the OER is a four-electron transfer process, resulting in poor kinetics. The commonly accepted reaction pathway is as follows:**Alkaline oxygen evolution.**

S* Active site for $O^-$, $OH^-$, and $OOH^-$ intermediates.

| | | |
|---|---|---|
| Step (I) | $S* + H_2O \rightarrow OH^* + H^+ + e^-$ | **2.14** |
| Step (II) | $OH^* \rightarrow O^* + H^+ + e^-$ | **2.15** |
| Step (III) | $O^* + H_2O \rightarrow OOH^* + H^+ + e^-$ | **2.16** |
| Step (IV) | $OOH^* \rightarrow S* + O_2 + H^+ + e^-$ | **2.17** |

#### 2.2.2.2 Alkaline oxygen evolution.

S* Active site for $O^-$, $OH^-$, and $OOH^-$ intermediates.

| | | |
|---|---|---|
| Step (I) | $S* + OH^- \rightarrow OH^* + e^-$ | **2.18** |
| Step (II) | $OH^* + OH^- \rightarrow O^* + H_2O + e^-$ | **2.19** |
| Step (III) | $O^* + OH^- \rightarrow OOH^* + e^-$ | **2.20** |
| Step (IV) | $OOH^* + OH^- \rightarrow S* + O_2 + H_2O + e^-$ | **2.21** |

### 2.2.3 Electrochemical measurement criteria for catalytic activity

The kinetics of chlorine evolution was measured over $RuO_2$ electrodes and suggested that the kinetics of CER is not affected by the change in pH of the brine[33]. **Figure 2.4** compares the measured logarithmic value of current density (log j (mA) $cm^{-2}$) vs. pH.

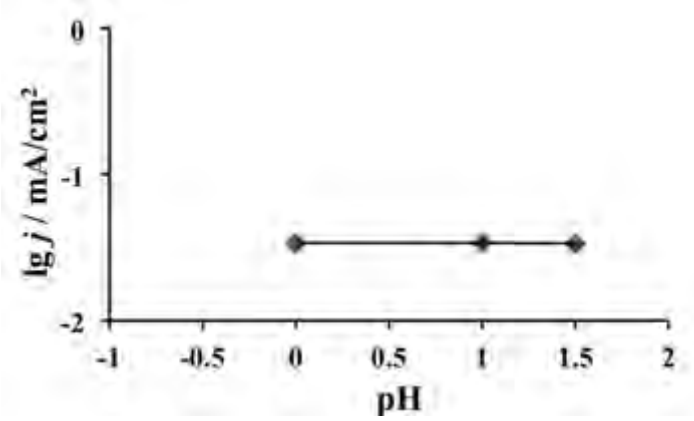


Figure 2.4: Kinetics of CER over $RuO_2$ (110) / Ru (0001) at U = 1.34 V vs. SHE and T = 25°C. Reproduced with permission[33]. Copyright 2017, American Chemical Society.

However, the activity of OER depends on the pH of electrolyte because the equilibrium potential of OER decreases by a factor 0.059 eV per pH. An increase in pH reduces the equilibrium overpotential of the OER, shifting the selectivity of chlorine evolution to oxygen evolution[25, 26, 34]. Thus, the reversible hydrogen electrode (RHE) scale is adopted while determining the equilibrium potential of the CER using the Nernst equation (**Eq.2.22**) that considers the pH, concentration of the NaCl, temperature, and partial pressure of the electrolyte.

$$E_{CER}\ \text{vs RHE} = E^0_{CER} - \frac{RT}{F}.\ln a\ (Cl^-) + \frac{RT}{2F}.\ln a\ (Cl_2) \qquad \textbf{2.22}$$

The following equation is used to calculate The $E^O_{CER}$ under standard conditions,

$$E^0_{CER} = \left(1.358\ V - \frac{RT}{F}.\ 2.303\ .pH\right) - (\ 0.001248\ \frac{dv}{dk}).(T - 298.15\ K) \qquad \textbf{2.23}$$

Where, $E^{O}_{CER}$ = Electrode potential under standard conditions (V), R = the universal gas constant (8.314 J $mol^{-1}$ $K^{-1}$), T = Temperature (K), F = Faraday's constant (96485.3 C $mol^{-1}$), a($Cl^-$) = concentration of the NaCl in the electrolyte (mol $L^{-1}$), a($Cl_2$) = partial pressure of evolving $Cl_2$ (0.01).

In the past decades, several methods have been developed and designed to evaluate catalytic performance related to the activity, selectivity, and stability. Some of the widely accepted and followed critical parameters are Overpotential (η), Tafel slope, Chronopotentiometry or Chronoamperometry (Stability test), Faradaic efficiency (FE), Electrochemically active surface area. They are discussed in more details subsequently.

#### 2.2.3.1 Overpotential

Irrespective of the design of the process and the electrodes chosen, an excess potential from the thermodynamic equilibrium potential needs to be applied to overcome the intrinsic activation barrier to drive the electrocatalytic reaction, as the applied potential of 1.356 V in CER is same as that of the half-cell potential. When the potential is increased, the free energy of the product becomes negative, and the reaction proceeds. The positive deviation of applied excess potential ($E_e$) for anodic reactions like CER or negative deviation for cathodic reactions like HER from the thermodynamic equilibrium potential ($E_t$) is termed as the overpotential (η). Therefore, a catalyst with less overpotential and high current density are desired for any catalytic reaction.

Overpotential is the first, and the foremost parameter used to estimate the performance of the electrocatalyst by calculating the potential required to reach a fixed current density value from the transient voltammograms or the sampling cyclic voltammograms. The ideal potential value for the chlorine evolution reaction, oxygen evolution reaction, and hydrogen evolution reaction is

1.356 V, 1.23 V, and 0 V vs. RHE. The overpotential recorded can be classified into the following types: (i) Activation overpotential; (ii) concentration overpotential ($\eta_c$), and iii) resistance overpotential ($\eta_\Omega$). The **activation overpotential** depends on the intrinsic activity of a catalyst and can be tuned by optimizing the process of catalyst design. The decrease of active ionic species near the electrode surface during the electrochemical reaction causes the **concentration overpotential**. Maintaining stable electrolyte concentration by continuous flow or stirring can reduce the concentration overpotential. The increase in ohmic resistance due to the poor ionic conductivity of the electrolyte or poor contact between the electrode/catalyst interface causes the increase of **resistance overpotential** and can be compensated by subtracting the measured iR (current * ohmic resistance) value from the observed potential values. Connecting one catalyst particle to another is necessary for an efficient electron transfer and can be done by adding carbon additives. Therefore, the most important point of focus is the activation overpotential, an intrinsic property that determines the performance of a catalyst[35].

#### 2.2.3.2 Tafel slope

Tafel slope reveals the reaction kinetics for the electrocatalytic reactions such as CER, OER and HER, etc. The overpotential ($\eta$) and current density (j) measured from the transient polarization techniques such as linear sweep voltammogram (LSV) or cyclic voltammogram (CV), is plotted in terms of overpotential ($\eta$). vs. ($|j|$) and the linear portion of the obtained plot is used to calculate the Tafel values based on the following equation (**Eq.2.24**).

$$\eta = b \log |j| + a \qquad \textbf{2.24}$$

$\eta$ = Overpotential (mV), j = current density ( mA $cm^{-2}$), b = Tafel slope (mV $dec^{-1}$), and a = constant.

They reflect the kinetic process of the electrochemical reaction. For an electrode to perform well, it should exhibit a low Tafel slope, meaning less overpotential at very high current density[36-38].

#### 2.2.3.3 Electrochemically active surface area

The surface area obtained using the BET method cannot be used to calculate the electrochemically active surface area (ECSA) because not all the elements present in the catalyst will be active in the faradaic region under the electrolytic process. To find the active surfaces in an electrocatalyst for a specific electrochemical reaction, the double layer capacitance ($C_{dl}$) method, redox peak integration method, hydrogen underpotential deposition (H-UPD), and carbon monoxide (CO) stripping method can be used to determine the electrochemically active surface area. Among these methods, the double layer capacitance method is used in CER, a technique in which the measured double layer capacitance over the specific capacitance value of the electrode gives the electrochemically active surface area of the catalyst and is obtained by performing 5 – 10 cyclic voltammograms in the fixed voltage window in the non-faradaic region at different scan rates (10 – 200 mV $s^{-1}$). Increased active sites on the electrocatalyst results in larger $C_{dl}$ values. The ECSA normalized current density can be used to compare the intrinsic property of different catalysts[35, 39, 40].

#### 2.2.3.4 Stability

Another important parameter for evaluating an electrocatalyst for practical application is the long-term stability/durability tests such as chronopotentiometry (V vs. t) or chronoamperometry (i vs. t). These tests are performed for a period of time usually greater than 10 hours. If the overpotential is stable or within a 10% increase, the results suggests that the catalyst has excellent

stability making it a potential candidate for practical application. Usually, the chronopotentiometry test is suitable and widely adopted in which the overpotential value is monitored for a period of time over the applied current density. Continuous supply of reactants are necessary in diffusion limited reactions to maintain the potential constant[35].

#### 2.2.3.5 Faradaic efficiency

Faradaic efficiency (FE) is the calculation of the charge transfer efficiency of the electrons from the external circuit to the desired reaction products (chlorine).

It can be calculated using the following equation:

$$FE = n_{yield} / n_{theoretical} = n_{yield} \times it/zF \qquad \textbf{2.25}$$

Where i = applied current (A), t = time consumed (s), z = the number of electrons consumed per product (number of electrons in the CER = 2), and F = Faraday's constant (96485.3 C $mol^{-1}$).

## 2.3 Advances in the design of anodes for chlorine evolution reaction

In the initial days, platinum and graphite anode materials were used for chlorine production in the chlor-alkali industry. Considering the increase in cost and poor performance, new anode materials that are economical and high performing were needed. The revolution for new electrode materials for chlorine evolution reaction started in year 1956, when Beer Lambert introduced the insoluble titanium anodes coated with highly active platinum group metal oxides known as Dimensionally Stable Anodes (DSA). The titanium anodes were not able to be dissolved anodically, and when immersed in the electrolyte, they formed an insulating oxide layer on the surface, which is non-conductive to the electrolyte but conducive to other elements. It is thus, the titanium plates were coated with electrically and electrochemically active materials to improve

their performance. Once the conductive coating wears off, the protective insulating layer develops on the anode surface, preventing corrosion. Due to this intrinsic property, they are also called self-healing anodes.

Since commercialization in 1960s, the precious metals have been used in the chlor-alkali industry because of their high activity and selectivity towards chloride ions[41-43]. The platinum group metals were chosen because of their exceptional catalytic activity resulting in less overpotential close to the theoretical value, when operated at high current density. Initially, platinum and iridium were used as the electrocatalytic coatings, while later other low-cost platinum group metals came into existence. The dimensionally stable anodes are made by depositing a mixture of metal oxide (Example: $RuO_2$, $IrO_2$, $RhO_2$, $PbO_2$, etc.) on a conductive substrate, (Example: Titanium, FTO, and carbon paper) that act as catalytically active sites for chloride ions[1, 11, 24, 41-45]. However, the platinum group metal oxides usually suffer from the loss of catalytic activity through corrosion, causing the dissolution of metal oxides into the electrolyte. This dissolution not only reduces the service life of the anodes, but also incurs colossal maintenance costs.

To prevent the dissolution and promote the activity and stability of the catalyst, alloying with valve metals such as Ti, Zr, V, Sn, Nb, Ta, Nd and Sb, etc., has been carried out [44, 46, 47]. Also, the electronic and geometric factors play a crucial role in determining the electrocatalytic activity of the catalytic material. As the active materials and most of the valve materials share the same crystal geometry, they result in a solid solution promoting the durability of the catalyst over a long period of time. As the mixed metal oxides with less platinum group materials suffer from poor electrical conductivity, the anodes are designed with 10% to 30% of platinum group metals to overcome the poor electrical conductivity of the mixed metal oxides[1, 14].

In academic and industrial research, the most common and currently employed platinum group electrode material is $RuO_2$ and $IrO_2$, owing to their high activity in CER. Other metals such as Pt, Pd, and Rh are added in minimal quantities as dopants or additives to improve the electrocatalytic behavior of the anode[1, 11]. As a result, DSA containing a mixture of oxides was developed, which had an exceptional catalytic activity along with high selectivity and stability towards CER compared to all other elements[1, 12].

At the same time, with the aim of increasing the activity without increasing the cost of the anode, low-cost transition metal elements are being explored as potential catalysts for CER. Several low-cost, non-precious, abundantly available anode materials for chlorine evolution reaction have been developed such as $Co_3O_4$ (Spinel)[48], $CoSb_2O_{6-x}$ (Trirutile)[49], Single-atom catalysts[26] and perovskites[50], etc. However, the non-precious anodes suffer from high overpotential, and less activity compared to the precious metal like $RuO_2$. A periodic table listing the metals explored in the design of anodes for chlorine evolution reaction is given in **Figure 2.5**.


Figure 2.5: Elements used in the electrodes for chlorine evolution reaction. Reproduced with permission[11]. Copyright 2021, American Chemical Society.

Optimizing the properties of a catalyst to achieve high activity and selectivity with very less overpotential is a huge task. Both intrinsic properties and external parameters (temperature, brine concentration, flow rate, etc.) should be perfectly balanced for achieving high performance in CER. A short review of the recent advances in the design of anodes for chlorine evolution reaction is given below.

## 2.4 Anodes for chlorine evolution reaction

According to the Sabatier principle, the binding energy between the catalytic site and the reactant species should be optimized, where the catalyst and the reactant should be neither weakly nor strongly interacting, making it easy for the reactant to be adsorbed or desorbed from the catalyst surface. The free energy landscape (ΔG) between the catalyst and the reactant is estimated through the DFT calculations. For a two-electron transfer reaction like CER, there is only one reaction intermediate, whose free energy ($\Delta G_{RI}$) depends on the catalyst surface and should be in equilibrium ($\Delta G_{RI} = 0$) with the reactants and the products, as illustrated in **Figure 2.6**[51, 52].

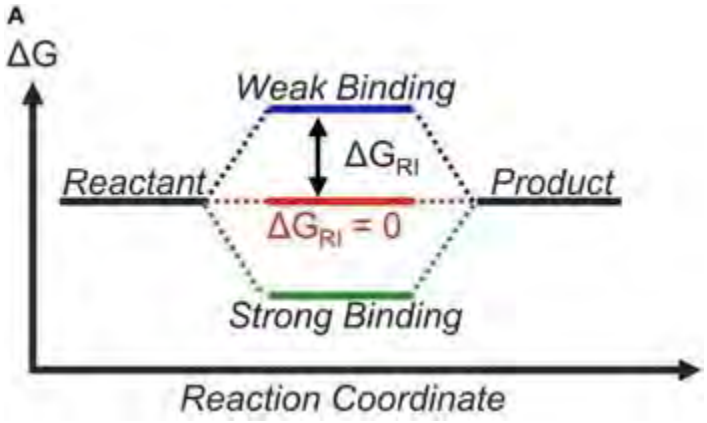


Figure 2.6: Free energy diagram for the reaction intermediate with the different binding strengths. Reproduced with permission[51]. Copyright 2021, Frontiers.

Based on this, a volcano plot can be derived and the catalyst with high affinity and optimal binding energy for the chloride ions will be present at the apex of the volcano curve. As all the reactions happen on the catalyst's surface, the electrochemical performance will be influenced by the pH, applied electrode potential, surface groups, and electrolyte composition [1, 11].

### 2.4.1 Precious metal anodes for chlorine evolution reaction

Almost, all the anodes for CER contain platinum group elements as catalysts owing to their high activity and less energy consumption compared to the other transition metal elements. Among the Pt group elements, Ru and Ir are mostly used because of their high affinity towards chloride ions comparing to others reactants (Example: $OH^-$)[1, 11, 53-55]. An overpotential-dependent volcano plot based on the oxygen binding energies on the catalyst surface for $Cl^-$ ions in CER is shown in **Figure 2.7**.

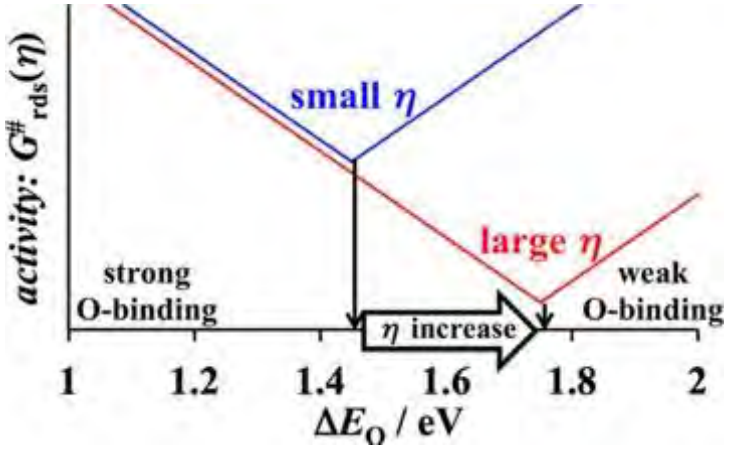


Figure 2.7: Overpotential dependent volcano plot. Reproduced with permission[56]. Copyright 2019, American Chemical Society.

For example, at high overpotential region, the oxygen binding energy on the surface of $RuO_2$ to $Cl^-$ is weaker resulting in superior performance, whereas $IrO_2$ is superior in the low overpotential region. As, $RuO_2$ has weaker oxygen binding energy at the high overpotential region $\eta_{CER} > 0.05$

V, it is considered as a suitable catalyst for forward reaction and $IrO_2$ is assumed to be superior in the backward reactions $\eta_{CER} < 0$ V, such as reduction of chlorine gas (**Figure 2.8**)[56, 57].

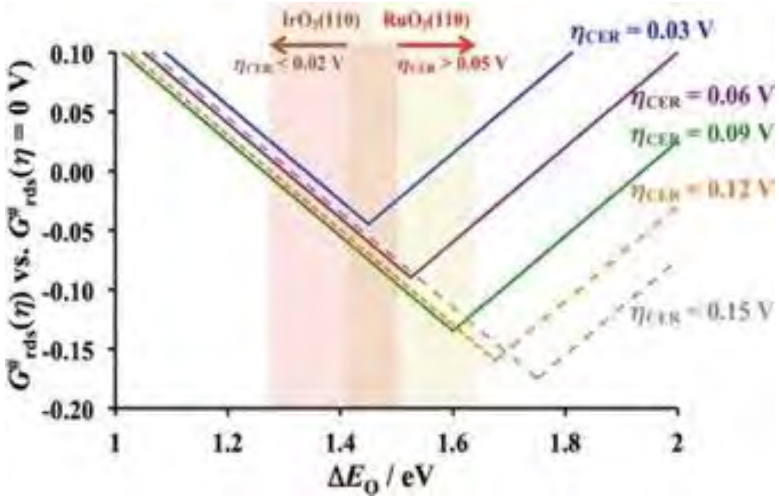


Figure 2.8: Overpotential dependent volcano plots constructed for $RuO_2$ and $IrO_2$. Reproduced with permission[56]. Copyright 2019, American Chemical Society.

Later in 2012, Zeradjanin and co-workers studied the adsorbents that are formed on the catalyst surface during CER by combining electrochemical techniques and Raman spectroscopy. Based on the observed characteristic Raman spectrum, an overpotential dependent volcano plot was constructed and the characteristic Raman peaks of $RuO_2$ is close to the Cl-O bond vibration near the apex of the volcano plot, compared to other oxides as shown in **Figure 2.9**[54]. The high affinity for chloride ions is because of the oxygen deficit nature, presence of more positive charges and smaller binding energy of chloride ions on the surface of $RuO_2$[58]. In addition to that, it was found that the solvent also plays an important role in the formation of a key intermediate for chlorine evolution reaction to occur, which is the formation of a hydrophilic layer that contains O-atoms. Almost all precious metal elements have high affinity for chloride ions comparing to non-precious catalysts[11, 54, 59]. The $RuO_2$ electrodes exhibited higher selectivity for $Cl_2$ compared to

$IrO_2$ in acidic 5 M NaCl solution, even though the electrochemically active surface area of $IrO_2$ was higher than $RuO_2$[58], which agrees with the theoretical calculations[56, 57].

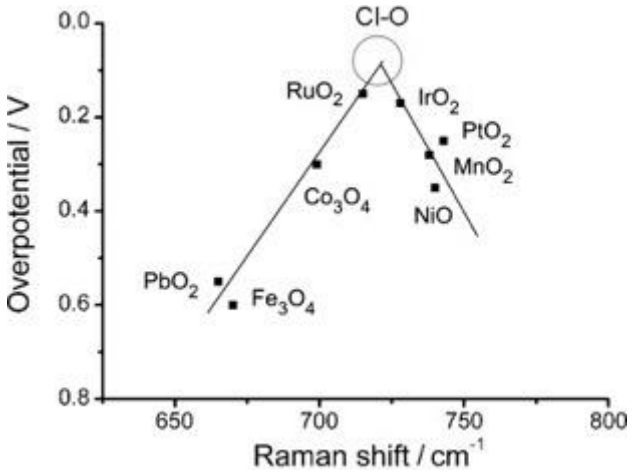


Figure 2.9: Overpotential dependent volcano plots as a function of Raman spectrum obtained. Reproduced with permission[54]. Copyright 2012, Wiley-VCH.

In addition to the above, most of the $RuO_2$-based MMO electrode made by the conventional thermal decomposition method contains only 20 to 40 % of $RuO_2$ in the MMO anode [11, 14, 46, 55, 60], because several studies have proven that the electrodes with less than 40 % $RuO_2$ exhibit higher selectivity for CER compared to 60 to 100 % $RuO_2$ in the composite due to its less electrochemically active surface area[60, 61]. Bune and co-workers measured the selectivity of chlorine evolution for a $RuO_2$-$TiO_2$ electrode in an acidic 4.27 M NaCl solution at a current density of 1.2 kA $m^{-2}$ and concluded that the selectivity increased as the percentage of Ru in the coating was decreased, while the opposite was experienced for oxygen evolution reaction. The volume percentage of oxygen gas as a function of Ru content in the $RuO_2$-$TiO_2$ coating is shown in **Figure 2.10**[1]. Further studies have proved that, the selectivity of $Cl_2$ for a $RuO_2$-$TiO_2$ DSA electrode is high, when the content of Ru is <30 %[1, 23, 62].

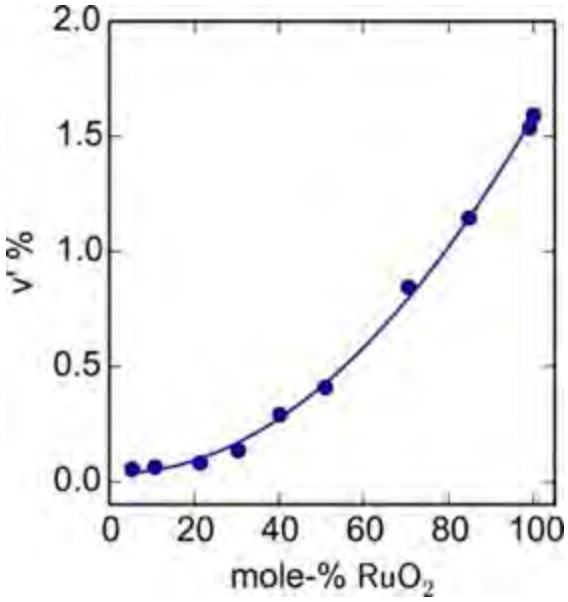


Figure 2.10: Oxygen content in the cell gas as a function of mole-% $RuO_2$ in a $RuO_2$-$TiO_2$ electrode. Reproduced with permission[1]. Copyright 2016, American Chemical Society.

The decrease in selectivity of $Cl_2$ with increase in Ru content is because of the decrease in the threshold potential of OER. In 1993, Takasu and co-workers measured the threshold electrode potential for CER and OER for a $RuO_2$-$TiO_2$ electrode made using thermal decomposition method in 1 M $H_2SO_4$ + 0.5 M NaCl solution. A less threshold potential of ~1.12 V vs. Ag/AgCl was needed for CER, while the OER threshold potential was 1.19 V vs. Ag/AgCl. When increasing the Ru content to 80%, the threshold potential for chlorine evolution decreased near 1.1 V vs Ag/AgCl along with the decrease in threshold potential for OER near 1.15 V vs. Ag/AgCl (**Figure 2.11**)[63].

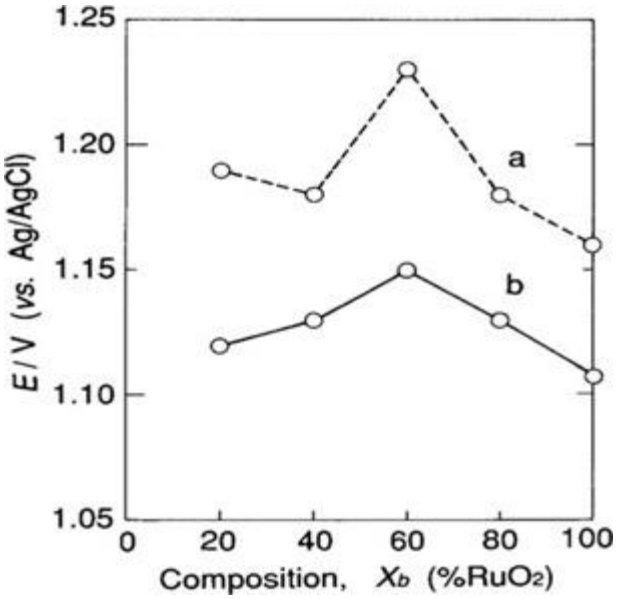


Figure 2.11: Threshold potentials for (a) chlorine and (b) oxygen evolution in 1.0 mol $L^{-3}$ + 0.5 mol $L^{-3}$ solution measured for electrodes with different Ru % in the $RuO_2$-$TiO_2$ coating. Reproduced with permission[63]. Copyright 1993, Elsevier.

The selectivity for $Cl_2$ over $O_2$ also depends on the amount of catalyst loading. When the catalyst loading increases, the activity for CER increases. But, the insufficient amount of chloride ions near the electrode surface oxidizes the OER reactants present in the electrolyte, thereby increasing the $O_2$ concentration in the cell gas[64, 65]. In 1998, Arikawa and co-workers, measured the selectivity between chlorine and oxygen gas using differential electrochemical mass spectroscopy (DEMS) for a $RuO_2$ coated Titanium (Ti) electrode with different loadings and the electrode with less loading of 0.1 to 0.2 mg $cm^{-2}$ has >95 % selectivity at low overpotential and ~90 % selectivity at high overpotential region for chlorine evolution compared to the higher oxide loadings that have <70 % selectivity as shown in **Figure 2.12**[25, 61].

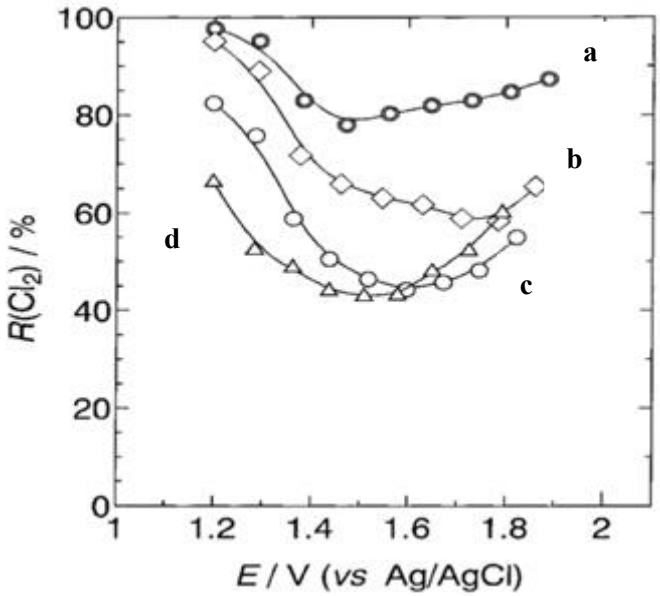


Figure 2.12: Ratio of chlorine evolution reaction as function of electrode potential in NaCl solution for 0.1 (a), 0.2 (b), 0.5 (c) and 0.9 (d) mg $cm^{-2}$ $RuO_2$ on Ti plate. Reproduced with permission[61]. Copyright 1998, Springer Nature.

The loss of the platinum group oxides during the electrolysis is too high due to corrosion of active sites. Especially, the service life of the pure $RuO_2$ electrode was poor because of the formation of volatile $RuO_4$, when the critical potential is reached[66, 67]. To increase the lifetime of these anodes, the stabilizing agents were added in the coating mixture. One or more metals, such as titanium, tantalum, zirconium, or niobium were added. However, titanium was primarily used because of the exceptional catalytic activity of $RuO_2$-$TiO_2$ anodes comparing to doping of other metals with $RuO_2$[11, 41-44].

#### 2.4.1.1 Effect of dopants on the catalytic performance of precious metal-based anodes.

Titanium is the most important and indispensable dopant in almost all the dimensionally stable anodes[68, 69]. The service life of $RuO_2$-$TiO_2$ DSA is better as compared to pure $RuO_2$ DSA,

because $TiO_2$ acts as a stabilizer in the composite and also alters the selectivity towards CER[69-73]. Studies have also proven that, even the DSA with less Ru content needs Ti to selectively catalyze the chloride ions[62]. As the electrodes with 20 % $RuO_2$ and 80 % $RuO_2$ in the $TiO_2$ based DSA's deliver similar activity, it is suggested that Ti also functions as an active catalyst layer for chlorine evolution reaction. This is due to the activation of the Ti sites by the Ru dopants[1, 69]. Using computational studies, it was found that the $TiO_2$ layer on top of $RuO_2$ has a significant effect on the chlorine selectivity and activity. For the $TiO_2$ monolayer on top of $RuO_2$, the O adsorption energy $\Delta E(O^c)$ was in the range of 2.7 eV to 4.2 eV (average $\Delta E(O^c)$ = 3.5 eV), which is closer to the optimum value of in the volcano plot (3.2 eV), exhibiting high selectivity. On the other hand, for the $RuO_2$ monolayer on $TiO_2$ was in the range of 1.1 eV to 1.6 eV (average $\Delta E(O^c)$ = 1.4 eV), not close to the optimum selectivity value. The Ti sites in the $TiO_2$ monolayer on $RuO_2$ might have been activated by the Ru doping[69]. Also, the $TiO_2$ layer on the top of $RuO_2$ blocks the intermediates of OER, thereby increasing the selectivity towards chlorine evolution reaction. Experimental studies have proved that a coating of single layer of $TiO_2$ increases the selectivity for chlorine evolution[74, 75].

Then the study was extended to find the optimal doping element in the rutile $TiO_2$ to achieve high activity and selectivity in chlorine evolution reaction. The optimal oxygen adsorption value $\Delta E(O^c)$ for chlorine evolution reaction was 3.2 eV. The calculated descriptor value for dopant in $TiO_2$ as an active site or Ti as an active site is shown in **Figure 2.13**. Based on the optimal descriptor value, the dopants that exhibit optimal activity and selectivity for CER, when doped in $TiO_2$ were Bi, Co, Ir, Mn, Pd, Ru, V, Pt and Ir[1, 68].

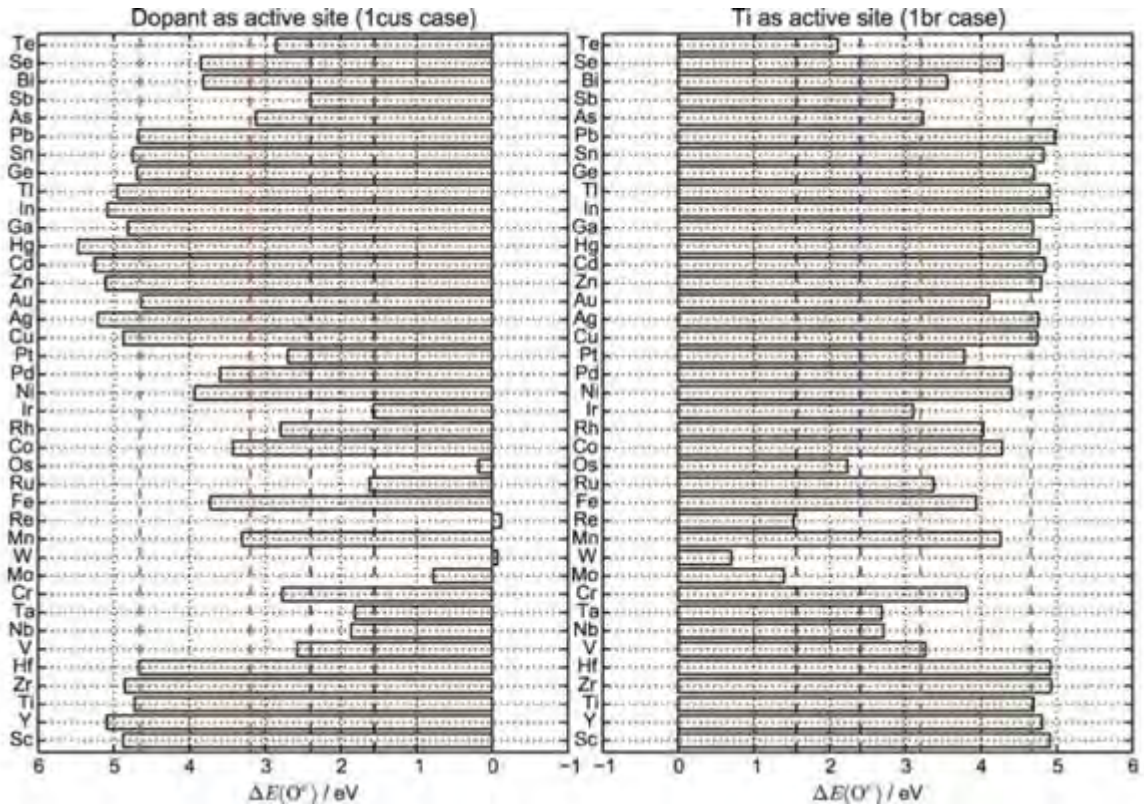


Figure 2.13: Descriptor value for doped $TiO_2$, where the dopants act as an active site (left) and when the Ti acts as an active site (right). Reproduced with permission[68]. Copyright 2015, Elsevier.

In 2018, Deng and co-workers prepared electrolyzed oxidizing water using $TiO_2$ doped $IrO_2$-$Ta_2O_5$ anode and studied the effects of varying $TiO_2$ content (10 %, 16 %, 24 %, and 34 %) on the activity, selectivity for CER and service life in dilute 0.1 M NaCl solution. The electrode was fabricated using thermal decomposition method at 550°C. SEM measurements showed that the compactness of the coating increased with increase in the % of $TiO_2$, in which the electrode with 30 % $TiO_2$ has less cracks and the opposite is observed for 10 % $TiO_2$ (**Figure 2.14 a**). CV measurements show that the activity increased with increase in $TiO_2$ (**Figure 2.14 b**), whereas the pure $IrO_2$ and $IrO_2$-$Ta_2O_5$ have lesser activity, suggesting that $TiO_2$ also participates in the electrochemical reaction. The selectivity for $Cl^-$ ions was measured by quantifying the amount of active chlorine content by applying 100 mA $cm^{-2}$ for 30 mins in 0.1 M NaCl solution (**Figure 2.14**

**c**). The $IrO_2$-$TiO_2$-$Ta_2O_5$ (34 % $TiO_2$) had produced 173.9 mg $L^{-1}$ of Chlorine, higher than the electrode without $TiO_2$ (90.2 mg $L^{-1}$). **Figure 2.14 (d)** depicts that, the service life of the electrode increased with the increase in the $TiO_2$ content with service life of 170 hours for 34 % $TiO_2$ electrode, comparing to the shorter service life of the DSA with no $TiO_2$ dopant. The effect of increasing the $TiO_2$ beyond 34 % was not discussed[76]. However, the obtained results agree with the computational calculations, that the addition of $TiO_2$ increases the catalytic activity and selectivity in CER[68].

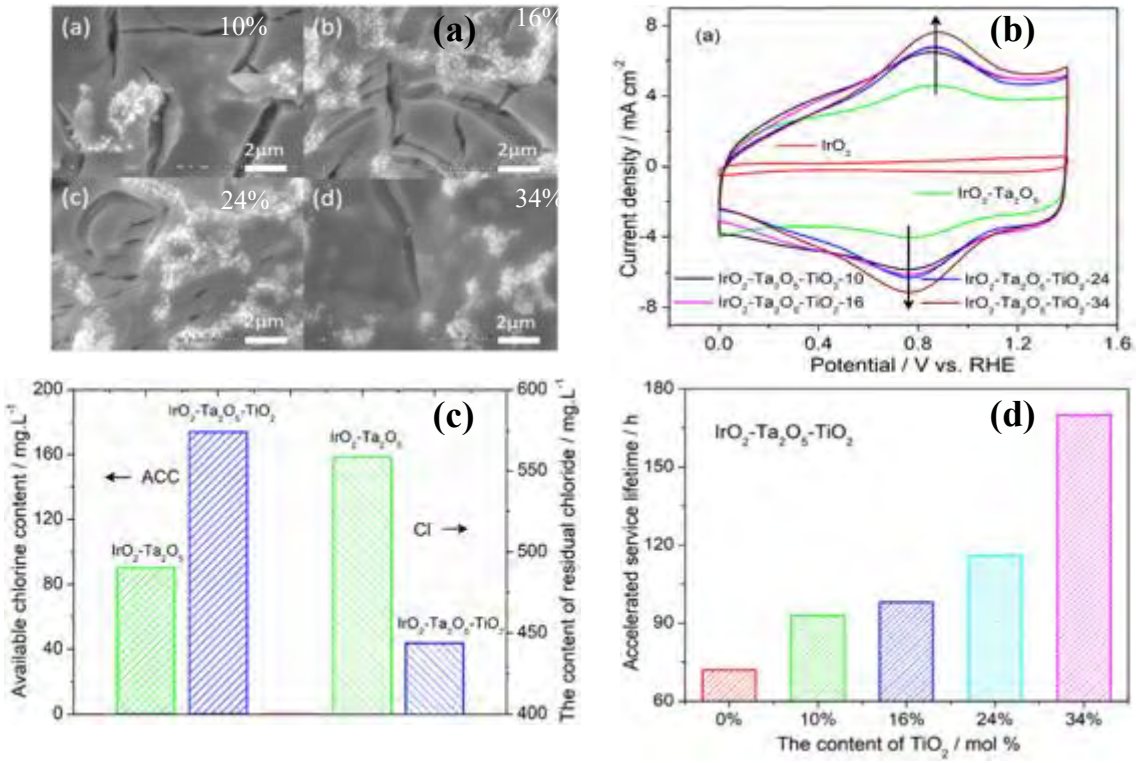


Figure 2.14: (a) Surface morphology of the DSA with varying $TiO_2$ content; (b) Cyclic voltammograms; (c) Total amount of ACC and remaining $Cl^-$ at 100 mA $cm^{-2}$ for 30 mins; (d) Accelerated service life of the DSA at 2000 mA $cm^{-2}$ at 40 in 0.5 M $H_2SO_4$ solution. Reproduced with permission[76]. Copyright 2019, Elsevier.

$SnO_2$ is another important element in the DSA fabrication, that has been added as a stabilizer and dispersion agent in the DSA's. At high pH value (pH>6), $RuO_2$ is susceptible for undergoing corrosion through oxidation of Ru (IV) to Ru (VIII) and becoming volatile[77]. This makes the coating get dissolved in the electrolyte and form an insulating $TiO_2$ layer when the Ti substrate comes in contact with the electrolyte. The insulating $TiO_2$ layer blocks the contact with the electrode coating and causes an sudden increase in overpotential as a result of the electrode failure[24]. The influence of $SnO_2$ on the electrocatalytic activity of $RuO_2$ (30 %)-$TiO_2$ (70 %) prepared using the thermal decomposition method for oxygen evolution in $HClO_4$ electrolyte was studied by Onuchukwu and co-workers in 1990. The $RuO_2$ content was kept constant and the $TiO_2$ content was varied with $SnO_2$. The surface charge q* was higher at >60 mC $cm^{-2}$ for $RuO_2$-$TiO_2$ with 20-40 % of $SnO_2$ and ~30 mC $cm^{-2}$ for 10 % and ~20 mC $cm^{-2}$ for 70 % $SnO_2$. The higher surface charge at 20-40 % of $SnO_2$ was because of the increased exposure of the Ru catalytic sites, but the results were contradictory with the activity measurements. The maximum activity is obtained for the electrode with 70 % $SnO_2$ and no apparent reasons were given. Also, the influence of $SnO_2$ on the service life of the electrodes were not studied[78].

Later in 2005, Chen and co-workers measured the electrocatalytic performance of $RuO_2$-$Sb_2O_5$-$SnO_2$ (12.2 % - 22.2 % - 65.6 %) in an acidic 3 M $H_2SO_4$ solution prepared using thermal decomposition method, by utilizing $SnO_2$ acts as a dispersing agent / stabilizer and $Sb_2O_5$ as a conductive agent. A compact coating was observed from the SEM measurements (**Figure 2.15 a**) and the ternary metal oxide coating had a service life time of 307 hours under a current density of 500 mA $cm^{-2}$ at 25 °C (**Figure 2.15 b**), and they reported that electrode service life was 15 times higher than the pure $RuO_2$[46]. Later, the effects of ruthenium content in $RuO_2$-$Sb_2O_5$-$SnO_2$ on the stability of the anode for OER in 3 M $H_2SO_4$ were studied by Li and co-workers in 2021. The

electrode with 30 % Ru content in the coating had a service life of 419 hours (25 °C) and 165 hours (70 °C) at 500 mA $cm^{-2}$ current density (**Figure 2.16 a**), whereas the electrode with 75 % Ru had poor service life of ~100 hours at 25 °C and ~30 hours at 70 °C (**Figure 2.16 b**)[60]. Even though less activity is obtained in coatings with less Ru content, the valve metal present in the composite was able to protect the anode from corrosion and extend the service life.

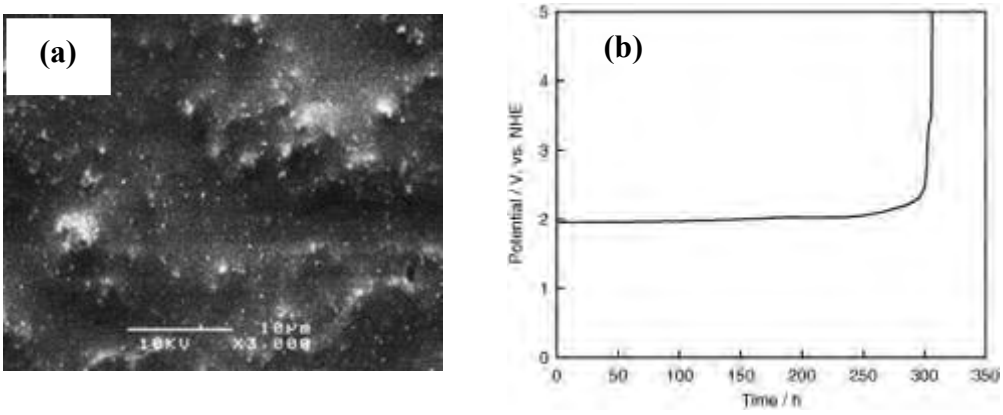


Figure 2.15: Service life of Ti/$RuO_2$-$Sb_2O_5$-$SnO_2$ electrode in 3 M $H_2SO_4$ at 500 mA $cm^{-2}$. Reproduced with permission[46]. Copyright 2005, Elsevier.

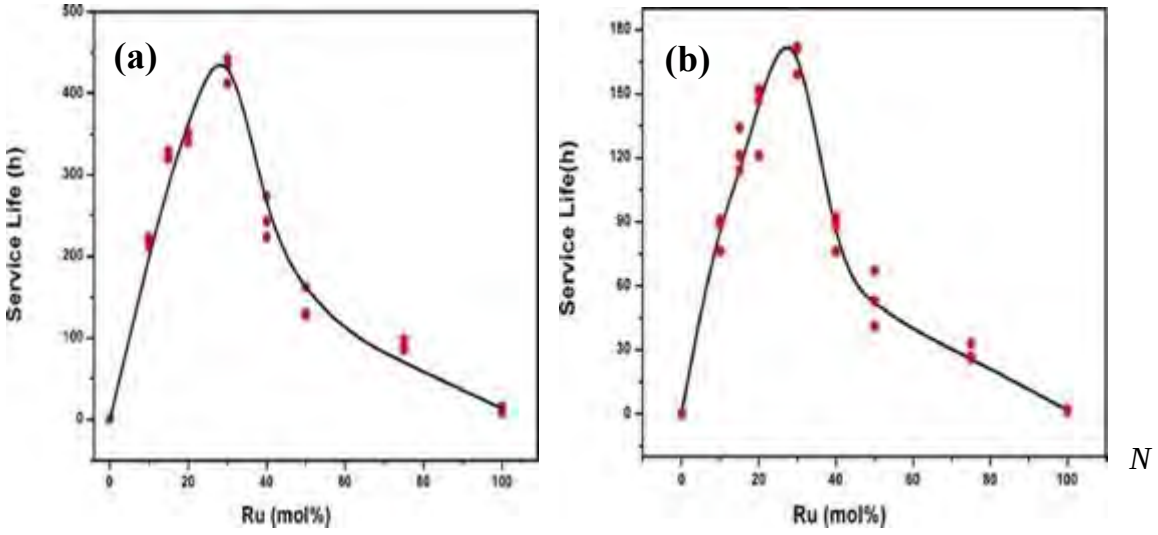


Figure 2.16: Comparison of service life $RuO_2$-$Sb_2O_5$-$SnO_2$ electrodes with varying Ru contents under 500 mA $cm^{-2}$ in 3 M $H_2SO_4$ solution at (a) 25 °C and (b) 70 °C. Reproduced with permission[60]. Copyright 2021, Elsevier.

The addition of $SnO_2$ not only increases the stability of electrode, but is also advantageous for improving the selectivity of chloride ions in CER because of its high OER overpotential comparing to CER [11, 79]. The activity of Ru doped $SnO_2$ film using the thermal decomposition method was measured for both oxygen evolution (1 M KOH solution at 30 °C) and chlorine evolution reaction (3 M NaCl solution at 30 °C). The anodic overpotential for oxygen evolution in the alkaline conditions was around 1.4 V, whereas the chlorine evolution reaction potential was around 1.0 V[80]. Later, the Ti/$RuO_2$-$Sb_2O_5$-$SnO_2$ was evaluated for seawater electro chlorination (0.5 M NaCl, pH=8) and the electrode had a current efficiency of 90 % at 25 mA $cm^{-2}$ current density and ~85 % at 100 mA $cm^{-2}$. The decrease in current efficiency at increased current density might be because of the lesser chlorine content. However, the electrode demonstrated an excellent service life of 266 hours at a current density of 1000 mA $cm^{-2}$ (35 °C). The service life of the electrode was estimated to be around five years at 50 mA $cm^{-2}$ current density [46]. Comparing the anode's activity in oxygen evolution and chlorine evolution, the electrode required ~1.6 V to reach 1000 mA $cm^{-2}$ in chlorine evolution, whereas in it required ~2 V to reach 500 mA $cm^{-2}$ in OER[46]. The increase in the threshold potential for oxygen evolution is due to the addition of $SnO_2$ because it is an n-type semiconductor with poor conductivity. The presence of $SnO_2$ might have weakened the OH* adsorption on the electrode surface, resulting in poor kinetics for OER. The reason for electrode failure after 250 hours might be because of the applied current density[14], where insufficient concentration of chloride ions near the electrode surface in alkaline electrolyte might have resulted in increased oxygen evolution, inducing the corrosion of the anodes[12].

There are very few non-precious transition metal oxides that are active for chlorine evolution, namely $Co_3O_4$, $Fe_3O_4$, $PbO_2$, NiO and $MnO_2$[81-85]. Among them, spinel $Co_3O_4$ was examined by several researchers due to their moderate activity and less cost. Ha and co-workers synthesized the

$Co_3O_4$ nanoparticles using the hot injection method with particle sizes in the range of 10 nm to 20 nm (**Figure 2.17 a**). They evaluated the electrochemical properties of $Co_3O_4$ in CER by combing Raman spectroscopy. High selectivity for CER over OER has been observed based on the LSV measurements in 0.6 M NaCl and 0.6 M $NaClO_4$ shown in **Figure 2.17 b**. The In-situ Raman spectrum illustrates that, when the potential reached 1.2 V, a new broad peak was has been observed at 502.6 $cm^{-1}$ due to the adsorption of the reaction intermediates of chlorine evolution reaction (**Figure 2.17 c**) but the band was absent for the oxygen evolution in the $NaClO_4$ electrolyte (**Figure 2.17 d**), confirming its high selectivity for chlorine evolution[86].

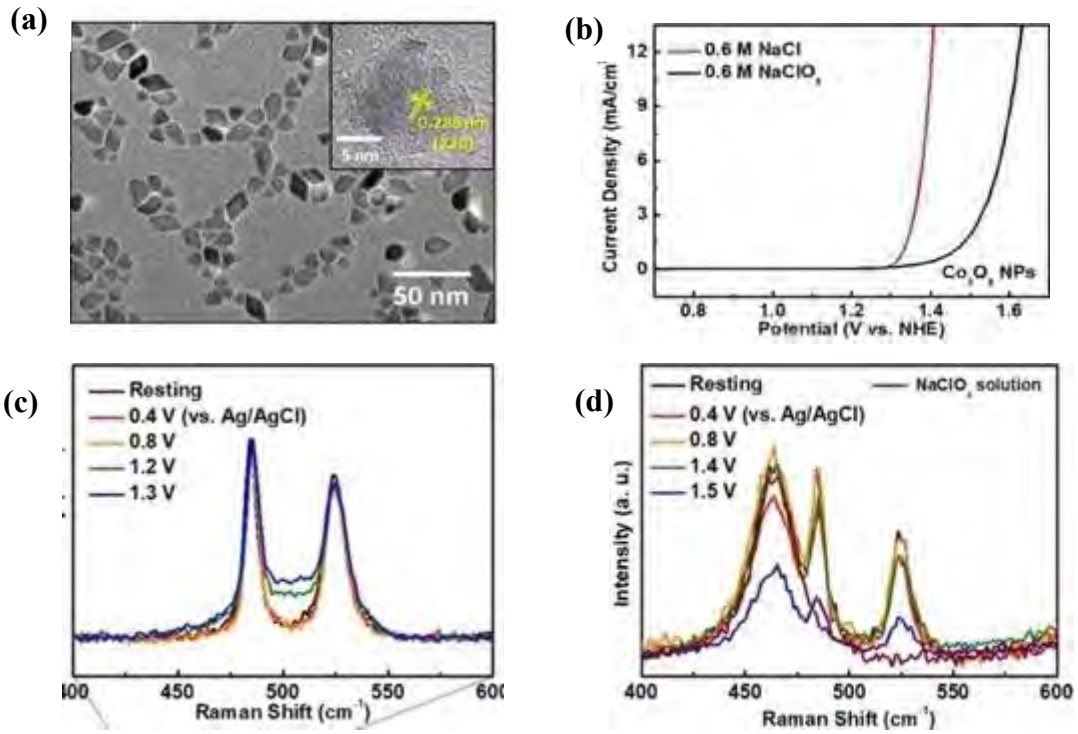


Figure 2.17: comparison of the polarization curves of $Co_3O_4$ nanoparticles in (a) 0.6 M NaCl; (b) 0.6 M $NaClO_4$ solution; (c) In situ Raman spectrum observed in the diluted chlorine solution during the active chlorine solution; and (d) Spectrum observed in the $NaClO_4$ solution for oxygen evolution reaction. Reproduced with permission[86]. Copyright 2019, American Chemical Society.

Addition of a platinum group element with a co-catalyst, that has poor OER kinetics is an attractive strategy for increase the selectivity and stability of the electrodes used in CER. Therefore, mixed coatings were fabricated with precious metal oxides such as $RuO_2$ or $IrO_2$ and were evaluated based on their structure, composition, and electrochemical properties[11, 87]. More recently, Han and co-workers prepared the $IrO_2$-$Co_3O_4$ (ICO) anode with less than >3 % $IrO_2$ and tested it for chlorine evolution reaction in both 2 M NaCl and diluted 10 mM NaCl solutions. The electrode performed well in the 2 M NaCl solution with early onset potential around ~1.75 V, and increased overpotential of 55 mV for OER in 2 M $NaNO_3$ **(Figure 2.18 a)**. The higher activity of ICO than pure $IrO_2$ or $Co_3O_4$, was due to the formation of more Co sites in $Co_3O_4$ as a result of doping of Ir. The ICO had >97 % current efficiency in 50 mM NaCl electrolyte, where the $Co_3O_4$ exhibited ~65 % and $IrO_2$ exhibited ~30 %. The Accelerated stability test (AST) for the ICO electrode conducted in 0.5 M $H_2SO_4$ solution resulted in a service life of 200 hours, where the $IrO_2$ electrode potential was quite higher. **(Figure 2.18 b)**[59]. This work shows that doping of precious metals at very small amount into the non-precious metals could improve the electrochemical performance by exposing additional active sites, similar to the activation of Ti sites observed from the doping of Ru in $TiO_2$[59].

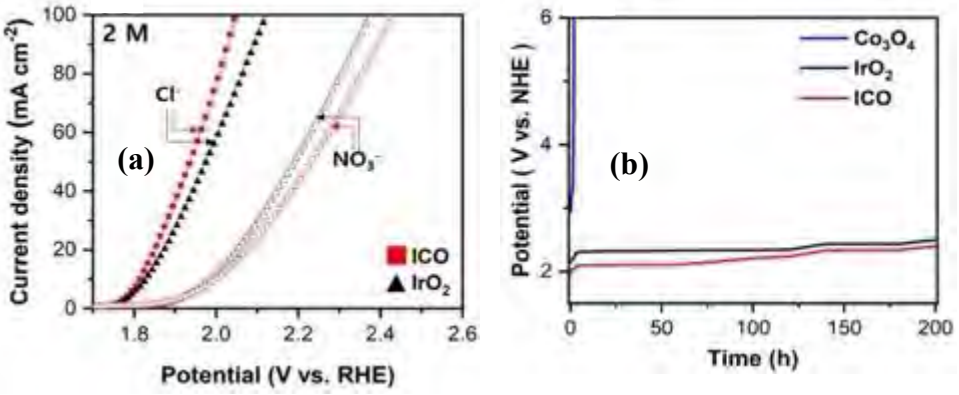


Figure 2.18: Accelerated stability test of ICO ($IrO_2$-$Co_3O_4$), $IrO_2$ and $Co_3O_4$ at 0.1 A $cm^{-2}$ in 0.5 M $H_2SO_4$ (pH=3). Reproduced with permission[59]. Copyright 2022, Elsevier.

### 2.4.2 Non-precious anodes for CER

In the recent days, the on-site water treatment plants using chlorine-electrolyzed water for water purification is growing rapidly. Nevertheless, the current $RuO_2$ based DSAs are costly and in order achieve widespread installation of these plants, development of cheap and highly stable CER electrocatalysts are necessary. Only a very few non-precious metal elements are highly active for chlorine evolution, such as Co, V, Mn, Ni, Fe, and Pb, etc. Based on the previous studies on the precious metal DSA's, multi-metal composites always deliver better performance compared to the single metal elements[48, 49, 86, 88]. The non-precious and non-stoichiometric cobalt, nickel and manganese based antimonates prepared using the co-sputtering technique on a FTO substrate was reported for acidic chlorine evolution reaction by Moreno and co-workers in 2019[49]. The synthesized materials were predicted to be stable in $Cl_2$ medium according to the pourbaix diagrams. The polarization curves before and after the stability test are shown in **(Figures 2.19 a , b).** Comparing to all the electrodes, the $CoSb_2O_x$ retained its activity and stability after the chronopotentiometry tests.

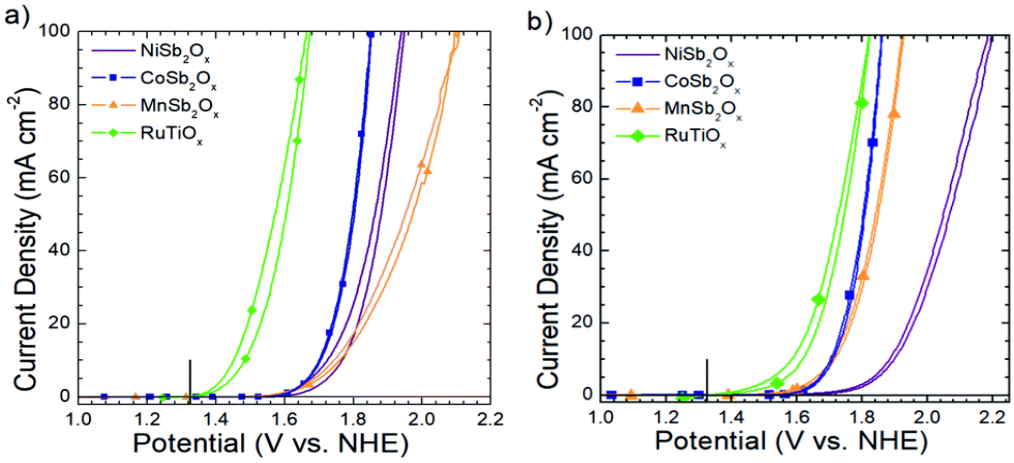


Figure 2.19: Comparison of polarization curves of $RuTiO_x$, $CoSb_2O_x$, $NiSb_2O_x$ and $MnSb_2O_x$ before and after the stability test at 100 mA $cm^{-2}$ in 4 M NaCl solution at pH=2. Reproduced with permission[49]. Copyright 2019, Royal Society of Chemistry.

The $CoSb_2O_{6-x}$ film remained on the substrate with only minor surface enrichment of Sb content (13 %) with only 48 mV increase in potential after 50 hours of operation at 100 mA $cm^{-2}$ in 4 M NaCl (pH=2) solution. It was further confirmed that, after a 250 hours chronopotentiometry tests at 100 mA $cm^{-2}$, the potential decreased by 47 mV from the initial value (~1.851 V vs NHE), ensuring its high stability. The other anodes lost their performance because of their poor structural stability under harsh conditions. In which, after a stability test of 50 hours, ~80 % and ~39 % surface enrichment of Sb content was found on the surface of $NiSb_2O_x$ and $MnSb_2O_x$ with potential increase of 297 mV and 134 mV[49]. The author mentioned that the activity can be further increased by increasing the loading of the catalyst material. However, increasing the loading can increase the charge transfer resistance of the electrodes[36]. Also, the elements are present in a non-stochiometric form, which makes it difficult to synthesize the catalyst using other synthesis methods. Later, Evan and co-workers prepared stochiometric $CoSb_2O_6$ and $MnSb_2O_6$ through electrodeposition technique on FTO substrate (**Figure 2.20 (a and b)**). Even though the $CoSb_2O_x$ had very high selectivity for chlorine evolution in 4 M NaCl (pH=2), the potential required for reaching 100 mA $cm^{-2}$ was very high for $CoSb_2O_6$ (around 2.2 V vs. RHE), as shown in **Figure 2.20 (c)**[89].

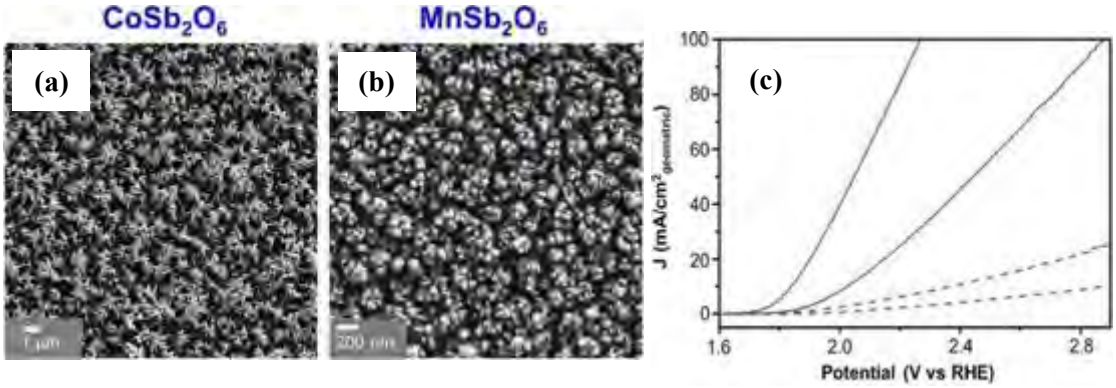


Figure 2.20: Comparison of surface morphology of the synthesized electrodes (a & b) and (c) the polarization curves of $CoSb_2O_6$ (purple) and $MnSb_2O_6$ (green) in 4 M NaCl (pH=2) and 0.5 M $H_2SO_4$. Reproduced with permission[89]. Copyright 2020, American Chemical Society.

It is suggested that the high activity for chlorine evolution in the $CoSb_2O_x$ prepared by Moreno and co-workers in the previous work was because of the presence of non-stochiometric elemental composition that have triggered the formation of the oxygen vacancies having appropriate binding energy for chloride ions[89]. As no theoretical calculations have performed, the reason for high selectivity for chlorine evolution is still not clear.

Recently, selective, and non-precious vanadium-based $Ti/Ti_{0.35}V_{0.35}Sn_{0.25}Sb_{0.05}O_2$ DSA was prepared through the thermal decomposition method for acidic chlorine evolution reaction by Alavijeh and co-workers. The electrode had an onset potential of 1.25 V vs. Ag/AgCl for chlorine evolution with a selectivity of 88 % at 40 mA $cm^{-2}$ and the overpotential for oxygen evolution >6 times higher than the potential of CER. Density of states and band structure calculations projected that the band gap of $Ti_{0.35}V_{0.35}Sn_{0.25}Sb_{0.05}O_2$ decreased from 2.01 eV to 1.0 eV, resulting in an improved activity compared to the pure V-oxide and V-doped $TiO_2$[88]. The presence of Ti increased the selectivity for chlorine evolution and doping Sn/Sb increased the overpotential for oxygen evolution. The activity obtained from this composite is very less but this work shows that vanadium is active for CER when doped with $TiO_2$, which is in agreement from the theoretical studies by Karlsson and co-workers[68].

Many researchers are recently focusing on the development of non-precious electrodes for chlorine evolution, but the high catalytic performance delivered by the precious metals is difficult to be achieved by the low-cost transition metal-based anodes. The non-precious anodes are cheap and widely available, but they can only decrease the initial capital investment cost. The high energy consumption of the non-precious catalysts because of their sluggish kinetics hinders their suitability for the practical applications[10]. Therefore, the non-precious metal anodes can be added

as dopants to decrease the precious metal concentration and to tune the electronic properties for achieving exceptional catalytic properties[59, 87].

### 2.4.3 Effect of physical properties on catalysts for CLER

All the above works focused on altering the electronic properties and crystal structure to increase the catalytic performance of the electrodes in CER. But the modulation of the physical properties, such as morphology, surface roughness, exposed surface area, and porosity also plays an important role in increasing the activity and stability of electrocatalysts. The factors such as bubble removal and mass transfer of reactive ions have a direct influence on the electrode potential. The electrodes that are made of the traditional thermal decomposition method have a mud crack surface morphology, which allows the electrolyte to penetrate inside these cracks. This causes bubble trapping, thereby inducing the catalyst removal from the electrode surface as a result of an increase in the tensile stress inside the cracks. Hence, several strategies have been proposed to improve the performance of the electrodes through structure modification.

One of the industrially convenient methods for preparing electrodes with molecular level homogeneity and nano structural morphology is the sol-gel method[90]. Chen and co-workers evaluated the impact of microstructural coating on the electrochemical performance of CER for $Ru_{0.3}Sn_{0.7}O_2$ (*rso*) electrode coating prepared through sol-gel thermal decomposition method with a Ru loading of 5.78 g $m^{-2}$. By controlling the coating times and loading amount, four different coating with mud-cracks (*mc-rso*), reduced-cracks (*rc-rso*), less-cracks (*lc-rso*), and crack-free (*cf-rso*) coatings have been prepared (**Figure 2.21**)[91].

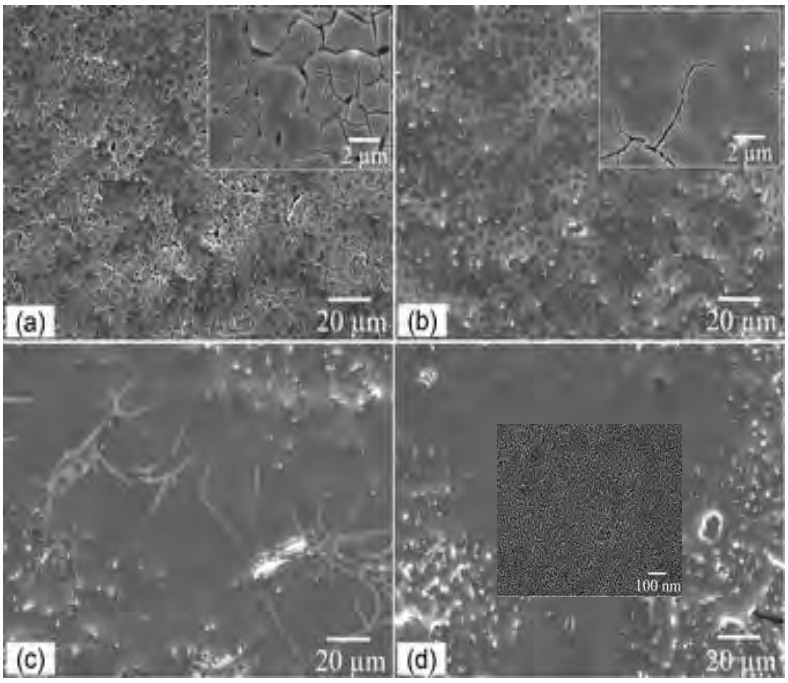


Figure 2.21: SEM images of mud-crack-RSO (a), reduced-crack-RSO (b), less-crack-RSO (c), crack-free-RSO (d), enlarged image of (d) indicating the nanoporous surface. Reproduced with permission[91]. Copyright 2019, Royal Society of Chemistry.

The electrode with mud crack (*mc-rso*) structure delivered 30 % higher voltametric charge ($q_a$) than the *cf-rso* (nano-porous), *lc-rso*, and commercial $Ru_{0.3}Ti_{0.7}O_2$ because of the penetration of the electrolyte through them. The voltametric charge ($q_a$) response shown in **Figure 2.22(a)**, indicates that only the outer surface layer of the compact *cf-rso* and *lc-rso* coatings have been exposed to the electrolyte. The polarization curves of the *cf-rso* and commercial electrode were measured in 3.5 M NaCl (pH=3) at 80 °C. The crack-free (*cf-rso*) electrode exhibited very less overpotential (~1.225 V vs NHE) in the low current density region (<100 mA $cm^{-2}$) compared to other electrodes in **Figure 2.22(b)**, because of the nano-porous network enabling efficient diffusion and transportation of the reactive ionic species. The compact coatings can ensure long service life as compared to mud-crack electrodes because, the penetration of the electrolyte

through the mud-cracks can form an insulating $TiO_2$ layer, deactivating the electrode. In addition, the better performance of sol-gel prepared crack-free (cf) electrodes was also due to the efficient bubble removal[91].

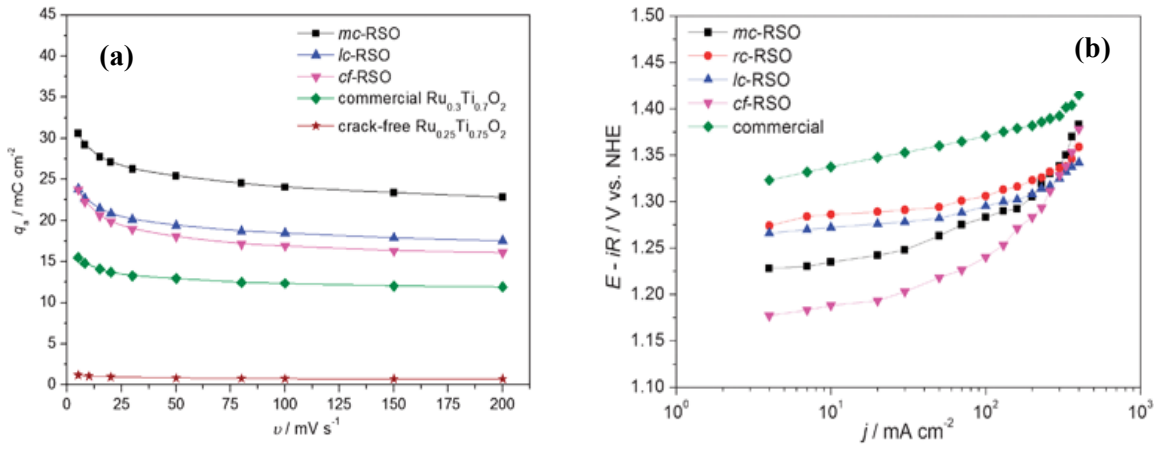


Figure 2.22: (a) Voltametric charge (qa) response obtained from different scan rates, (b) Comparison of polarization curves measured in 3.5 M NaCl (pH=3) solution. Reproduced with permission[91]. Copyright 2019, Royal Society of Chemistry.

In order to further improve the electrocatalytic activity, improving the porous nature of the electrode and making the electrolyte more accessible with efficient bubble removal under high current density is very important. Menzel and coworkers prepared an ordered 10 nm mesoporous micelle templated Ru or Ir, or Ru/Ir coated $TiO_2$ catalyst with excellent pore connectivity, by using Pluronic F127 as a templated polymer to induce the porous structure **(Figure 2.23)**. **Figure 2.23 (b and c)** shows that the activity obtained from the CV for the templated catalyst (120 mA $cm^{-2}$ at ~1.87 V vs. RHE) was two times higher than the untemplated catalysts (~50 mA $cm^{-2}$ at 1.9 V vs. RHE) in 4 M NaCl (pH=3) electrolyte[92].

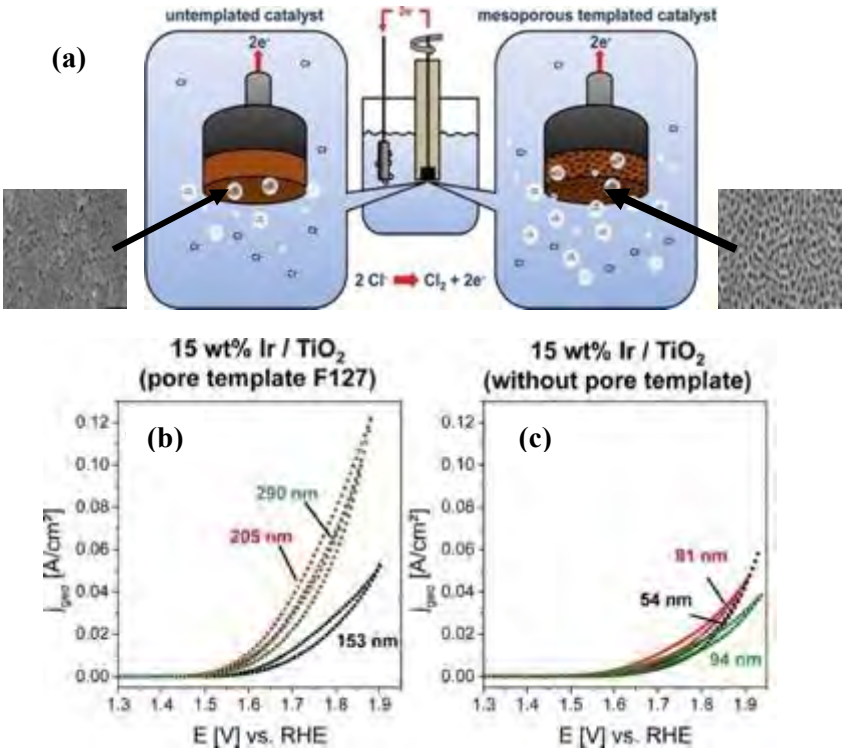


Figure 2.23: (a) Schematic diagram of the surface morphology of the templated and the untemplated Ir/$TiO_2$ electrode; (b and c) Comparison of cyclic voltammograms from the templated and untemplated Ir/$TiO_2$ catalyst with varying thickness in 4 M NaCl ( pH=3 ) solution. Reproduced with permission[92]. Copyright 2020, American Chemical Society.

Although the sol-gel methods can improve the mass transport of the reactants by enhancing the activity of a catalyst through surface structural modifications, there are high chances for the added surfactants and adhesives in electrode preparation to block the active sites from participating in the electrochemical reaction. Additionally, the interfacial resistance between the electrode coating and the substrate causes an increase in the overpotential[10]. The in-situ growth of the catalysts on the substrate can reduce the interfacial resistance, thereby providing an efficient electron transfer and protecting the catalyst from peeling off, which is not possible via the thermal decomposition method [10, 72, 93-95].

The electrodes with high contact angle and less adhesion forces are needed for achieving high catalytic activity. The traditional DSA coating with less contact angle and high adhesion forces is also one of the reasons for its poor performance. Jiang and co-workers constructed a superaerophobic electrodeposited $RuO_2$ coating on the hydrothermally grown $TiO_2$ nanostructured arrays (NSA) and correlated the measured electrochemical results with the bubble adhesion force and the contact angle. The nanostructured $RuO_2$@$TiO_2$ sheets had an average size of 200 nm with 20 nm thickness, as shown in **Figure 2.24 (a and b)** [95].

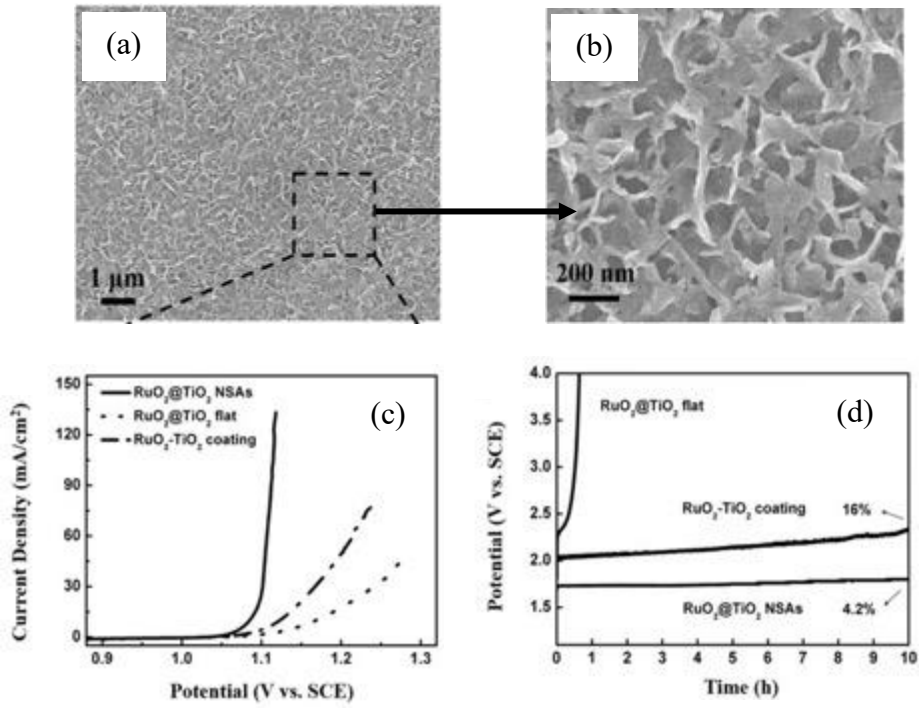


Figure 2.24: (a) SEM images of $RuO_2$@$TiO_2$ nanosheet arrays; (b) enhanced image; (c) LSV polarization curves and (d) Chronopotentiometry test at 250 mA $cm^{-2}$ of $RuO_2$@$TiO_2$ NSA, $RuO_2$@$TiO_2$ sheet, and $RuO_2$-$TiO_2$ traditional coating. Reproduced with permission[95]. Copyright 2016, Wiley-VCH.

**Figure 2.24 (c and d)** compares the polarization curves and the chronopotentiometry tests of the $RuO_2$@$TiO_2$ NSA and the control samples. The $RuO_2$@$TiO_2$ NSA had an onset potential of

1.07 V vs. SCE reaching a current density of 6.65 mA $cm^{-2}$, while the flat electrode and the DSA delivered 0.37 mA $cm^{-2}$ and 0.65 mA $cm^{-2}$ in saturated NaCl solution. Under chronopotentiometry test at a current density of 250 mA $cm^{-2}$ for 10 hours, the NSA electrode only had a 4.2 % increase in potential, while there was a 16 % increase in the potential for the traditional coating and the flat film electrode had a steep increase in overpotential. The NSA electrode experienced less bubble adhesion force of ~3 uN due to less area of contact between the catalyst surface and the bubble, comparing to higher contact area exhibited by the flat film and traditional coating resulting in higher adhesion forces (42 mN and 29 mN). The NSA electrode has high aerophobicity with large bubble and less electrolyte contact angle of (157.2° and 15.5°), better than the flat film (116.2° and 78.1°) and traditional coating (128.2° and 56.3°). The flat film electrodes make it difficult for the bubbles to detach, which is not observed in NSA. Also, the surface roughness (*r*) calculated for the NSA was greater than the control samples, resulting in increased surface wettability and aerophobicity. Post SEM measurements proved that the NSA retained its structure after the stability test, owing to its efficient bubble removal, while damages were found in the traditional coating. It is because of the increased tensile stress caused by the bubbles, that peeled off the flat film due to poor bubble removal[95].

Similar way, Wang and co-workers prepared the $IrO_2/TiO_2$ nanosheet arrays through in situ growth of $TiO_2$ nanosheets and sputtered $IrO_2$ on top of it. The electrode reached 10 mA $cm^{-2}$ current density with 44 mV overpotential in saturated NaCl solution (pH=2). The electrode delivered 50 mA $cm^{-2}$ at 1.61 V vs. RHE in the chronoamperometry test with an 92.3 % initial current density retention after a 50-hour stability test[3, 95]. In both of the above works based on the nanostructured electrodes, the reason for the increased activity and the stability is due to the high surface concentration of the $Cl^-$ ions, not affecting the local current density and not blocking the

active sites by providing efficient $Cl_2$ bubble removal, thus maintaining the electrode potential constant[3, 95]. But compared to the thermal decomposition and electrodeposition methods, sputtering requires special equipment making the process complicated and costly[96, 97]. Adopting hydrothermal methods for insitu growth of catalyst seems attractive, but the electrodes size prepared are very small (~ 4–6 $cm^{-2}$). Several complications might arise when converting them to industrial scale, where big electrodes are needed (>1 $m^2$)[3, 95].

Comparing to the hydrothermal method for in-situ growth of nanostructured electrodes, the growth of $TiO_2$ nanotubes using the electro-anodization process is very attractive and suitable for large scale. Also, the one-dimensional nanomaterials possess high electrical conductivity, enhanced surface area and strong adhesion to the substrates. By tuning the electrolyte composition and the electrochemical parameters (voltage and current), the physical properties of these nanotubes can be altered[70, 98]. Heo and co-workers synthesized $RuO_2$-loaded conductive black $TiO_2$ nanotube arrays by constructing the $TiO_2$ nanotube arrays through two step electro-anodization process followed by calcination in Ar atmosphere at 450 °C. $RuO_2$ was deposited on the nanotubes though pulsed electrodeposition process at -1 mA $cm^{-2}$ for 50 ms with a resting time of 1 s. The advantage of pulsed electrodeposition is the coverage of the inner pores of the nanotubes with $RuO_2$, while the galvanostatic process can only deposit on the outer surface resulting in a very less loading of Ru species. The SEM images of black $TiO_2$ nanotube arrays, along with the current density and potential profiles recorded during the $RuO_2$ deposition is shown in **Figure 2.25 (a and b)** [99].

The polarization curves were measured in 5 M NaCl (pH=2) solution, and the $RuO_2$ coated black $TiO_2$ ($RuO_2$/b-$TiO_2$) only required 1.090 V and 1.125 V vs. SCE to reach a current density of 10 mA $cm^{-2}$, and 100 mA $cm^{-2}$, while the electrode without $RuO_2$ coating showed negligible

activity (**Figure 2.25 c**). In acidic conditions, the faradaic efficiency measured was 95.25 % and the high performance of the black $TiO_2$ is because of its high electrical conductivity compared to the crystalline $TiO_2$, as reflected in the chronopotentiometry test at a current density of 100 mA $cm^{-2}$ for 4 hours. The black $TiO_2$ maintained a stable potential, while a steep increase in potential has been observed for the crystalline $TiO_2$ as a result of poor electrical conductivity at increasing potentials (**Figure 2.25 d**) [99].

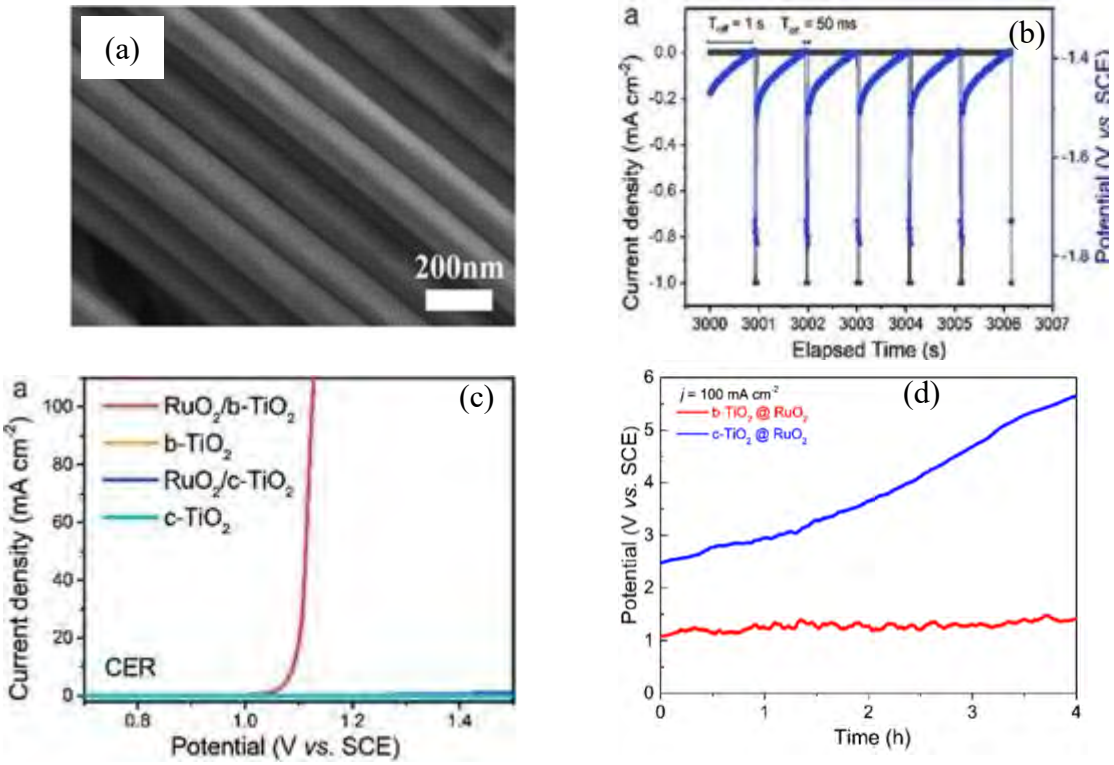


Figure 2.25: (a) SEM image of conductive black $TiO_2$; (b) Electrodeposition profile of $RuO_2$ (Current density vs. Time vs. Potential); (c) LSV profiles of c-$TiO_2$ and b-$TiO_2$ with and without $RuO_2$; (d) Chronopotentiometry test observed at 100 mA $cm^{-2}$ for 4 hours in 5 M NaCl (pH=2). Reproduced with permission[99]. Copyright 2020, Elsevier.

The high catalytic performance is because of the presence of defects in the black-$TiO_2$, resulting in increased electrochemically active surface area, but the activity depends on $RuO_2$

loading because it improves the electrical conductivity by acting as an electron donor[70, 99]. Enhanced electrical conductivity at increased potentials is deemed to be necessary for electrocatalytic reactions, as the industrial reactions are performed at high anodic potentials[10, 11, 99].

Carbon cloths and carbon papers are widely used as substrates in electrocatalytic reactions like OER and HER because of its high electrical conductivity and 3-dimensional structure[100-103]. After the graphite electrodes, carbon-based electrodes have been very rarely used in chlorine evolution reaction[24, 93, 104, 105]. Zhang and co-workers prepared $RuO_2$ decorated carbon fiber cloth through galvanostatic electrodeposition (20 mA $cm^{-2}$), followed by thermal annealing at 500 °C in an air atmosphere (**Figure 2.26 a**). At 1.20 V vs. SCE, the $RuO_2$/CC-10 delivered a higher current density of 175 mA $cm^{-2}$, comparing to the $RuO_2$/CC-5 (105 mA $cm^{-2}$), $RuO_2$/CC-20 (85 mA $cm^{-2}$) and $RuO_2$/CC-30 (65 mA $cm^{-2}$) in 5 M NaCl solution (**Figure 2.26 b**). A very small charge transfer resistance of 3.7 Ω was measured for 10 min electrodeposition, compared to 8.76 Ω, 10.17 Ω and 14.91 Ω for 5 mins, 20 mins and 30 mins deposition of $RuO_2$ (**Figure 2.26 c**). The bubble shielding effect at high current densities has been resolved by the 3-dimensional topography of the carbon cloth, that resulted in efficient utilization of the $RuO_2$ and decreased charge transfer resistance[93].

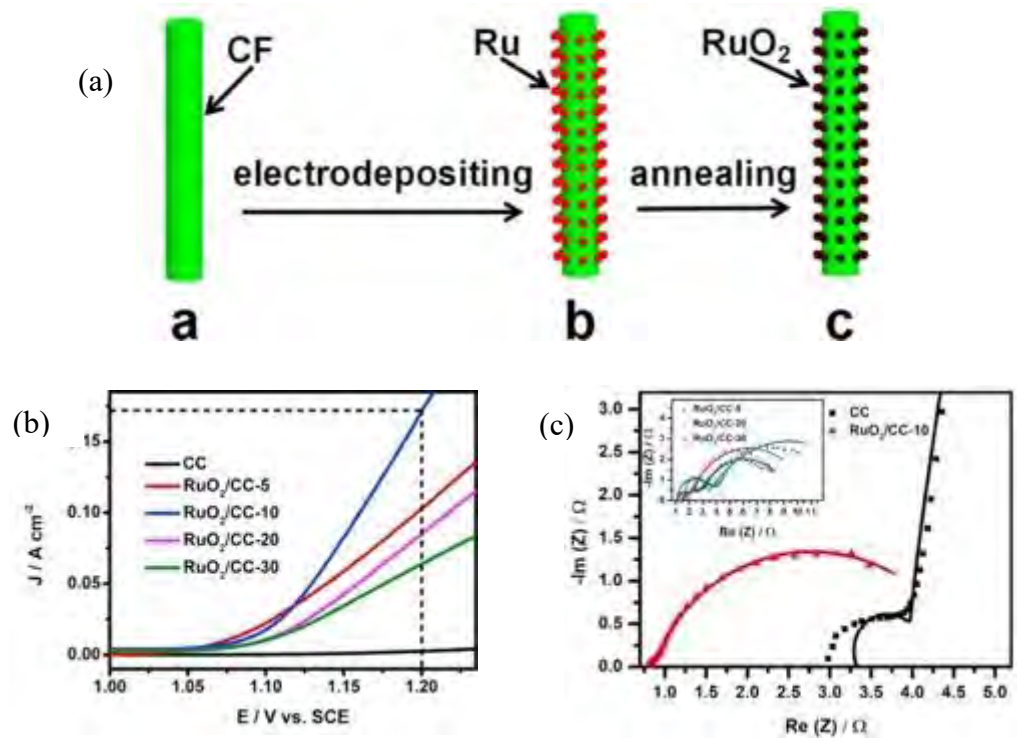


Figure 2.26: (a) Schematics of preparation of $RuO_2$ on carbon-cloth; (b) LSV and (c) EIS data of $RuO_2$-CC (5 , 10, 20, and 30 mins) deposition time. Reproduced with permission [93]. Copyright 2019, Elsevier.

The physical and chemical properties of the carbon materials can be altered through heteroatom doping. Microwave irradiation was used to decorate Pt nanoparticles (~10.9 nm) on heteroatom (nitrogen and phosphorous) doped carbon (~200 nm) (Pt/NPC) by Huang and co-workers. At 50 mA $cm^{-2}$ in an acidic 5 M NaCl solution, an overpotential (η) of 108 mV was measured for the Pt/NPC, that is close to the 62 mV (η) exhibited of Pt/C. The high catalytic activity is because of, (i) the synergy between the Pt nanoparticles and the N/P doped C and (ii) the formation of active sites as a result of electronegativity difference between the carbon and heteroatom dopants[104, 106]. Even though the electrode has a high electrochemically active surface area with less charge transfer resistance, the decomposition of carbon substrates will diminish the electrode performance at higher potential and pH conditions[107, 108]. Thus, this work can be

considered a good example, and can be used to prepare the electrodes based on metal foams with high electrical conductivity and 3-dimensional structures[109, 110].

### 2.4.4 Strategies for maximizing the utilization of catalytic materials

Unlike the homogeneous catalysts, the behavior and performance of the heterogeneous catalysts totally depends on their surface property. Since the catalytic reaction only happens on the surface, the efficient usage of catalytic materials is very important and is a growing concern ,especially in the usage of precious metal as their cost increases by ~5 % every year. Apart from the cost of the raw material, converting them to usable catalysts adds up extra cost. The nature of the active site not only depends on the composition and shape, but also the size of the catalyst. Reducing the size of the particle to increase the amount of electrochemically active surface area for per gram of loading is one way to overcome this issue[111]. In the recent days, many researchers have been focusing on achieving high performance and maximum utilization efficiency with less loading of the electrocatalyst through single atom catalysts and supported catalysts[111-113].

#### 2.4.4.1 Single atom catalysts

Single atom catalysts are the ones in which the catalysts are atomically dispersed on the support structure (eg: carbon-based materials, metal oxides, etc.) and are isolated from one atom to another. Compared to the conventional catalysts, the single atom catalysts have shown promising evidence in high metal utilization efficiency, selectivity, and stability in many heterogeneous catalytic reactions like HER, OER ORR, etc.[45, 113-115]. Very few researchers have been working on single atom catalysts for chlorine evolution reaction. Lim and co-workers prepared the atomically dispersed Pt-$N_4$ (2.7 wt % - 0.7 wt %) on multi-walled carbon nanotubes (Pt1/CNT) for chlorine evolution reaction (**Figure 2.27 a**)[26]. The electrocatalytic activity was

measured in 1 M NaCl ( pH=0.9) using a RRDE, and $Pt_1$/CNT only required 50 mV (η) to reach 10 mA $cm^{-2}$, while the PtNP/CNT and commercial DSA needed 120 mV (η) and 105 mV (η). In situ electrochemical XANES showed that, only negligible changes were observed in the absorption spectrum in 0.1 M $HClO_4$ electrolyte, while significant changes were observed in the presence of NaCl. Increase in intensity of absorption were observed at 1.40 V and 1.50 V in the presence of NaCl confirming its high selectivity towards oxidation of chloride ions (**Figure 2.27 b**).

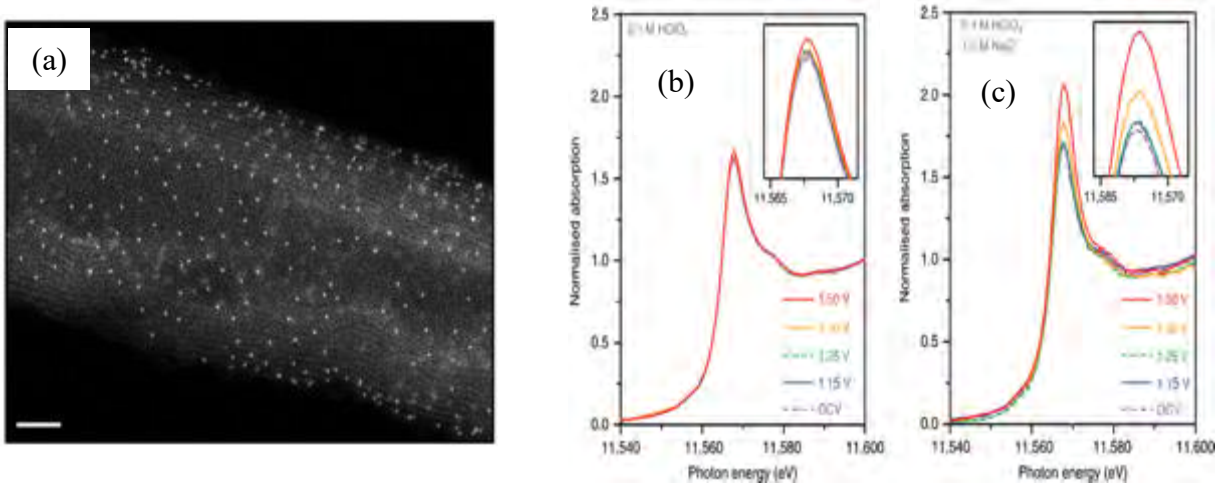


Figure 2.27: (i) HAADF-STEM image of $Pt_1$-CNT; (ii) In situ electrochemical XANES results of $Pt_1$/CNT in the absence (a) and presence (b) of NaCl. Reproduced with permission[26]. Copyright 2020, Springer Nature.

But, the electrode only retained 72 % of its initial activity at 1.41 V vs. RHE, after 12 hours of chronoamperometry test, incurring a huge loss because of the dissolution of the Pt metals[26]. The electrode might lose its complete activity at high current density or in industrial conditions (~400 mA $cm^{-2}$). Another complexity in the single atom catalysts is achieving high-density loading of single atoms in a specific area[112, 113]. Also, metal substrates should be used as supports instead of carbon in order to avoid the oxidation of the support at high potentials in anodic reactions involving water[24, 108].

### 2.4.4.2 Supported catalysts

The catalysts employed in chlorine evolution reactions suffer from anodic corrosion at either higher operating potentials or under alkaline conditions**.** The formation of durable active sites under high current density with superior selectivity and low catalyst loading is a grand challenge[1, 10, 11, 116]. Lim and co-workers synthesized the Nb-doped $TiO_2$ loaded with $RuO_2$ (~1.1 at %) nanoparticles through a two-step hydrothermal process. The HAADF and elemental mapping image of $RuO_2$/Nb:$TiO_2$-A200 is shown in **Figure 2.28**[25].

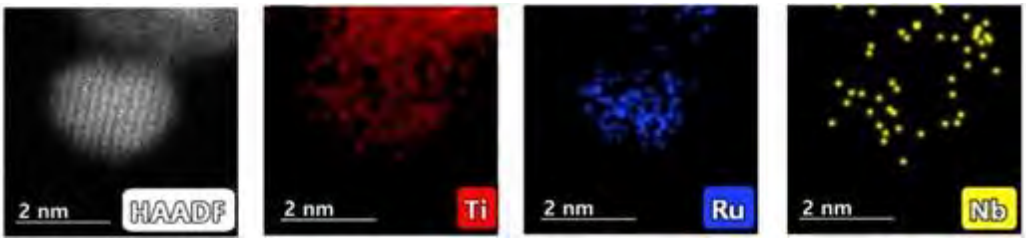


Figure 2.28: HAADF and elemental mapping image of $RuO_2$/Nb:$TiO_2$-A200 nanoparticles. Reproduced with permission[25]. Copyright 2021, American Chemical Society.

The unprotected $RuO_2$ decorated $TiO_2$ NP experienced a continuous decrease in activity during the LSV test over 50 cycles, because of the loss of $RuO_2$ nanoparticles through corrosion from the $TiO_2$ surface (0 cycles = 2.54; after 50 cycles = 0.45 %.). Interestingly, Nb doping into the $TiO_2$, formed a protective $TiO_2$ layer on top of $TiO_2$ nanoparticles during calcination, protecting the $RuO_2$ from anodic dissolution. The protected catalyst maintained a stable activity for 50 LSV cycles (**Figure 2.29 a**) with a high faradaic efficiency of 93.7 % (0.6 M NaCl, pH=6) and 97.7% (5 M NaCl, pH=2) at 50 mA $cm^{-2}$. The overpotential required for $RuO_2$/Nb:$TiO_2$-A200 to reach 10 mA $cm^{-2}$ was only 22 mV, lesser than the DSA (158 mV). The Nb doping formed an $TiO_2$ layer on $RuO_2$, making the catalyst more durable under harsh conditions, through inhibition of the surface hydroxylation and suppressing the side reactions as revealed from the XPS results shown

in **Figure 2.29 b**. As a result negligible changes in potential values was observed during the chronopotentiometry test at 10 mA $cm^{-2}$ in dilute 0.6 M NaCl (**Figure 2.29 c**) and 100 mA $cm^{-2}$ in acidic 5 M NaCl ( **Figure 2.29 d**) [25].

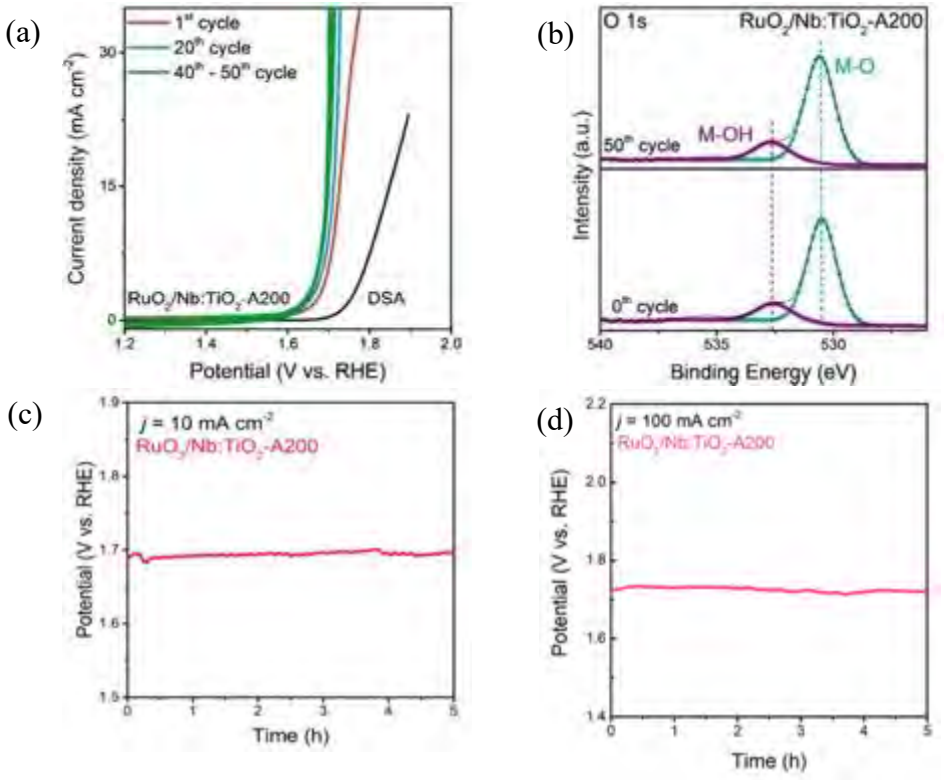


Figure 2.29: (a) LSV provides; (b) XPS spectra of $RuO_2$/Nb:$TiO_2$(A200) nanoparticles (before and after in dilute NaCl solution); (c) Chronopotentiometry tests for 5 hours at 10 mA $cm^{-2}$ in dilute 0.6 M NaCl (pH=6); (d) 100 mA $cm^{-2}$ in acidic 5 M NaCl (pH=2). Reproduced with permission[25]. Copyright 2021, American Chemical Society.

The utilization of supported catalysts in large-scale electrolysis sounds promising because of the usage of very smaller amount of precious (>5 %) metals as comparing to the DSA's (20 % to 40 %). But the loss of active sites in the DSA or composite catalysts are backed by the active sites beneath the surface ensuring long service life, while the loss of active sites in the supported catalysts are permanent.

## 2.5 High entropy oxides for in catalysis

As new group of ceramic materials comprising five or more elements in a single-lattice, leading to high configurational entropy value (> 1.5 R) known as high entropy ceramics (HEC's) have been actively explored for variety of applications in recent days. The physical and chemical properties of these materials can be tuned by altering the type and stoichiometry of the metal elements used. Random mixing of elements of different atomic sizes, lowers the overall energy required for the activation and transportation of the active reactant species, that is beneficial for both electrochemical and photoelectrochemical reactions. High entropy oxides have been applied for several catalytic reactions such as, HER, OER, ORR, CO oxidation, $CO_2$ reduction, and alcohol oxidation. As oxygen defects play an important role in enhancing the activity of a catalyst, especially oxidation reactions like CER, OER, etc., creating and controlling those defects in high entropy materials will be very useful for increasing their catalytic activity. High entropy materials can be applied directly as catalysts or as a support structure to anchor the catalytic materials. Apart from the structure and surface properties, particle size has a huge influence on the catalytic activity. As high entropy oxides tend to have huge number of active sites, reducing their particle size to nanometers (<100nm) could result in efficient electron transfer and high catalytic activity. A very few reports have been reported for the nano-sized high entropy oxides for electrocatalysis[117-119].

Duan and co-workers used the solvothermal method to synthesize nanosized $(FeCoNiCrMn)_3O_4$ high entropy spinel oxide electrocatalyst (**Figure 2.30 a**), with an average particle size of 6.24nm (**Figure 2.30 b**) for alkaline oxygen evolution reaction. The HEO required an overpotential of 288 mV to reach 10 mA $cm^{-2}$, less than the commercial $RuO_2$ which required 300 mV overpotential as observed from the LSV curves measured in 1 M KOH solution (**Figure 2.30 c**). Tafel plot and EIS results suggest that the electrode had a smaller value of 60 mV $dec^{-1}$

and 8.7 Ω ($R_{ct}$) comparing to the pure $RuO_2$ (150 mV $dec^{-1}$, $R_{ct}$ = 54.1 Ω). A potential increase of 1.3 % (0.019 V) was observed from the initial value of ~1.52 V vs RHE during the chronopotentiometry test at 10 mA $cm^{-2}$ (**Figure 2.30 d**). Post analysis revealed that the amount of oxygen vacancies increased from 28.1 % to 51.4 % as a result of partial oxidation of the metal oxides and loss of oxygen anions during the electrochemical activation process[119].

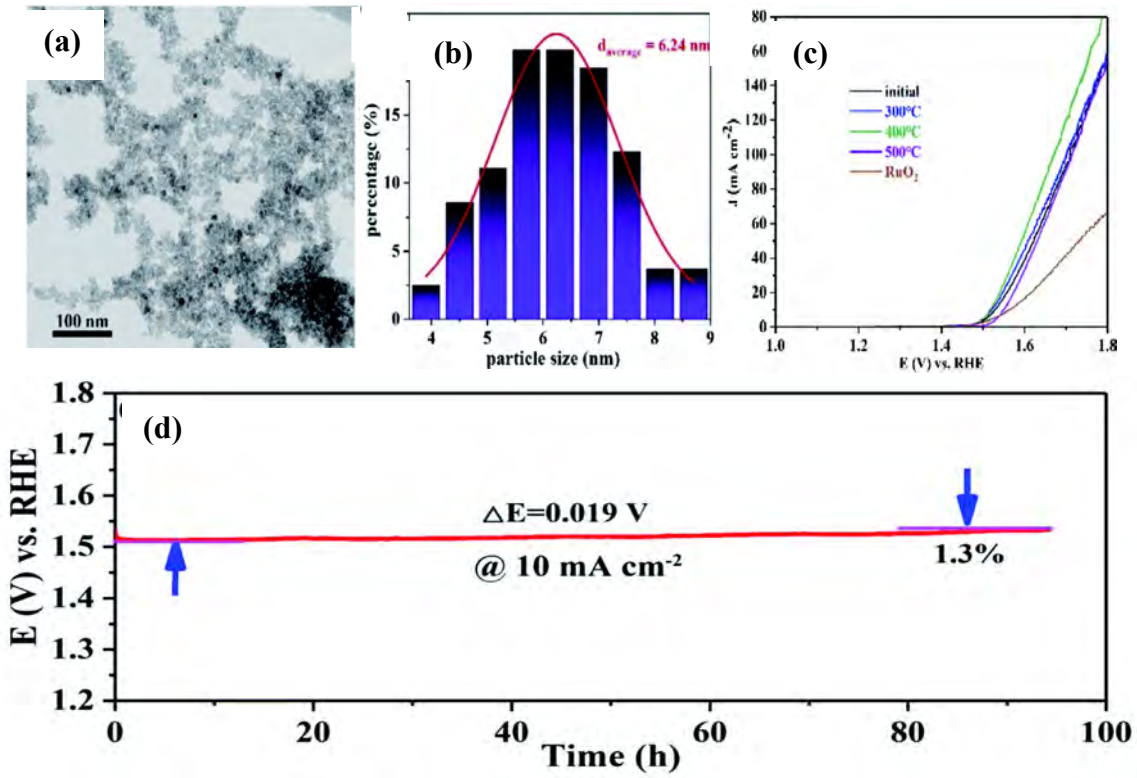


Figure 2.30: (a)Morphology; (b) particle size of $(FeCoNiCeMn)3O_4$ calcinated at 400 °C; (c) LSV polarization curves measured of the HEO's and $RuO_2$ measured in 1 M KOH solution and (d) chronopotentiometry test at 10 mA $cm^{-2}$. Reproduced with permission[119]. Copyright 2022, Royal Society of Chemistry.

However, most of the HEO's are poorly conductive. The addition of the conductive materials is necessary, in order to boost the electrocatalytic activity. The surfactant assisted solvothermal synthesis method was used to prepare $(CoCuFeMnNi)O_4$ spinel (Fd3m structured) nanoparticles decorated on multi-walled carbon nano tubes (MWCNT) for alkaline oxygen

evolution. The HEO/MWCNT needed lesser potential of 1.58V vs. RHE, while the bare HEO needed 1.63V vs RHE to reach 10 mA $cm^{-2}$ in alkaline 1 M KOH solution (**Figure 2.31 a**). The poor electrical conductivity of the HEO, causes an increase in the charge transfer resistance (~100 Ω at 1.58 V vs. RHE), that was solved by the MWCNT owing to the efficient electron transfer at higher potentials (~25 Ω at 1.58 V vs. RHE) (**Figure 2.31 b**) [120].

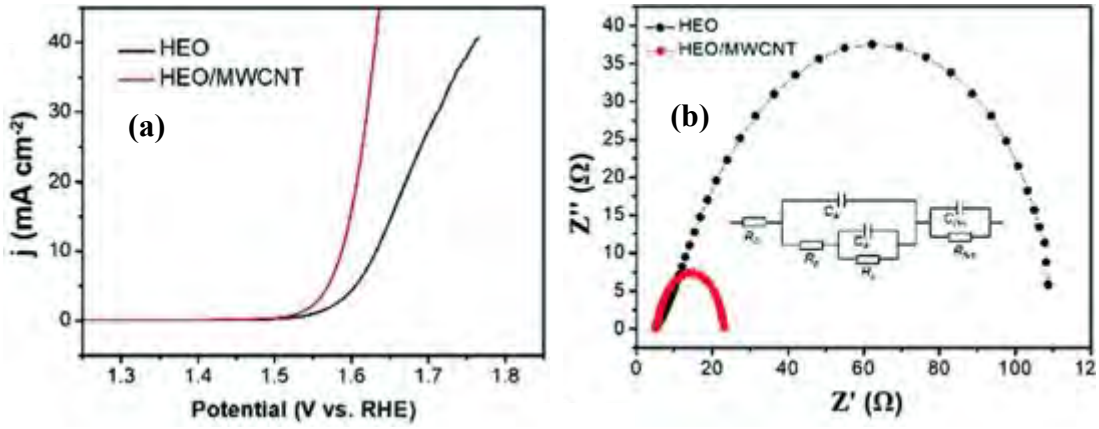


Figure 2.31: Comparison of activity from LSV curves and (b) EIS plots of HEO and HEO/MWCNT. Reproduced with permission[120]. Copyright 2019, Royal Society of Chemistry.

The presence of oxygen defects and straining effect created by the presence of five cations, good lifetime of charge carriers, and modified electronic structure are the reasons for the high performance of high entropy oxides. Increasing the surface area of the HEO can further increase the catalytic activity[121]. The high entropy materials are superior in activity and stability comparing to traditional electrocatalyst like $RuO_2$, $IrO_2$ and $Co_3O_4$, etc. and photocatalyst like $TiO_2$, $BiVO_4$, and ZnO, etc[120]. As the surface area has a huge influence on the activity of the electrocatalysts, synthesizing nanosized high entropy materials are necessary.

## 2.5. Summary

Considering the increase in requirement of chlorine for production of valuable products and onsite electrochemical water treatment, high performing anodes are needed that can operate at rigorous operating conditions with less energy consumption. Even though the state-of-art DSA are capable of operating at high potential for long time (>4 years), their energy consumption is very high because of their poor catalytic activity as a result of the low surface area and less electrical conductivity. They also suffer from poor stability in the dilute and high pH electrolysis conditions as a result of corrosion of the active sites. Therefore, highly active, selective, and stable electrocatalysts with less energy consumption are needed for both industrial and dilute/sea-water electrolysis systems.

Up to date, many efforts have been devoted to developing various strategies to modify or entirely fabricate new anodes for chlorine oxidation reactions, such as: (i) Template assisted synthesis of nano porous coatings on DSA; (ii) Sol-gel synthesis of nano-structured electrodes[92]; (iii) In-situ growth of electrodes using hydrothermal method[72, 95]; (iv) nanofilms through co-sputtering method[3, 49]; (v) electrodeposition[70, 71, 95]; (vi) single atom catalysts, and (vii) supported catalysts[25]. However, their suitability in industrial level design is limited because of either complicated synthesis process or poor performance on long run. Recently, many researchers are focusing on designing the low-cost non-precious anode for chlorine evolution rection[49, 88], but the non-precious anodes are not able to deliver the same performance as the precious metal anodes like $RuO_2$ and $IrO_2$. Therefore, the search for new anode materials is needed that are highly active and stable in all electrolyte conditions and superior to the DSA's [10, 11].

Very recently, single phase high entropy ceramics are being recently explored as potential candidates for many catalytic reactions such as thermocatalysis, electrocatalysis (OER, HER, ORR,

and $CO_2$ reduction, etc.), catalysts for metal-ion[122], metal-sulphur[123] and metal air batteries[124], and photocatalysis[121], because of their high stability against corrosion and the presence of abundant active sites, resulting in high catalytic activity. High entropy materials are expected to provide high catalytic activity at low overpotential and high stability against corrosion, because of their random mixing and the combined effect of five elements[18-21]. Thus far, a very few materials have been explored because of its experimental synthesis complexity. Inspired from the properties of HEO, single phase rutile high entropy oxides with random mixing are expected to deliver high catalytic performance comparing to the traditional DSA.

The literature survey and the key challenges mentioned above leads to the objectives as stated in Chapter 1, section 1.2.

# Chapter 3. Experimental Section

## 3.1. Reagents and laboratory equipment

The chemical reagents and laboratory equipment used in the anode material synthesis, electrode slurry preparation, coating, and testing of catalytic activities are listed in Tables 3.1 and 3.2.

Table 3.1 Chemical reagents used in the experiment

| Item | Formula | Grade | Brand |
|---|---|---|---|
| Ruthenium(III) chloride hydrate | $RuCl_3 \cdot xH_2O$ | ReagentPlus® 40.0 % – 49 % | Sigma-Aldrich |
| Tin chloride | $SnCl_2$ | 99.0 % | Aladdin |
| Titanium(IV) butoxide | $Ti(OCH_2CH_2CH_2CH_3)_4$ | 97.0 % | Sigma-Aldrich |
| Ammonium metavanadate | $NH_4VO_3$ | ACS reagent, ≥99.0 % | Sigma-Aldrich |
| Cobalt(II) chloride hexahydrate | $CoCl_3 \cdot 6H_2O$ | 98.0 % - 102.0 %, ACS reagent | Acros organics |
| Ethylene glycol | $C_2H_6O_{12}$ | >99.5 % | Acros organics |
| Ammonia water | $NH_4OH$ | 25 % | Macklin |
| Ethanol | $CH_3CH_2OH$ | AR | Duksan |
| Sodium Chloride | NaCl | 99 %, Ar | Macklin |
| Hydrochloric acid | HCl | 37 % | Sigma-Aldrich |
| Sodium hydroxide | NaOH | ≥99 % EMSURE | Sigma-Aldrich |
| Carbon paper | TGP-H-060 | Tech | Toray |
| Isopropyl alcohol | $(CH_3)_2CHOH$ | AR | |
| Nafion® 117 solution (~5% in a mixture of lower aliphatic alcohols and water) | - | 5 % in water and alcohol | Sigma-Aldrich |
| Ketjen black carbon | ECP-600JD | - | MTI |

Table 3.2 Instruments used in the experiment

| Item | Type | Brand, Supplier |
|---|---|---|
| Analytical balance | SECURA324-1OIN | Sartorius |
| Magnetic stirrer with hotplate | SP88857104 | Thermo scientific |
| Ultrasonic cleaner | MB-200MOD | Branson |
| Vacuum drying oven | DZF-6000 | Standhill |
| Centrifuge | TG16G | BeiHong |
| Muffle furnace | KLS 15/12 | Thermoconcept |
| Potentiostat | PGSTAT302N | Metrohm Autolab |

## 3.2. Material synthesis

In a typical synthesis process, 0.465 mmol $RuCl_3 \cdot xH_2O$ (0.096 g), 0.465 mmol $SnCl_3$ (0.088 g), 0.465 mmol $Ti(OCH_2CH_2CH_2CH_3)_4$ (0.158 g), 0.465 mmol $NH_4VO_3$ (0.054 g), and 0.465 mmol (0.110 g) were dissolved in 50 mL of ethylene glycol and is maintained under stirring for 6 hours. Some 5 mL, ammonia water was added to increase the solubility of the precursors. The solution was then transferred into a 100 mL Teflon-lined stainless-steel autoclave and heated in an oven at 180 °C for 12 hours. Once the autoclave has been cooled to room temperature, the precipitated solid residue is washed with DI water and ethanol via centrifugal separation (10,000 rpm for 10 mins) to remove the organic solvent. The process was repeated three times. The collected samples were then dried in an oven at 80 °C for 12 hours, and the nanosized high entropy rutile oxides were obtained by sintering the precursor sample at 500 °C (HEO-R-500). In addition to that, samples were sintered at 350 °C (HEO-R-350), 400 °C (HEO-R-400), 600 °C (HEO-R-600) and 700 °C (HEO-R-700) for comparison.

## 3.3. Materials characterizations

The structural information of the synthesized powder material was analyzed through an X-Ray diffractometer (XRD, Rigaku Smartlab) with Cu Kα radiation (λ = 0.154 nm) between 10° –

80° at a scanning rate of 1° $min^{-1}$. The morphology, HRTEM image, selected area diffraction pattern (SAED) image, and elemental analysis/mapping was observed under a scanning transmission electron microscope (STEM, JEM-2100F). The X-ray photoelectron spectroscopy (XPS, Thermo Scientific Nexsa) was performed using a monochromatic aluminium X-ray source to identify the elements and their respective oxidation states.

## 3.4. Electrochemical measurements

All the electrochemical characterizations were performed with PGSTAT302N metrohm Autolab potentiostat. The catalyst slurry was prepared by dispersing 2.5 mg of HEO-R catalyst powder with 0.235 µL isopropanol and 15 µL of Nafion 117 solution. Ketjen black carbon powder (0.5 mg) was added to enhance the electrical conductivity and the support between the catalyst particles. Then, 50 µL of the prepared catalyst ink was drop cast on a carbon paper to achieve a loading of ~1 mg $cm^{-2}$. To avoid concentration overpotential and diffusion-related problems, the exposed electrode area is maintained at 0.05 $cm^2$. An electrode with an exposed area of 0.2 $cm^2$ was also tested to confirm that there was no change in the stability of the catalyst during the chronopotentiometry test, depending on the exposed area. The electrochemical performance of HEO-R is compared with the control electrode, $RuO_2$-$TiO_2$ DSA, purchased from the Baoji Changli Special Metal Co., Ltd. All the process variables such as electrode size, electrolyte concentration, pH, electrolyte stirring speed (rpm), and temperature were maintained the same for all the electrodes tested in this work. A 100 mL H-type cell with Nafion 117 membrane separating the anode and cathode compartments was used. Teflon electrode holders were used to mount the working electrodes. Pt foil was used as a counter electrode and Ag/AgCl filled with 3.5 M NaCl was used as a reference electrode. All the electrode potentials reported in this work were converted

into the reversible hydrogen electrode (RHE) scale with 100 % manual iR correction unless otherwise mentioned using the following equation:

$$E_{RHE}=E_{Ag/AgCl}+ 0.1976 + \left(\frac{RT \ln 10}{F}\right) \text{ pH vs. RHE} \quad \textbf{3.1}$$

Where, $E_{Ag/AgCl}$ = electrode potential measured (V), R = gas constant (8.814 J $K^{-1}$ $mol^{-1}$), T = Temperature (K), and F = Faraday's constant (96485.3 C $mol^{-1}$).

The equilibrium potential of CER is calculated using the following equation[25, 26]:

$$E_{CER}(T, \alpha(Cl^-), \alpha(Cl_2)) = E^{\circ}_{CER} - \frac{RT}{F} \ln \alpha(Cl^-) + \frac{RT}{2F} \ln \alpha(Cl_2) \quad \textbf{3.2}$$

Where $\alpha(Cl^-)$ = molar concentration of NaCl in the electrolyte, and $\alpha(Cl_2)$ = 0.01 (partial pressure of evolving chlorine gas under Ar.

$$E^{\circ}_{CER} = \left[1.358V + \left(\frac{RT \ln 10}{F}\right) pH\right] - \left(\frac{dE^{\circ}}{dT}\right) \times (T\text{-}298.15\ K) \text{ vs. RHE} \quad \textbf{3.3}$$

Where, $\frac{dE^{\circ}}{dT}$ = 0.001248 according to reported works[26].

The catalytic performance of the HEO-R was measured using HEO-R as a working electrode and Pt-foil as a counter electrode in acidic 5 M NaCl (pH=2) and dilute 0.5 M NaCl (pH=6) solution. HCl and 0.1 M NaOH were used to adjust the electrolyte pH. Highly concentrated 5 M NaCl solution is used in industrial conditions because selectivity of $Cl_2$ gas increases with an increase in $Cl^-$ concentration, and >97 % selectivity was measured when 4 M NaCl solution was used. In the membrane cells, the concentration of NaCl in the feed brine is about 300 g $L^{-1}$. The pH value is maintained at ~2 because pH <2 can likely dissolve the Ti and metal elements. When the pH is >2, the selectivity towards oxygen evolution reaction increases and dissolution of anodes occurs under alkaline conditions[12, 23]. For dilute chloride solutions, 0.5 M NaCl is chosen

considering, the lower concentration of [$Cl^-$] = 0.5 M and higher pH of 8 in the sea water[14]. However, the pH value is maintained at 6 in this work instead of 8 to avoid the corrosion of the carbon substrate[24, 25]. Linear sweep voltammetry (LSV) tests were performed to measure the catalytic activity between the potential range of 0 V – 1.3 V vs. Ag/AgCl. However, proper growth of the diffusion layer and stable potential measurement is not possible in LSV, which causes a huge difference in overpotential compared to the steady state technique. Thus, short-term chronopotentiometry was performed at different current density ranges (10 mA $cm^{-2}$ to 200 mA $cm^{-2}$) and the measured potentials were used to compare the overpotential from the long term steady state measurements, such as chronopotentiometry. The charge transfer resistance ($R_{ct}$) values were obtained from the electrochemical impedance spectroscopy measurements (EIS), conducted at a fixed potential of 1.45 V in the faradaic region without iR compensation from 1,000,000 Hz to 0.1 Hz with a potential amplitude of 10 mV. The electrochemically active surface area is calculated based on the double-layer capacitance ($C_{dl}$) value. The double layer capacitance is determined by performing cyclic voltammetry in the non-faradaic potential in the range of 0.8 to 0.9 V vs Ag/AgCl at different scan rates (20, 40, 60, 80, and 100 mV $s^{-1}$).

The electrodes selectivity towards CER and OER in acidic electrolyte was verified through LSV and short-term CP tests in CER (5 M NaCl) and OER ($H_2SO_4$) electrolytes at same pH=2. The interference of OER during the CER was identified from the measured potential values. Whereas the chlorine content in dilute solutions was measured using the DPD (N,N-diethyl-p-phenylenediamine) colorimetric method with a pocket INESA portable chlorine meter (515 nm LED light source, DGB-402F) to calculate the faradaic efficiency of the CER. A constant current was applied through chronopotentiometry for 180 seconds. The reactor was well sealed, and the reaction was performed under stirring (400 rpm) to dissolve the evolved chlorine gas. The

electrolyte was then diluted ten times with DI water in a vial, and the DPD reagents were added to the solution, which produces a transparent pink colour after reacting with chlorine species. Finally, the concentration is automatically quantified by the chlorine meter by calculating the difference in absorbance. The Faradaic efficiency is then calculated using the following equation[25]:

$$FE = \frac{2 \times \left[Cl_{2,\,DPD}\right] \times V \times F}{i \times t} \times 100 \qquad \textbf{3.4}$$

Where, $Cl_{2,DPD}$ = Molar concentration of active chlorine (mol $L^{-1}$), V = volume of the electrolyte (L), F = Faraday's constant (96485.3 C $mol^{-1}$), i = current applied (A), and t = time of electrolysis (s).

# Chapter 4. Results and Discussion

## 4.1 Investigation of analytical properties

Based on the detailed literature survey, the following five elements, such as Ru, Sn, Ti, V, and Co have been chosen to prepare the high entropy oxide, as they either directly or indirectly participate in enhancing the catalytic performance of the electrode in CER. The elements such as Ru, V, and Co exhibit high catalytic activity towards CER[56, 57]. The presence of Ti in the composite can alter the binding energy to selectively adsorb $Cl^-$ ions favoring CER, while the presence of Sn could weaken the $OH^-$ adsorption energy and also shifts the overpotential of OER towards more positive potentials[11, 79]. The XRD pattern of HEO-R sintered at 500 °C (HEO-R-500) is shown in **Figure 4.1**. Major diffraction peaks present at 27.38°, 35.53°, 39.16°, 40.88°, 44.0°, 54.06°, 56.48°, 64.05°, and 68.70° correspond to the (110), (101), (200), (111), (210), (211), (220), (310), and (301) planes of the rutile structure (P42/mnm space group) and confirms the formation of a solid solution[14, 94]. Some minor impurities can be observed at 22.60° and 33.94° corresponding to $Ti_6O_{11}$ probably formed from the high-temperature calcination.

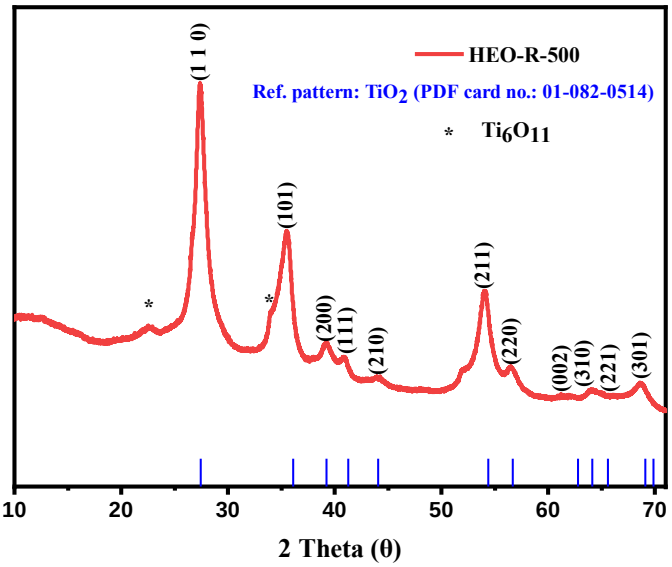


Figure 4.1: XRD patterns of HEO-R sintered at 500 °C.

More information can be observed from the compiled XRD patterns of the HEO-R precursor calcinated at 350 °C, 400 °C, 500 °C, 600 °C and 700 °C, as shown in **Figure 4.2**.

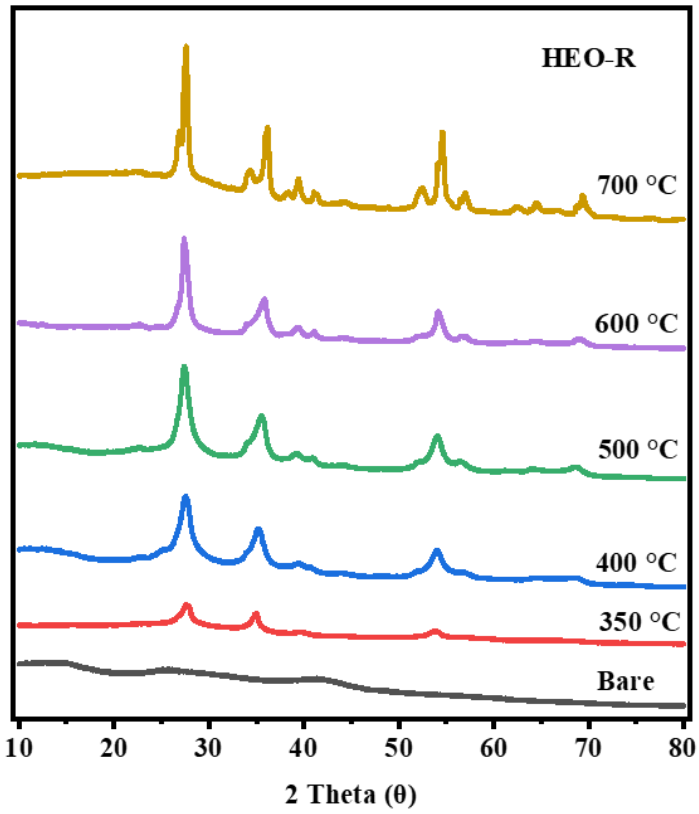


Figure 4.2: Comparison of XRD pattern of HEO-R precursor (Bare) and HEO-R sintered at 350 °C, 400 °C, 500 °C, 600 °C, and 700 °C.

There are no obvious crystalline peaks observed from the as-synthesized sample (HEO-R-Bare), indicating an amorphous phase through the formation of an organic-inorganic compound[125]. The sample sintered at 350 °C (HEO-R-350) shows no impurities, but its crystallinity is less than others because of the incomplete conversion of the precursor to oxides. Further increase in calcination temperature is necessary for obtaining pure oxides with high crystallinity, which has an impact on the catalytic activity. It is evident from the observed XRD patterns, that the crystallinity of the HEO-R increases with an increase in temperature. Only minor

differences can be observed in the XRD patterns for the samples calcinated at 400 °C, 500 °C, and 600 °C. On the other hand, when the temperature was increased to 700 °C, many additional peaks are observed comparing with others, indicating the formation of a multiple phase and the loss of prominent rutile structure. The multiple phases present in HEO-R-700 are related to $Ti_{0.9}Sn_{0.1}O_2$ (PDF card no.: 01-070-4403), $Ti_{0.2}Sn_{0.8}O_2$ (PDF card no.: 01-070-4410), $TiVO_4$. (PDF card no.: 01-077-0332). Similar pattern have been observed in other works[12, 119, 126].

Transmission electron microscopy (TEM) has been performed for HEO-R-350, HEO-R-500, and HEO-R-700. TEM has not been analyzed for HEO-R-400 and HEO-R-600, as there is not much difference in their XRD patterns compared to HEO-R-500. The TEM images of HEO-R-350 displayed in **Figure 4.3 (a)** shows that the particles are highly agglomerated and an intermixture of a crystalline - amorphous phase is observed. The high-resolution images (**Figures 4.3 b and c**) further confirm the presence of an intermixture of crystalline oxides and amorphous HEO precursor materials. This is because of the incomplete conversion of the HEO precursor to oxides, as reflected by the less crystalline XRD pattern of HEO-R-350. Because of the existence of the crystalline-amorphous phase, it was challenging to observe the individual particles and hence the average particle size has not been measured. The elemental composition is analyzed through TEM point EDS analysis, and it confirms that all the elements added are present in the synthesized HEO-R-350 in a non-equimolar ratio. Compared to all other elements, Co is present in a significantly lower concentration.

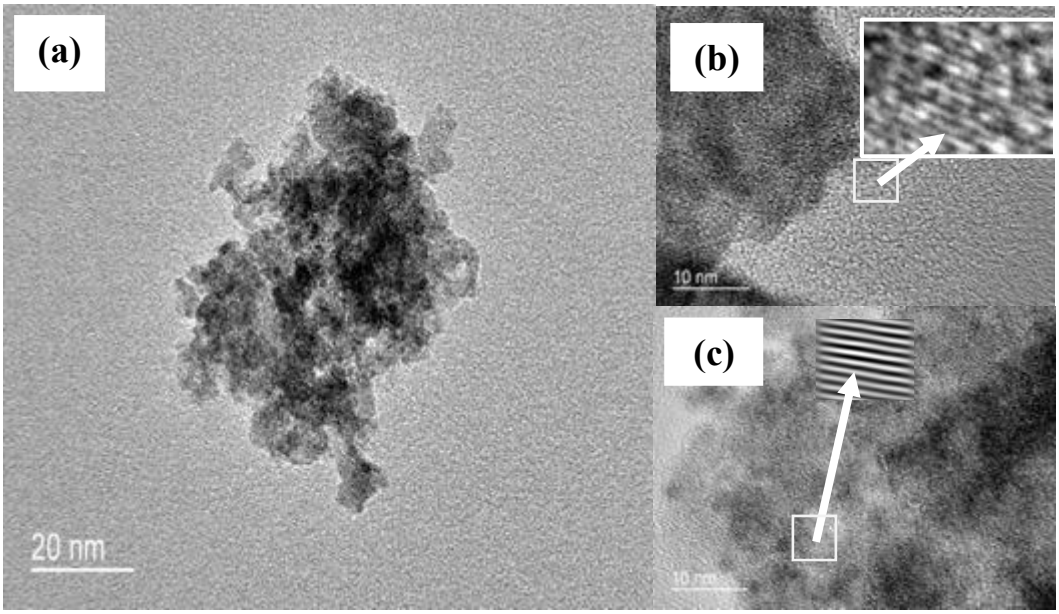


Figure 4.3: (a) TEM image of the HEO-R sintered at 350 °C, (b) high-resolution images of HEO-R-350 with inset figure showing the diffraction pattern.

Table 4.1: Atomic percentage (at%) of HEO-R-350 analyzed through TEM point EDS analysis.

| **Elements** | **Atomic Percentage (at%)** |
|---|---|
| Ru | 9.33 |
| Sn | 6.62 |
| Ti | 14.12 |
| V | 10.01 |
| Co | 0.13 |
| O | 59.79 |

After increasing the calcination temperature to 500 °C, the particles (HEO-R-500) are clearly observed without any amorphous phase but are still agglomerated (**Figure 4.4 a)**. The HRTEM analysis (**Figures 4.4 b - f**) displays the lattice fringes with a spacing of 0.318 nm, 0.251 nm, and 0.167 nm that are related to the (110), (101), and (211) crystal planes of the rutile structure. All the observed planes are related to the three major peaks present at 27.38°, 35.6°, and 54.10° in the

XRD pattern of HEO-R-500, further confirming the formation of a single-phase rutile structure. The polycrystalline nature of HEO-R-500 can be well observed from the clear diffraction rings from the SAED pattern shown in **Figure 4.4 (g)**. The particle size distribution histogram shown in **Figure 4.4 (h)** reveals that, the average particle size of HEO-R-500 is in the range of 10nm - 15nm. The presence of nanoparticles are advantageous for obtaining high catalytic activity, as a result of their large surface area with increased active sites and rapid electron transfer[119].

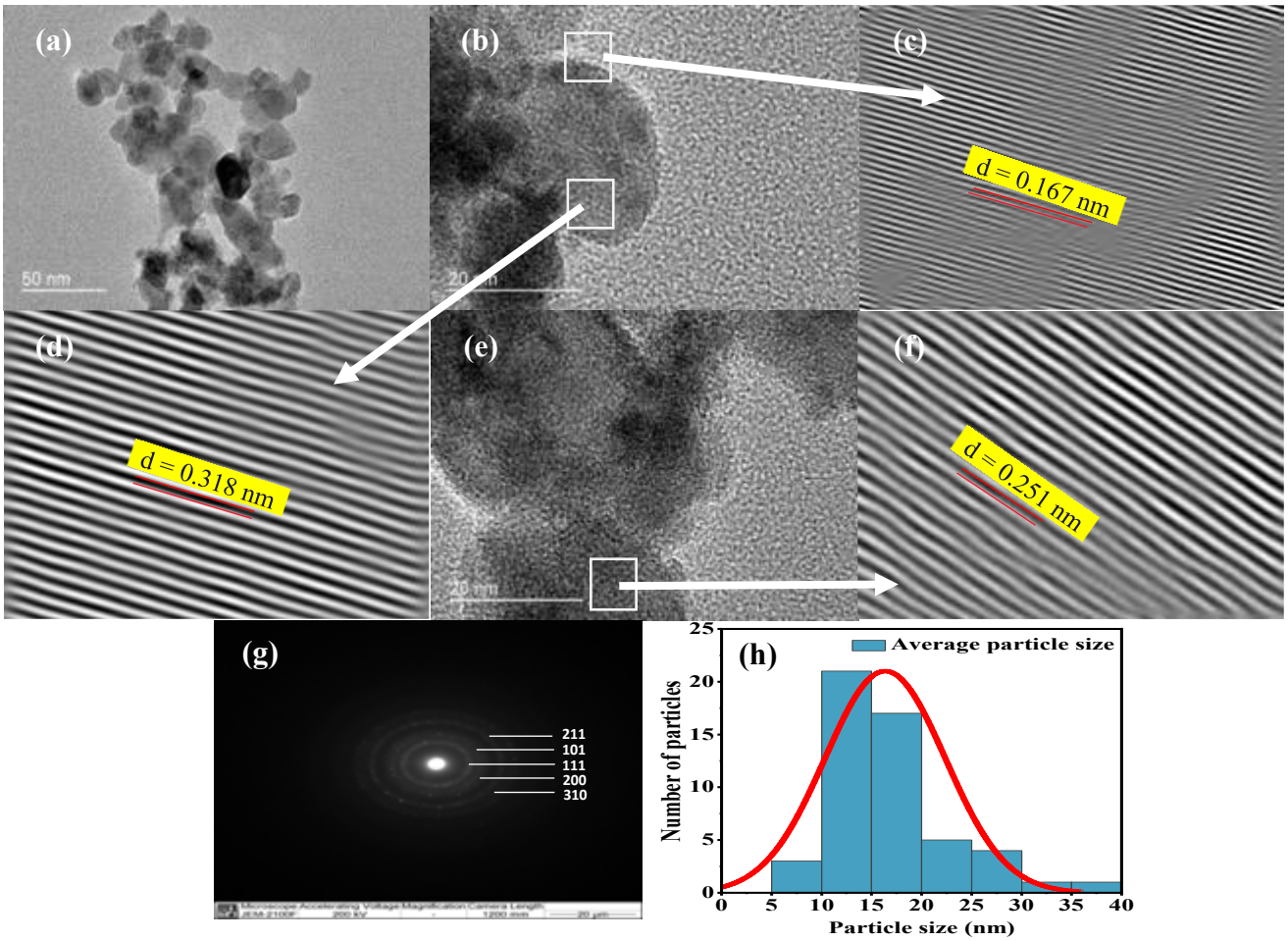


Figure 4.4: (a) TEM image of the HEO-R-500; (b) high resolution image (1) of HEO-R-500; (c) Enlarged image of diffraction pattern of fig (b); (d) Enlarged image of diffraction pattern of fig (b); (e) high resolution image (2) of HEO-R-500; (f) Enlarged image of diffraction pattern of fig (e); (g) SAED pattern; (h) Particle size distribution histogram of HEO-R-500.

The STEM-EDS mapping has been performed to analyze the dispersion of the elements in the HEO-R-500 (**Figure 4.5).** A uniform dispersion of Ru, Sn, Ti, and V has been observed, while the density of Co seems to be low. The presence of low concentration of cobalt might be due to the incompatibility of the synthesis process, or the cobalt ion was not able to diffuse into the rutile structure because of their difference in the cationic radii. Additionally, TEM point EDS analysis confirms the presence of all the elements similar to the HEO-R-350, but with a difference in their concentration, that might be because of the high calcination temperature (**Table 4.2**).

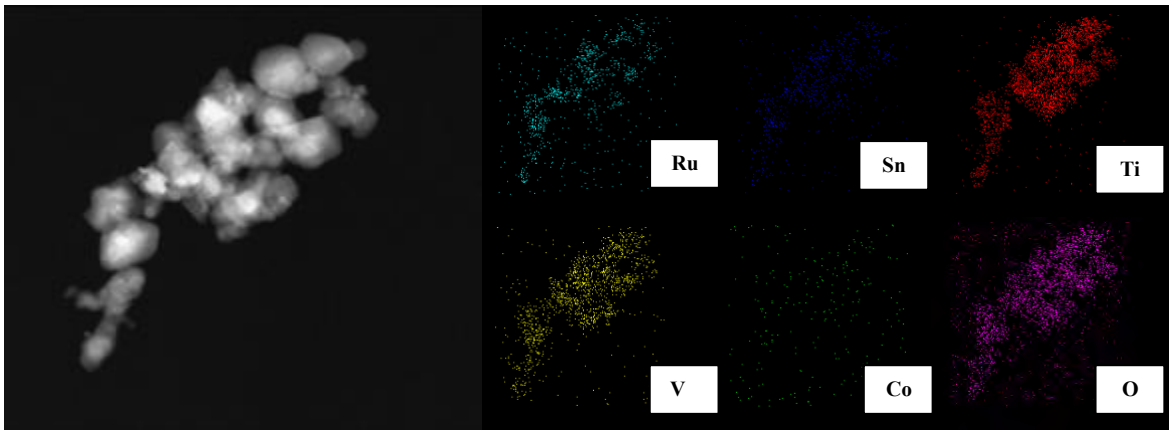


Figure 4.5: STEM-EDS mapping of HEO-R-500.

Table 4.2: Atomic percentage (at%) of HEO-R-500 analyzed through TEM point EDS analysis.

| **Elements** | **Atomic percentage (at%)** |
|---|---|
| Ru | 9.87 |
| Sn | 7.03 |
| Ti | 22.33 |
| V | 8.22 |
| Co | 0.14 |
| O | 52.41 |

When the temperature was increased to 700 °C, highly crystalline particles with increase in the particle size has been observed (**Figure 4.6**). The observed particles are two to three times bigger than the particle size of HEO-R-500, which might result in decreased catalytic activity. **Table 4.3** lists the concentration of the elements presents in HEO-R-700, obtained through the EDS analysis. Comparing to the HEO-R-350 and HEO-R-500, the elemental concentration in HEO-R-700 is highly non-equimolar. It can be observed that, the non-equimolar ratio increases with an increase in the calcination temperature, along with the formation of multiple phases. However, high temperature calcination is necessary to remove the amorphous phase and also to obtain crystalline metal oxides.

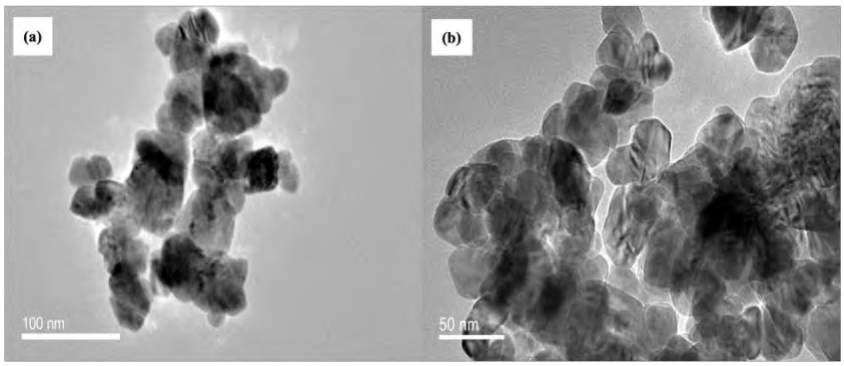


Figure 4.6: (a and b) TEM images of HEO-R-700.

Table 4.3: Atomic percentage (at%) of HEO-R-500 analyzed through TEM point EDS analysis.

| **Elements** | **Atomic percentage (at%)** |
|---|---|
| Ru | 41.33 |
| Sn | 8.56 |
| Ti | 7.53 |
| V | 17.95 |
| Co | 0.31 |
| O | 24.31 |

The surface states of HEO-R-500 are analyzed through X-ray photoelectron spectroscopy (XPS), and the elements Ru, Ti, Sn, V, and Co are observed in the complete survey spectrum shown in the **Figure 4.7**. The Ruthenium 3d spectrum is shown in **Figure 4.8 (a)**. The peaks present at 284.98 eV and 280.93 eV are assigned to the Ru $3d_{3/2}$ and Ru $3d_{5/2}$ of $Ru^{4+}$ oxidation state. The intensity of Ru $3d_{5/2}$ is much less than Ru $3d_{3/2}$, contradictory to the observed spectrum for pure $RuO_2$. The decreased intensity is because of the addition of other metals resulting in smaller content of Ru in the composite, as compared to the pure $RuO_2$. The satellite peak observed at 286.65 eV also corresponds to the binding energy of $Ru^{4+}$ oxidation state[70, 73, 127]. Also, less Ru content in a mixed oxide material is beneficial in promoting the electrocatalytic activity of the anode as a result of charge transfer induced activation of $RuO_2$ to $RuO_2^{\delta+}$ by other elements, which has been proved in the $(Ru_{1-x} - Ti_x)O_2$ coatings[73]. The Ti 2p spectrum shows the Ti $2p_{3/2}$ and Ti $2p_{1/2}$ of the $4^+$ oxidation state at 458.38 eV and 463.86 eV (**Figure 4.8 b**). A small amount of Ti is also present in the $Ti^{3+}$ state, noted from the satellite peak at 461.967 eV related to the Ti $2p_{1/2}$, creating oxygen defects[3, 70, 73, 121, 128]. Sn is present in 4+ state, confirmed by the location of peaks with binding energies of 486.19 eV and 494.7 eV related to the Sn $3d^{5/2}$ and Sn $3d^{3/2}$ [129] (**Figure 4.8 c**). As the binding energy is less than pure $SnO_2$, there are high possibilities for the presence of $Sn^{2+}$, creating oxygen vacancies[130]. Two valence states are found in the V 2p spectrum, in which the peaks at 516.60 eV and 523.45 eV correspond to the V $2p^{3/2}$ and $V2p^{1/2}$ of the $V^{4+}$ oxidation state. While the minor contribution of two peaks present at 517.10 eV is assigned to the V $2p^{3/2}$ related to the $V^{5+}$ oxidation state, that might be due to the presence of a small amount of $V_2O_5$ (**Figure 4.8 d**), originated from the air oxidation of the surface or due to the high-temperature calcination[131-134]. The presence of cobalt is confirmed by the presence of the Co 2p in the complete XPS survey spectrum. As the concentration of cobalt in the HEO-R-500 composite is

much less, the intensity of the peaks is very low, making it difficult to identify the oxidation states. The less concentration of cobalt is because of the poor diffusion of Co ions into the rutile structure. Deconvolution of the O 1s XPS spectrum resulted in three peaks at 529.92 eV, 532.41eV, and 533.39 eV. The lower binding energy peak at 529.92 is related to the lattice oxygen because of the metal-oxygen (M-O) bond. The peak centered at 532.41 eV corresponds to the oxygen vacancies and surface adsorbed hydroxyl group[128, 135, 136]. The peaks present at 533.39 eV raised as a result of adsorption of water ($H_2O$) molecules[137] (**Figure 4.8 e**). Except for cobalt, a major concentration of all the elements is present in the 4+ oxidation state and the above results confirm the successful solid solution, which will be beneficial for increase in resistance against corrosion.

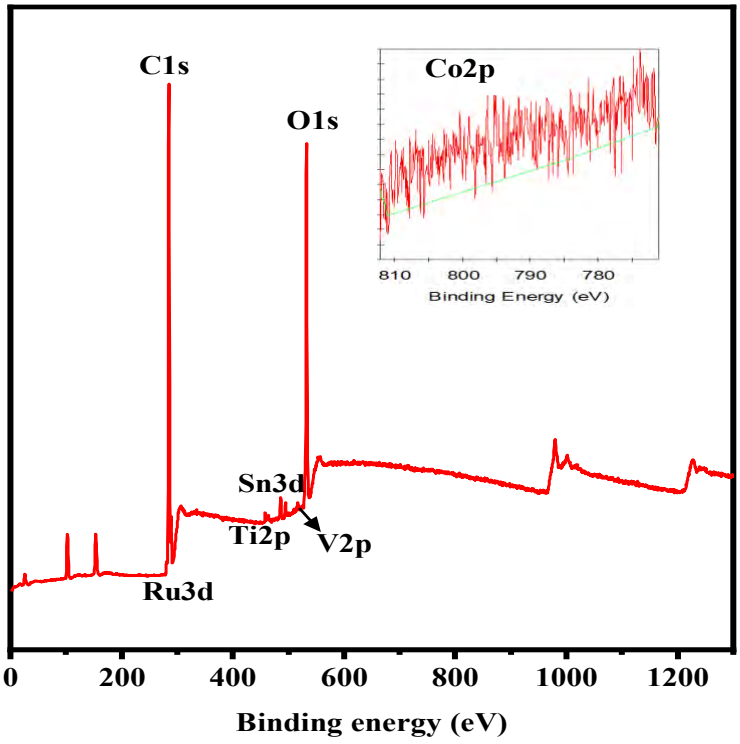


Figure 4.7: Complete XPS survey spectrum of HEO-R-500.

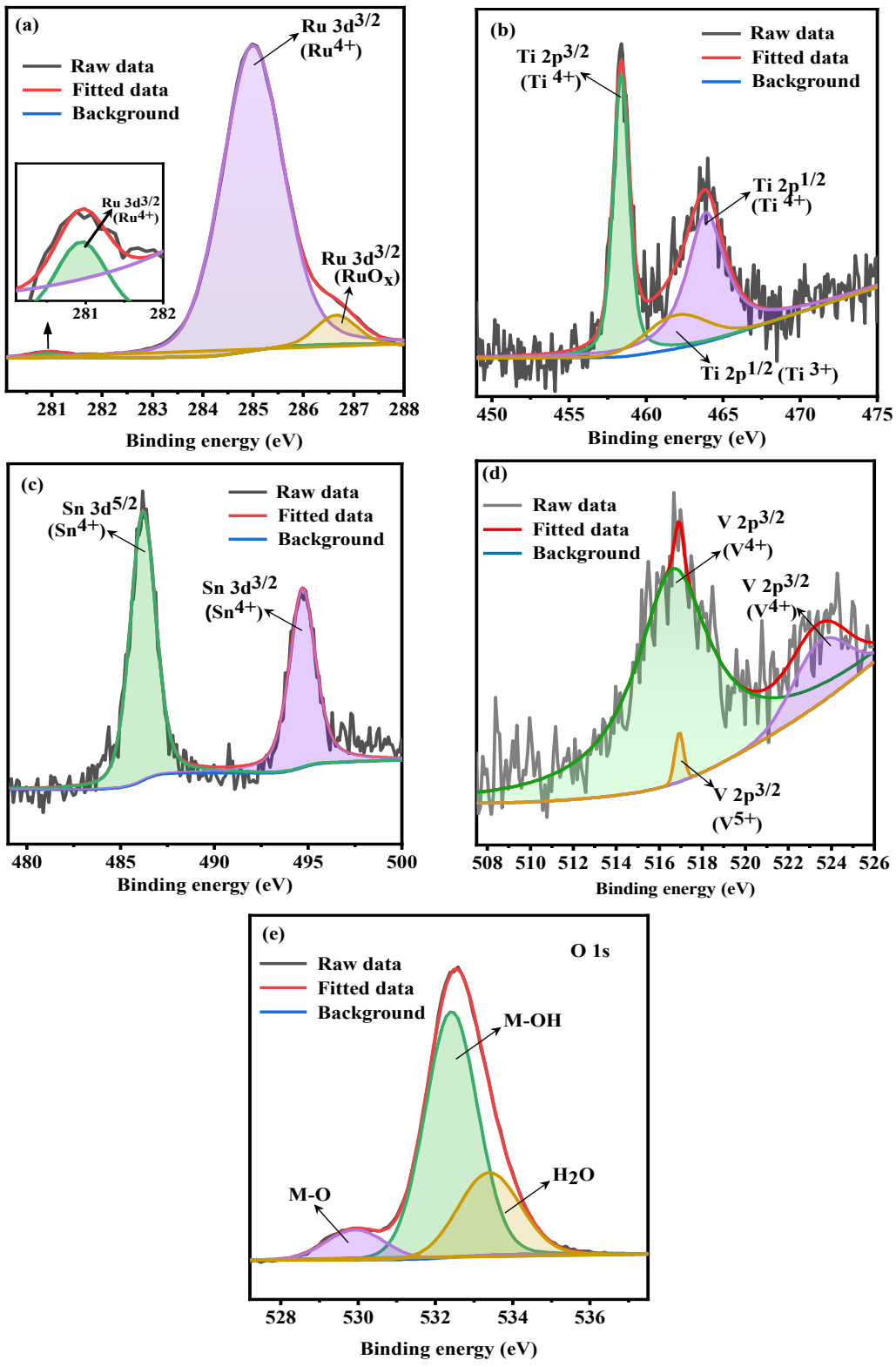


Figure 4.8: XPS profiles of Ru, Sn, Ti, V, Co, and O in HEO-R-500.

## 4.2 Evaluation of the electrocatalytic performance of HEO-R for CER

All the electrochemical measurements were carried out in a 100 mL H-type electrolytic cell at room temperature (25 °C) unless otherwise specified. Chlorine ($Cl_2$) production from saturated acidic NaCl solution is the first and foremost important process in the chlor-alkali industry. Thus, the electrochemical performance of HEO-R (350, 500 and 700) was evaluated in a 5 M NaCl solution (pH=2), followed by testing in the dilute solutions (0.5 M NaCl, pH=6). To clean the surface of the electrode and make it wet, a cyclic voltammogram (CV) was performed between 0.30 V to 1.315 V at a scan rate of 500 mV $s^{-1}$, until the capacitive current on the positive and negative peak potential regions are stable. **Figure 4.9** illustrates the cyclic voltammogram profiles of HEO-R-350, HEO-R-500 and HEO-R-700 for 50 cycles in the non-faradaic region. All the electrodes delivered an equal oxidation and reduction current at the end of the test suggesting that, the electrode surface is completely wet and free of impurities. The apparent fluctuation in the measured current response in the initial cycles of HEO-R-700 might be because of the surface coverage of metal cations with different valence states emerging from the multiple phases confirmed by the XRD patterns. These cations undergo oxidation/reduction during the CV resulting in fluctuating oxidation/reduction current. Even though the CV was performed in the non-faradaic region of CER to improve electrode surface wettability, the adsorption current measured from HEO-R-500 is higher compared to the HEO-R-350 and HEO-R-700, indicating the presence of more active sites.

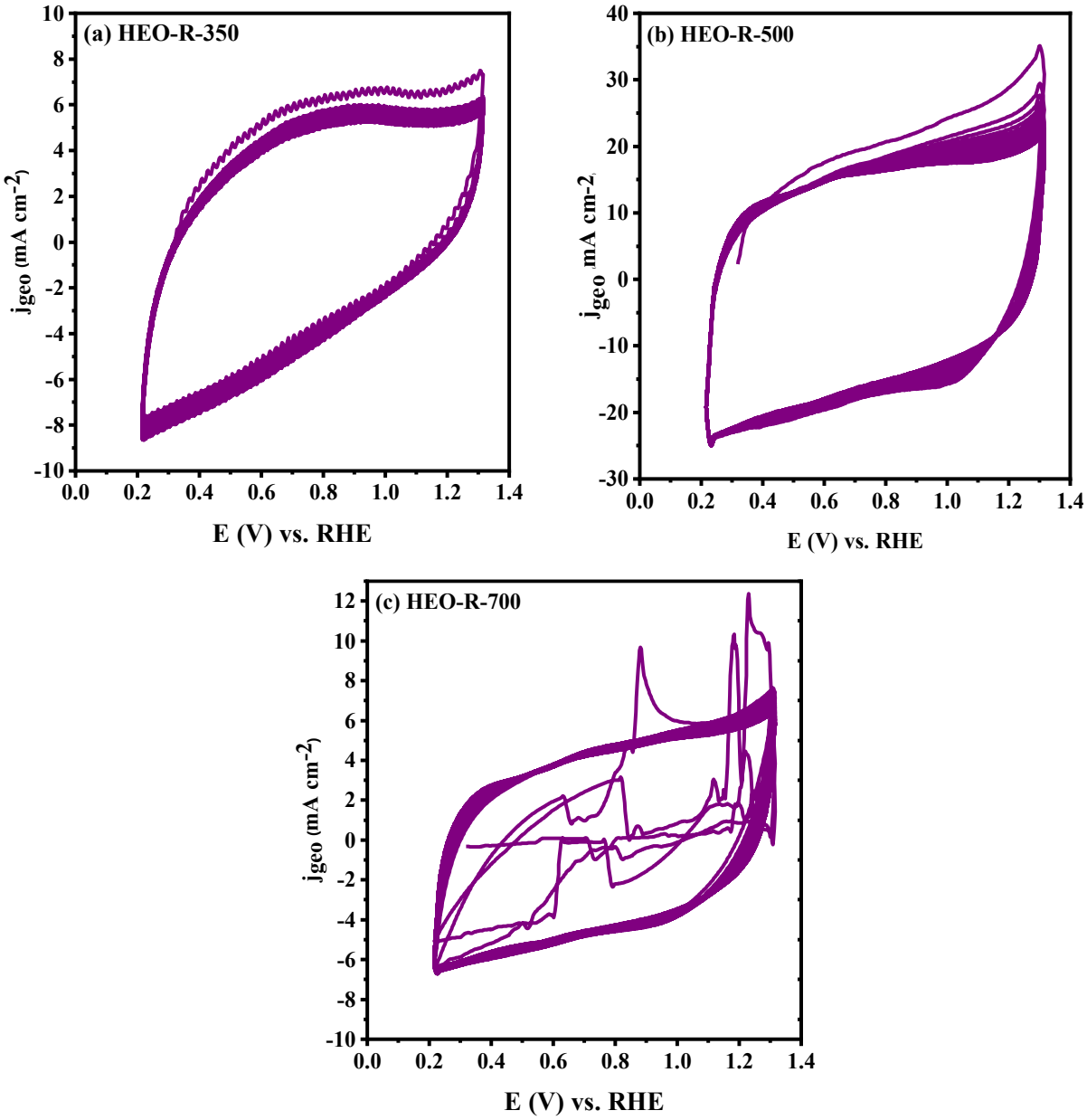


Figure 4.9: Cyclic voltammograms for impurity removal and wetting of electrodes.

The current/voltage (i/V) values of the HEO-R-350, HEO-R-500 and HEO-R-700 were investigated through LSV at a scan rate of 10 mV $s^{-1}$ in a 5 M NaCl (pH=2) electrolyte as shown in **Figure 4.10.**

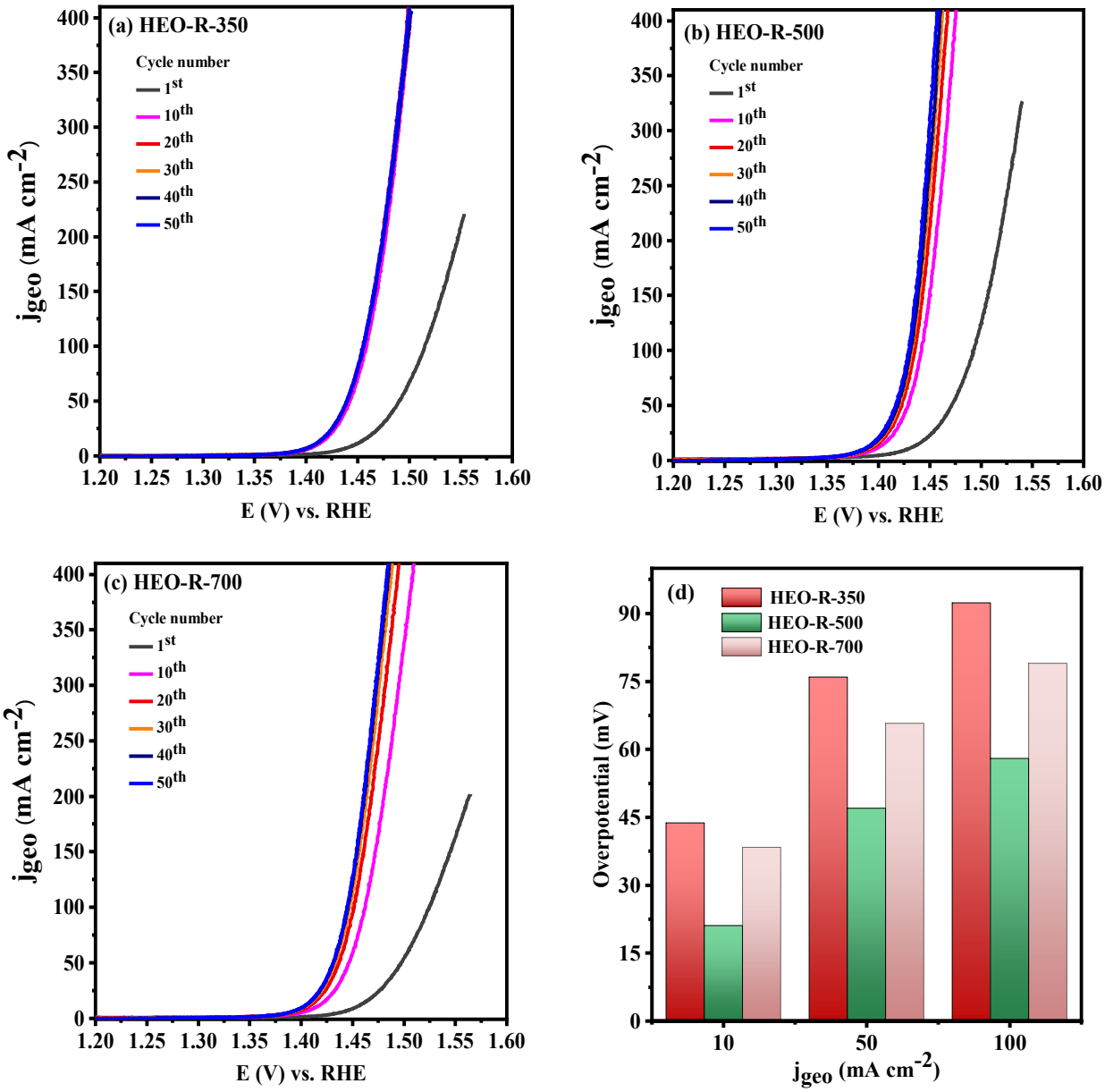


Figure 4.10: LSV polarization curves of (a) HEO-R-350, (b) HEO-R-500, and (c) HEO-R-700 in 5 M NaCl solution (pH=2), (d) Comparison of overpotential of HEO-R-300, HEO-R-500 and HEO-R-700 to reach 10, 50, and 100 mA $cm^{-2}$.

Comparing all the LSV graphs (**Figures 4.10 a-c**), it is clear that the electrodes require a certain period of time to get completely activated and to deliver a stable performance. It is because

of the incomplete wetting of the electrode, the activity in the initial stage low and increases with increase in electrode wettability during the electrochemical reaction[36]. It took approximately more than 35 LSV cycles for all the electrodes to get completely wet to reach a stable current density and potential value. No changes in the current density values have been observed between 35 - 50 cycles, indicating the complete activation of the electrodes. **Figure 4.10 (d)** compares the overpotential required for reaching 10, 50, and 100 mA $cm^{-2}$ for the fabricated electrodes. Based on the LSV curves, HEO-R-350 requires an overpotential of 32 mV, 64 mV, and 80 mV while the HEO-R-700 required an overpotential value of 26 mV, 56 mV, and 69 mV to reach 10, 50, 100 mA $cm^{-2}$. Whereas, the HEO-R-500 only needed 10 mV, 42 mV, and 54 mV overpotential to deliver 10, 50, 100 mA $cm^{-2}$, less than both the HEO-R-350 and HEO-R-700. The lesser activity of HEO-R-350 is because of its less crystallinity and the presence of a mixed organic-inorganic phase, resulting in fewer active sites, which is evident from the XRD patterns and TEM images. Although the crystallinity of the HEO-R-700 is higher compared to the HEO-R-350 and HEO-R-500, it delivers lower catalytic activity comparing to the HEO-R-500. It is because of the high temperature calcination, the material lost its single phase in addition to the formation of an larger particle size[126]. The presence of multi-elements in a single lattice can alter the electronic structure of the catalyst and the cationic size difference causes an lattice constraint that creates more active sites and oxygen vacancies[18-20]. Additionally, the presence of nanoparticles results in exposing a large number of active sites thereby improving the CER activity of the catalyst[119, 120]. This confirms that, the combined effect of the presence of a single phase, high crystallinity, and the smaller particle size (> 20 nm) in HEO-R-500, is the driving force for obtaining high catalytic activity at low overpotential.

Nevertheless, the LSV is transient, and the current/voltage (I/V) profile obtained from them might differ from the values measured during steady state electrolysis conditions, such as chronopotentiometry. Even a small difference in overpotential will have a significant impact on the energy efficiency and production cost in the industrial electrolysis process[138]. Thus, a series of chronopotentiometry tests were performed for HEO-R-350, HEO-R-500 and HEO-R-700 at 10, 50, 100, 200, and 300 mA $cm^{-2}$ for 300 seconds to identify the actual potential values required by these anodes **(Figure 4.11)**.

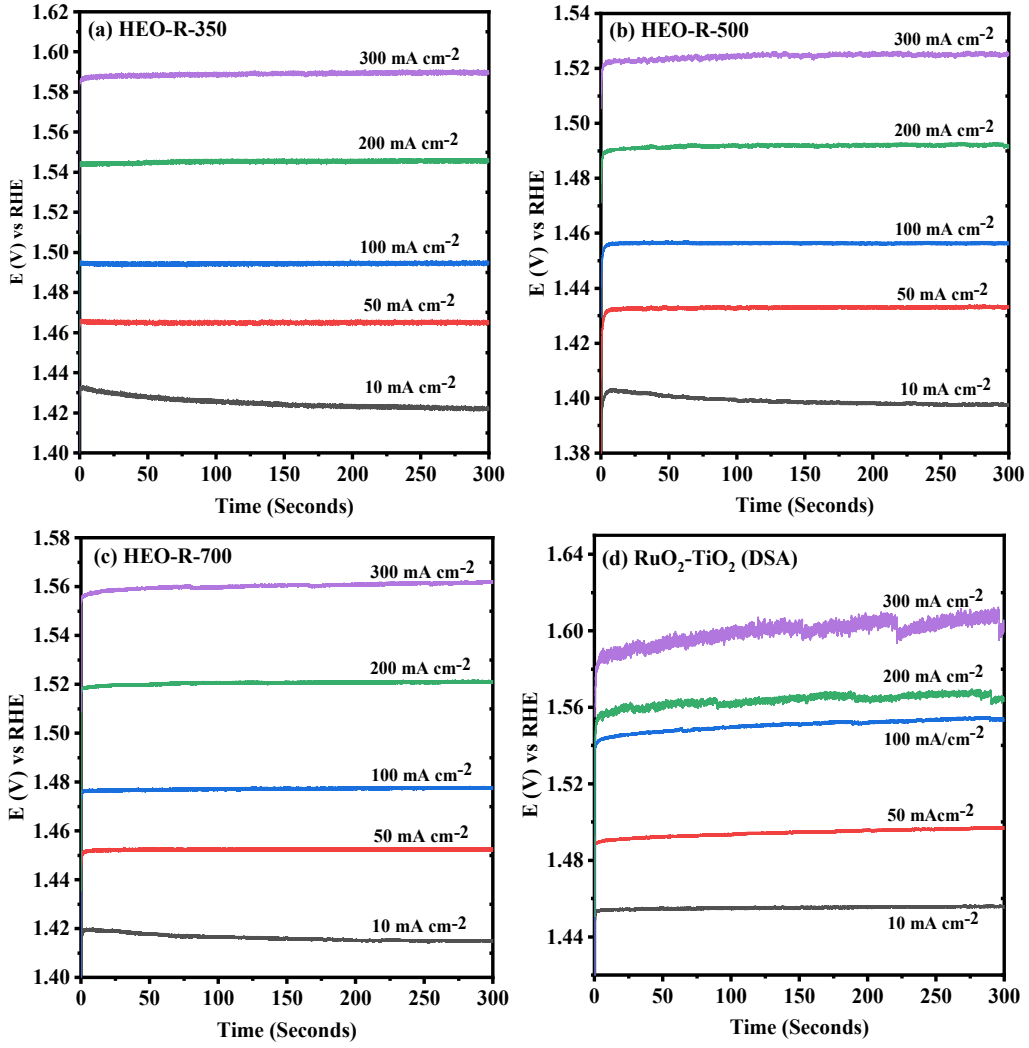


Figure 4.11: Comparison of chronopotentiometry test of HEO-R-350, HEO-R-500, HEO-R-700, and $RuO_2$-$TiO_2$ (DSA).

| Table 4.4: Overpotential comparison between LSV and CV profiles | | | | | | | | |
|---|---|---|---|---|---|---|---|---|
| | HEO-R-350 | | HEO-R-500 | | HEO-R-700 | | $RuO_2$-$TiO_2$ (DSA) | |
| j ($mA\ cm^{-2}$) | LSV ( η ) (mV) | SCV ( η ) (mV) | LSV ( η ) (mV) | SCV ( η ) (mV) | LSV ( η ) (mV) | SCV ( η ) (mV) | LSV ( η ) (mV) | SCV ( η ) (mV) |
| 10 | 32.0 | 43.70 | 12.9 | 21.0 | 26.3 | 38.3 | 68 | 80 |
| 50 | 64.80 | 75.90 | 42.0 | 47.0 | 56.3 | 65.7 | 101 | 121 |
| 100 | 80.40 | 92.30 | 54.4 | 58.8 | 96.06 | 79.0 | 123 | 179 |
| 200 | 99.30 | 115.0 | 66.3 | 71.1 | 85.5 | 97.2 | 163 | 189 |
| 300 | 113.1 | 130.0 | 74.4 | 82.3 | 97.6 | 113.5 | - | 226 |

**Figure 4.11** depicts that all the electrodes maintain a stable electrode potential over a range of applied current densities (10 – 300 mA $cm^{-2}$). Similar to the LSV results, the HEO-R-500 requires less overpotential to reach the applied current density values compared to the HEO-R-350 and HEO-R-700. However, the difference in the service life of the electrodes in acidic NaCl electrolytes are difficult to be analyzed from the short-term chronopotentiometry tests, because the rate of corrosion of the electrodes is slow, as compared to the dilute electrolytes[126]. **Table 4.4** compares the overpotential between HEO-R-300, HEO-R-500, and HEO-R-700, where more than 10 % difference in the overpotential observed between the LSV and the short-term chronopotentiometry tests. As the LSV technique cannot be used to obtain more accurate current/potential results, the overpotential values obtained from the short-term chronopotentiometry tests can be used for comparison with other works[37]. The catalytic activity and the overpotential of the HEO-R-500 have also been compared with the state-of-art commercial $RuO_2$-$TiO_2$ dimensionally stable anodes (DSA).

Compared to the $RuO_2$-$TiO_2$ (DSA), the HEO-R-500 delivers 20 times more current density at 1.45 V (**Figure 4.12 a**), suggesting that the fabricated anode has more active sites available for reaction and also an efficient electron transfer. The lower performance of the DSA is because of the less available active sites on the surface. The overpotential comparison between the HEO-R-500 and commercial DSA suggests that the kinetics of HEO-R-500 is superior to that of the commercially available catalysts (**Figure 4.12 b**).

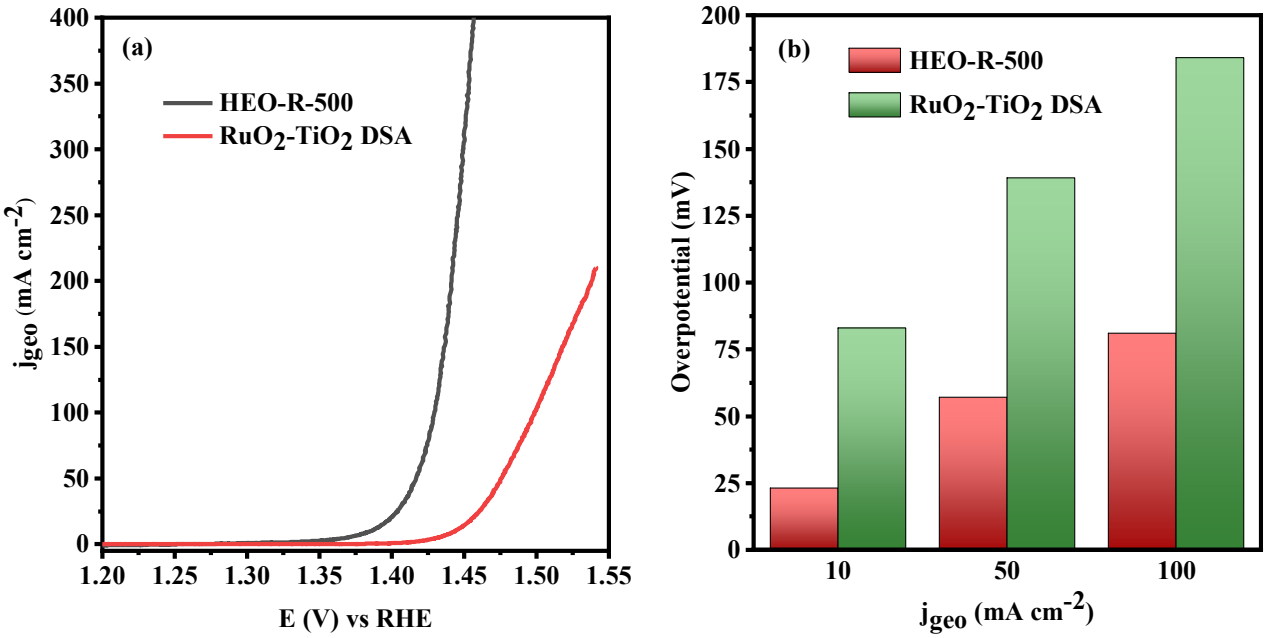


Figure 4.12: Comparison between HEO-R-500 and commercial $RuO_2$-$TiO_2$ (DSA), (a) LSV curves, (b) overpotential values obtained from short-term chronopotentiometry tests.

Tafel slope was calculated, as they are one of the important parameters to reveal the kinetics of the reaction and also the mechanism of the undergoing CER. The i/V values obtained from the short-term chronopotentiometry tests without iR correction were used, as they represent the practical potential values for the catalytic reaction to occur. The overpotential value was calculated in three different current density regions to understand their kinetics from lenient to rigorous

operating conditions, such as 10 to 40 mA $cm^{-2}$, 50 to 90 mA $cm^{-2}$, and 100 to 150 mA $cm^{-2}$ (**Figure 4.13**).

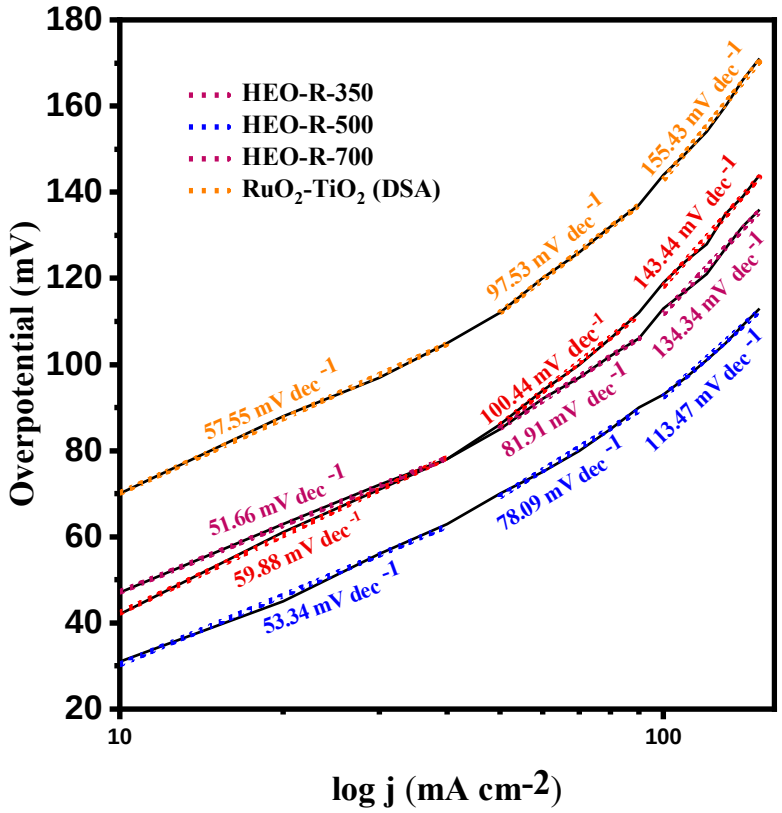


Figure 4.13: Comparison of Tafel slope vales determined from the sampling cyclic voltammetry test for HEO-R-350, HEO-R-500, HEO-R-700, and $RuO_2$-$TiO_2$ (DSA).

All the samples had a nearly similar Tafel slope value in the range of 50 mV $dec^{-1}$ – 60 mV $dec^{-1}$ in the 10 mA $cm^{-2}$ to 40 mA $cm^{-2}$ current density region, with HEO-R-700 being the lowest at 51.66 mV $dec^{-1}$. When the current density was increased to 50 mA $cm^{-2}$ – 90 mA $cm^{-2}$ and 100 mA $cm^{-2}$ to 150 mA $cm^{-2}$, the lowest Tafel slope values of 78.09 mV $dec^{-1}$ and 113.47 mV $dec^{-1}$ were estimated for the HEO-R-500, while comparing to the HEO-R-350 (100.44 mV $dec^{-1}$ and 143.44 mV $dec^{-1}$), HEO-R-700 (81.91 mV $dec^{-1}$ and 134.34 mV $dec^{-1}$), and the $RuO_2$-$TiO_2$ (DSA) (97.53 mV $dec^{-1}$ and 155.43 mV $dec^{-1}$). This suggests that the kinetics of HEO-R-500 is superior,

which are consistent with the LSV and short-term chronopotentiometry tests. The Tafel slope values of the HEO-R-500 indicate that these electrodes favor the Volmer-Heyrovsky mechanism, with the Heyrovsky step being the rate-determining step.

Further, the charge transfer resistance values were measured using electrochemical impedance spectroscopy (EIS), as they reflect the true activity trends. The EIS values were obtained in the faradaic region (> 1.375 V), because there are no electron transfer reactions happening in the non-faradaic region. **Figure 4.14** displays the Nyquist plot obtained from the EIS graphs, recorded at 1.45 V vs RHE (no iR correction) in a 5 M NaCl solution (pH=2). Both the Nyquist plot and their respective charge transfer values ($R_{ct}$) mentioned in **Table 4.5** signify that the HEO-R-500 electrode has a smaller $R_{ct}$ compared to the other electrodes, as a result of an efficient charge transfer kinetics. The more the active sites are present, and the more efficient will be the electron transfer with a smaller $R_{ct}$, resulting in a very high catalytic activity. It also suggests the facilitation of the quick escaping of the $Cl_2$ bubbles[47]. In addition to the above, the comparison of the measured $R_{ct}$ values and the double layer capacitance ($C_{dl}$) value can be used as an indirect indicator of the electrochemically active surface area (ECSA). The electrode with smaller charge transfer resistance ($R_{ct}$) and higher double layer capacitance ($C_{dl}$) will have more active sites with high catalytic activity[37].

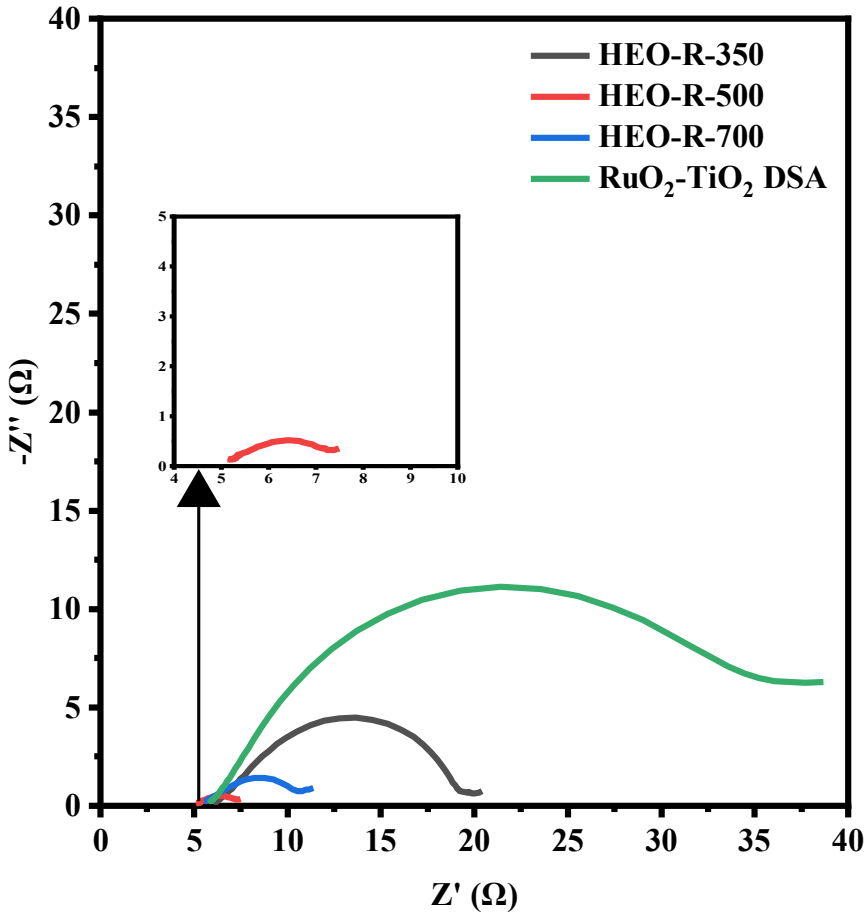


Figure 4.14: Comparison of charge transfer resistance from the EIS curves for HEO-350, HEO-500, HEO-700, and $RuO_2$-$TiO_2$ (DSA).

Table 4.5: Comparison of charge transfer resistance ($R_{ct}$) and double layer capacitance values ($C_{dl}$) for different anode materials

| **Anode material** | **Charge transfer resistance ($R_{ct}$) (Ω)** | **Double layer capacitance ($C_{dl}$) (mF $cm^{-2}$)** |
|---|---|---|
| HEO-R-350 | 13.3 | 44.37 mF $cm^{-2}$ |
| HEO-R-500 | 2.514 | 70.01 mF $cm^{-2}$ |
| HEO-R-700 | 7.0 | 34.39 mF $cm^{-2}$ |
| $RuO_2$-$TiO_2$ (DSA) | 31.7 | 4.235 mF $cm^{-2}$ |

The $C_{dl}$ values were calculated from the i-V profiles obtained from the CV tests performed at different scan rates, between 0.8 V - 0.9 V vs Ag/AgCl as shown in **Figure 4.15**. The linear fitting values of the capacitive current densities at 0.85 V vs Ag/AgCl were 44.37 mF $cm^{-2}$, 70.01 mF $cm^{-2}$, 34.39 mF $cm^{-2}$, and 4.235 mF $cm^{-2}$ for HEO-R-350, HEO-R-500, HEO-R-700, and commercial $RuO_2$-$TiO_2$ (DSA) (**Figure 4.16**). The $C_{dl}$ values of HEO-R-500 are nearly two times higher than the synthesized catalysts (HEO-R-350 and HEO-R-700) and ~16 times higher than the $RuO_2$-$TiO_2$ (DSA). The comparison of the $R_{ct}$ and $C_{dl}$ values indicates that, the active sites in the HEO-R-500 are higher, emerging from the combined effect of a complex interaction between the multi-elements present in the single phase rutile system and also the nano-particle size[18, 119, 120, 139]. Furthermore, the presence of vanadium could have reduced the band gap of the composite, thereby resulting in an efficient electron transfer[88].

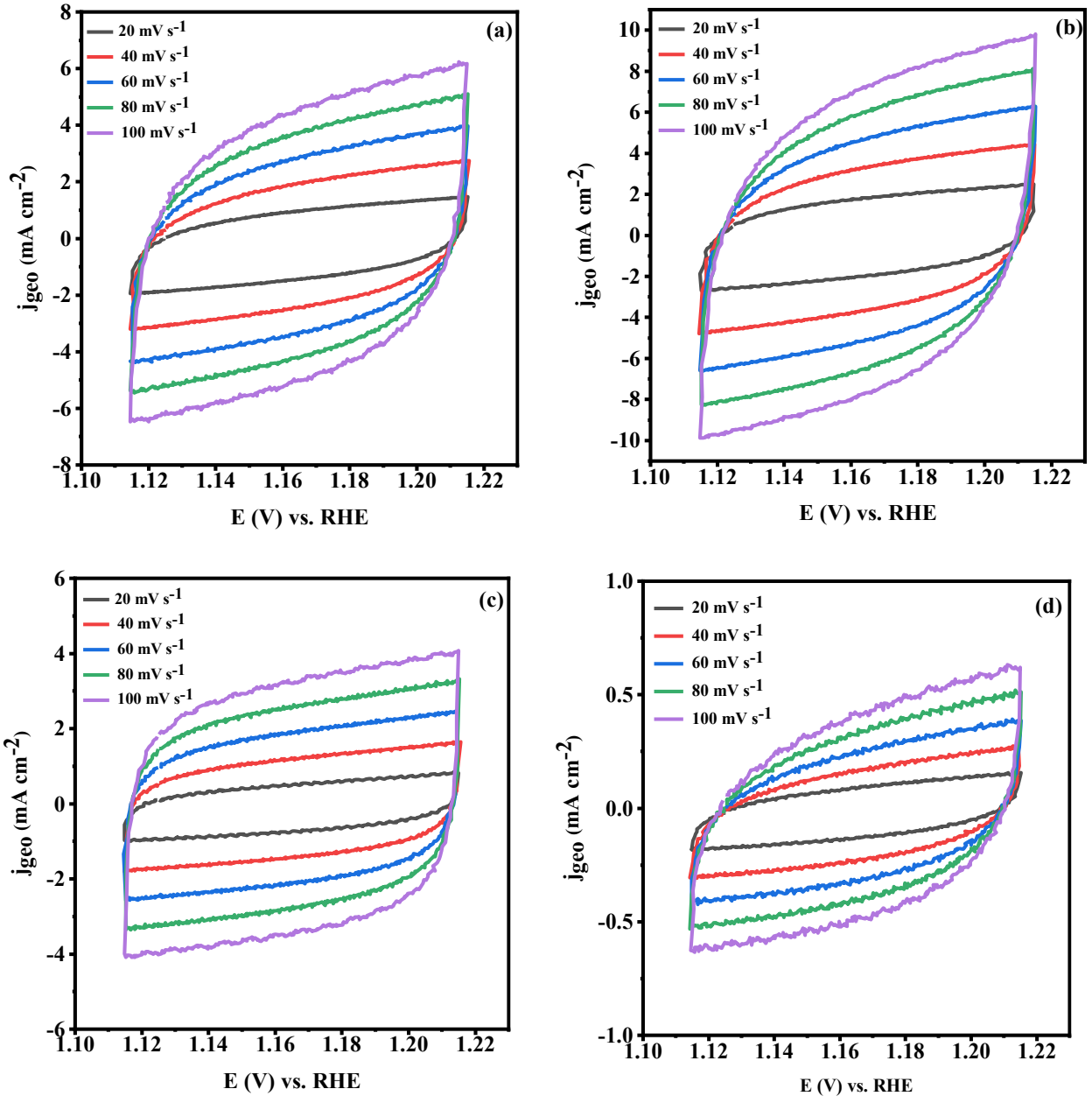


Figure 4.15: CV at varying scan rate and linear fitting of the capacitive current densities for (a) HEO-R-350, (b) HEO-R-500, (c) HEO-R-700, and (d) $RuO_2$-$TiO_2$ (DSA).

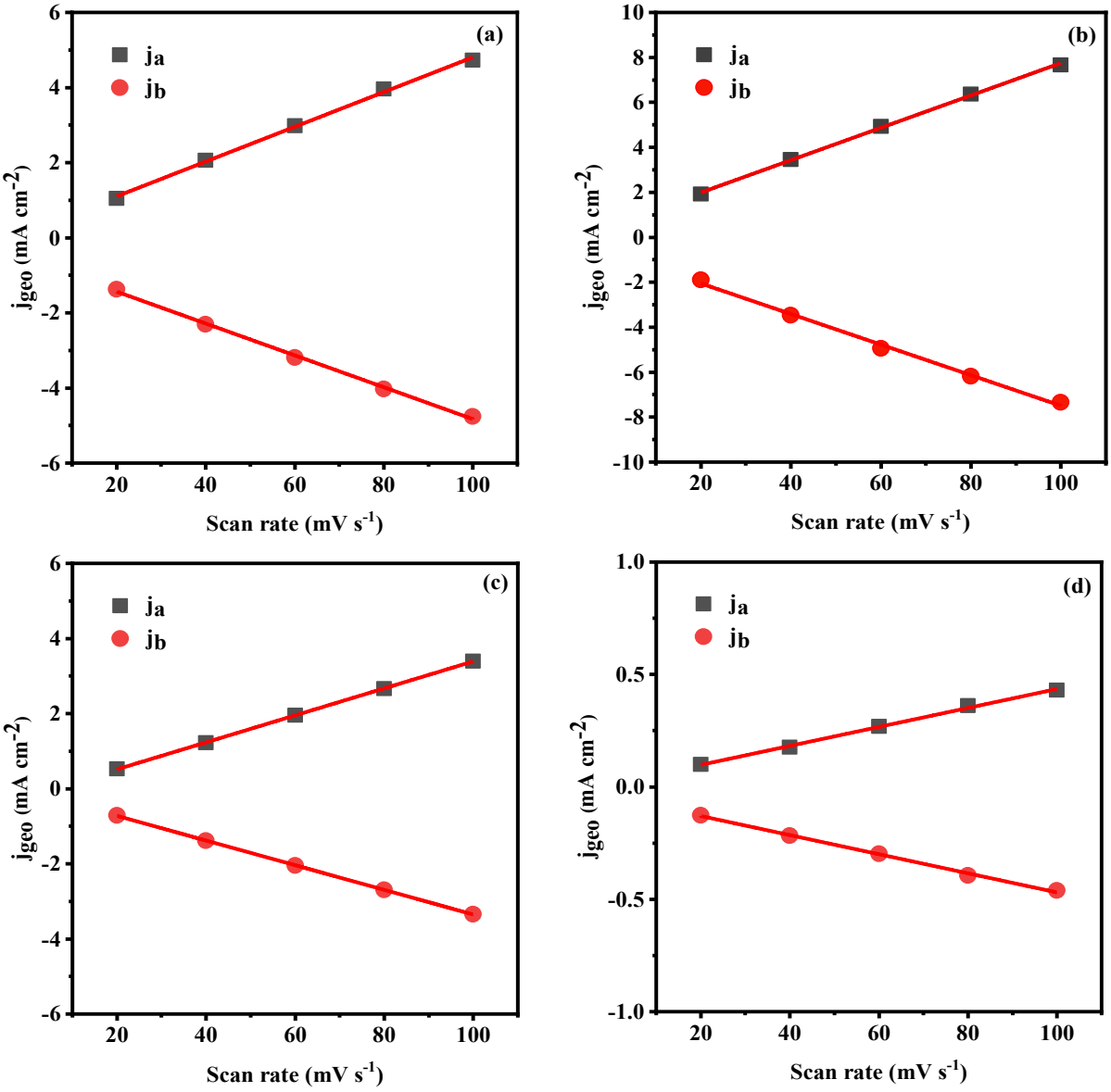


Figure 4.16: Linear fitting of the capacitive current densities for (a) HEO-R-350, (b) HEO-R-500, (c) HEO-R-700, and (d) $RuO_2$-$TiO_2$ (DSA).

Besides activity, selectivity is one of the crucial and essential parameters in CER. Under controlled reaction conditions, if the electrode has high catalytic activity but poor selectivity, then electrode can be considered as not suitable for industrial-scale electrolysis. In CER, the selectivity of $Cl^-$ ions are affected by the parasitic OER, because of its similar operating potential window

and the presence of favorable reactants ($OH^-$). The electrode's affinity for oxygen evolution reaction has been analyzed in 0.5 M $H_2SO_4$ at pH=0.3 and pH=2 conditions using LSV and short-term chronopotentiometry tests (**Figure 4.17)**. Comparing the potentials measured during LSV test in 0.5 M $H_2SO_4$ for OER and 5 M NaCl for CER , it can be observed that the electrodes were only minimally active toward OER intermediates. The HEO-R-350, HEO-R-500 and HEO-R-700 had an early onset potential for chlorine evolution in 5 M NaCl pH=2 at 1.39 V, 1.36 V and 1.37 V vs RHE and a higher potential for OER in 0.5 M $H_2SO_4$ (pH=0.3 / pH=2) at 1.4 V / 1.45 V, 1.37 V / 1.43 V, and 1.4 V / 1.44 V vs RHE. As there is always contribution from the background capacitive current, a fair comparison cannot be made from the transient techniques. Therefore, short-term chronopotentiometry tests were performed at 50 mA $cm^{-2}$ for CER and 10 mA $cm^{-2}$ for OER. Even at 50 mA $cm^{-2}$, the HEO-R electrodes had an early onset potential for CER, comparing to the higher potential required for OER even at a low current density of 10 mA $cm^{-2}$.

The potential difference between the CER in 5 M NaCl (pH=2) and OER in 0.5 M $H_2SO_4$ (pH=2) electrolyte is >50 mV for all the electrodes. This is because of the presence of Sn in the mixture, that not only acts as a valve metal increasing the stability of an electrocatalyst, but also increases the overpotential of OER by weakening the chemical absorption of $OH^*$ on the (110) plane[140]. Further, doping of rutile $TiO_2$ with transition metals such as Ru, V, and Co could have modulated the binding energy to favor optimal selectivity for chlorine evolution reaction[68]. These results indicate that the HEO-R has high selectivity towards chlorine evolution reaction in saturated chloride solutions.

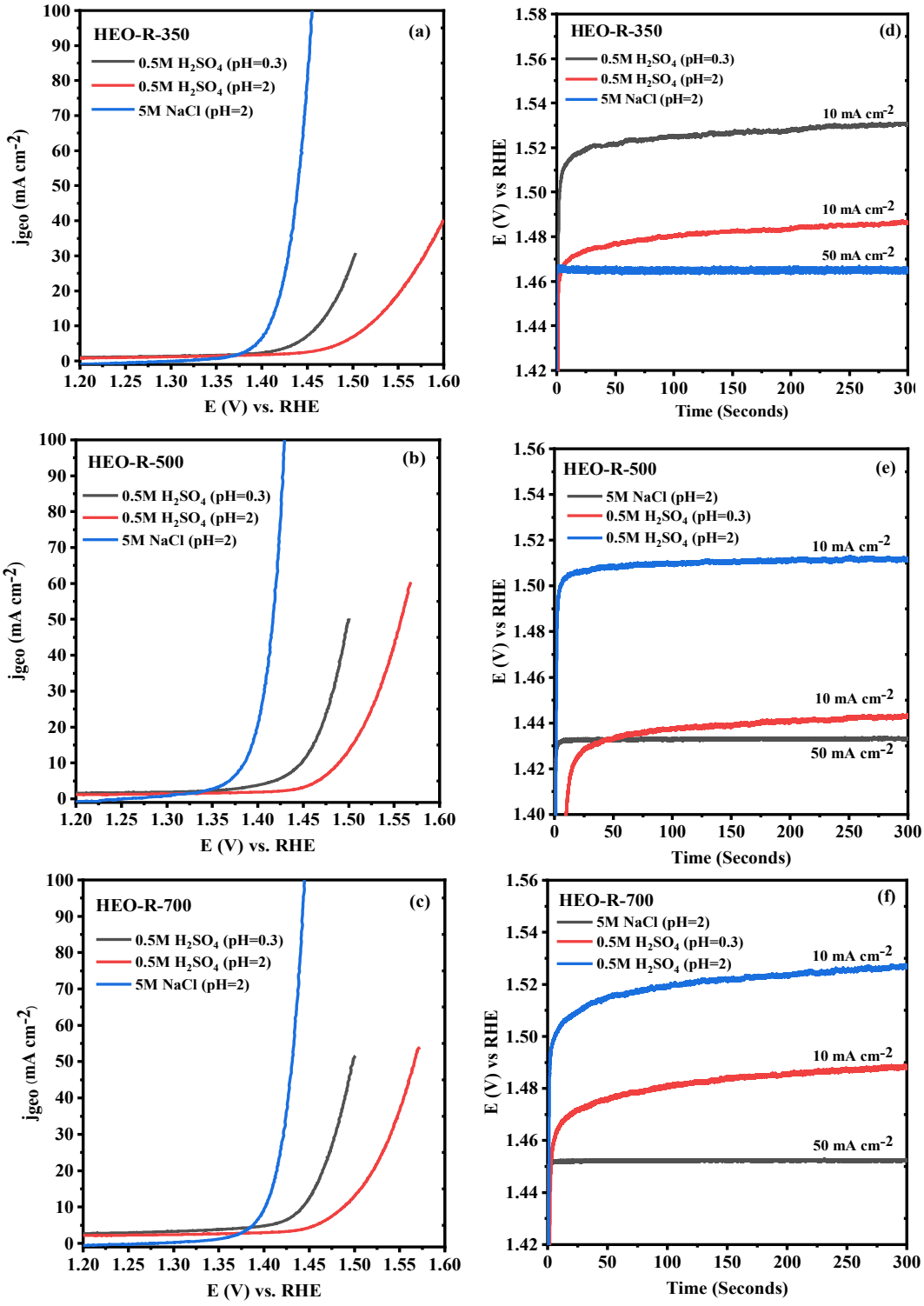


Figure 4.17: Comparison of LSV and SCV profiles for (a and d) HEO-R-350, (b and e) HEO-R-500, and (c and f) HEO-R-700.

Almost all the reported catalysts exhibit high selectivity and stability for CER, regardless of their energy consumption in saturated NaCl solutions but they deliver poor performance in the dilute chloride solutions. It is because, the low concentration of the chloride ions in the dilute solutions exhibits diffusion limitations of reactants towards the electrode surface and the high pH shifts the selectivity towards OER. The high pH not only reduces the efficiency of the electrolysis process, but also compromises the stability of the catalyst through corrosion, causing the dissolution of the metal species. For example, oxidation of $RuO_2$ ($Ru^{4+}$) to volatile $RuO_4$ ($Ru^{8+}$)[12, 25]. Hence, the electrochemical performance of the catalysts was evaluated in a dilute 0.5 M NaCl solutions at pH=6.

**Figure 4.18** compares the activity of the HEO-R and DSA electrodes measured in 0.5 M NaCl solution, and in order to maintain a constant pH at 6, 0.01 M bicarbonate salt has been added as a buffer. Among the tested electrodes, the HEO-R-500 reached 10 mA $cm^{-2}$ at 1.614 V, whereas higher potential was needed for HEO-R-350 (1.649 V), HEO-R-700 (1.655 V), and $RuO_2$-$TiO_2$ (DSA) (1.70 V). However, when the current density approached 50 mA $cm^{-2}$, the potential required was nearly similar for HEO-R-500 (1.705 V) and HEO-R-700 (1.710 V). Eventhough the DSA needed higher potential (1.70 V) in the low current density region compared to the HEO-R electrodes, the kinetics of the DSA increased comparable to the HEO-R-350 at the high current density region (50 mA $cm^{-2}$). As the potential difference at 50 mA $cm^{-2}$ between the HEO-R-500 and HEO-R-700 is very small based on the LSV curves, steady state chronopotentiometry tests were performed at 50 mA $cm^{-2}$ for one hour to monitor the potential and stability among the catalysts.

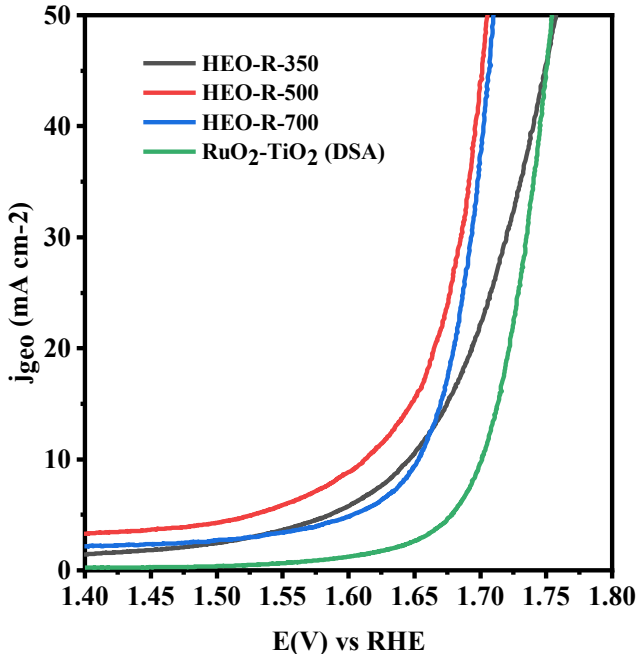


Figure 4.18: Comparison of LSV graphs of HEO-R-350, HEO-R-500, HEO-R-700, and $RuO_2$-$TiO_2$ (DSA) in 0.5 M NaCl solution.

**Figure 4.19** compares the V-t (voltage-time) curves of the synthesized catalysts obtained from the one-hour chronopotentiometry tests at 50 mA $cm^{-2}$. **Table 4.6** compares the increase in potential value from the initial stage ($100^{th}$ second) to the end of the reaction ($3600^{th}$ second). The potential value of HEO-R-500 only increased by ~0.6 % at the end of the reaction and it is because of the decrease in the chloride concentration. On the other hand, a constant increase in potential value was observed for the HEO-R-350 and HEO-R-700, with a potential increase of 2.66 % and 2.5 % at the end of the reaction. The instability of the HEO-R-350 is because of the presence of an organic-inorganic phase, that resulted in corrosion. On the other hand, the absence of a single phase and the impure nature of HEO-R-700, resulted in poor stability. Even though the DSA required higher potential for delivering 50 mA $cm^{-2}$ than the synthesized catalysts, it only had 1.73% increase in potential at the end of the test, which is lower compared to the HEO-R-350 and HEO-R-700. This is because of the existence of solid-solution of $RuO_2$-$TiO_2$ in the DSA, but their

potential increase is still higher than that of the HEO-R-500. Because of the presence of multi-metal solid solution and enhanced active sites, the HEO-R-500 is capable of catalyzing chloride ions in competitive oxidative environments with high stability.

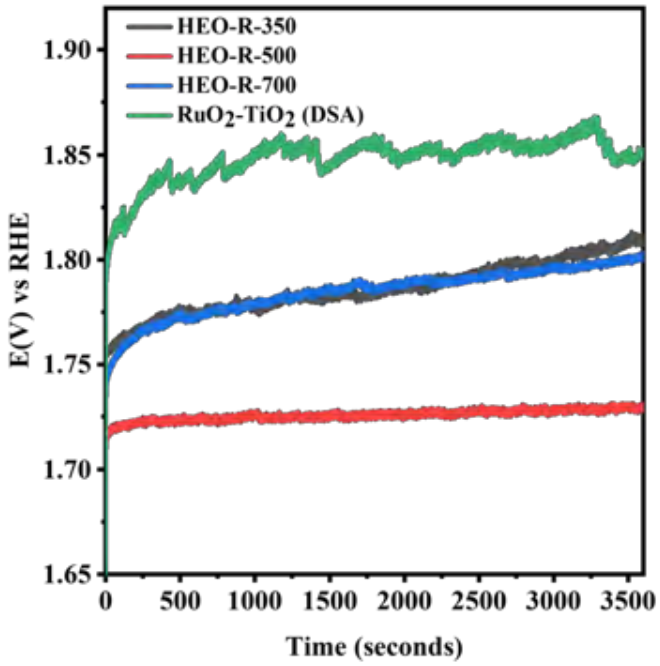


Figure 4.19: Short-term chronopotentiometry test performed for one hour in dilute 0.5 M NaCl solution (pH=6).

Table 4.6: Comparison of overpotential from short-term chronopotentiometry tests performed for one hour in dilute 0.5 M NaCl solution (pH=6).

| **Electrode** | **E(V) at 100 seconds** | **E(V) at 3600 seconds** | **Percentage of increase (%)** |
|---|---|---|---|
| HEO-R-350 | 1.762 | 1.809 | 2.66 |
| HEO-R-500 | 1.719 | 1.729 | 0.6 |
| HEO-R-700 | 1.756 | 1.801 | 2.5 |
| $RuO_2$-$TiO_2$ (DSA) | 1.817 | 1.849 | 1.73 |

Further, the faradaic efficiency (FE) of the HEO-R-500 was compared with the commercial $RuO_2$-$TiO_2$ anodes in dilute 0.5 M NaCl (pH=6 and pH=8), by quantifying the chlorine produced through chronopotentiometry test at 50 mA $cm^{-2}$ for 180 seconds (**Figure 4.20**). The DPD (N,N-diethyl-p-phenylenediamine) colorimetric test confirmed the active chlorine produced on the surface of HEO-R-500, with a high FE of 96.0 % and 94.61 % in 0.5 M NaCl solution at pH=6 and 8. The DSA also had a high FE of 93.11 % at pH=6, but when the pH of the electrolyte was increased to 8, the selectivity decreased to 73.98 %. The low FE of the DSA at pH=8 could be attributed to the OER. The high FE of the HEO-R-500 at pH=6 and pH=8, further confirms their weaker adsorption energy towards OER intermediates and optimal binding energy towards chloride ions exhibiting high selectivity. This poor selectivity towards OER will also improve the stability of the catalysts, by preventing corrosion through metal dissolution[1, 11].

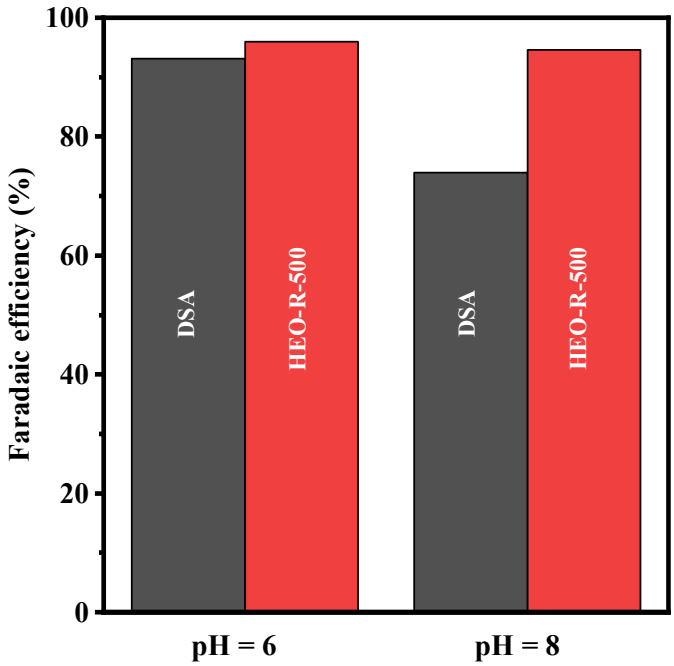


Figure 4.20: Faradaic efficiency test performed for one hour at 50 mA $cm^{-2}$ in dilute 0.5 M NaCl solution (pH=6 and 8).

The long-term stability of the HEO-R-500 was analyzed in a 5 M NaCl solution (pH=2) by performing chronopotentiometry test at $j_{geo}$ = 50 mA $cm^{-2}$ for 100 hours. The electrolyte was kept under circulation using a peristaltic pump and was replaced every 24 hours. **Figure 4.21 (a)** shows that, only a potential increase of 0.9% (13 mV) from 1.428 V vs RHE to 1.441 V vs RHE was observed, confirming the stability of the electrode. The total energy consumed during the test was 0.359 Wh or 7.17 Wh $cm^{-2}$. In addition, the LSV curves (**Figure 4.21 b**) recorded before and after the 100-hours chronopotentiometry test shows that, the electrode retained its initial activity with only a negligible shift in overpotential, indicating the excellent durability of the electrode. On the whole, the HEO-R-500 exhibits enhanced catalytic activity, selectivity, and outstanding stability towards CER in both saturated and diluted NaCl solutions, that is attributed to the combined effect of the multi-metal interactions (Ru, Ti, Sn, V, and Co), enhanced electrical conductivity and structural stability of the HEO-R.

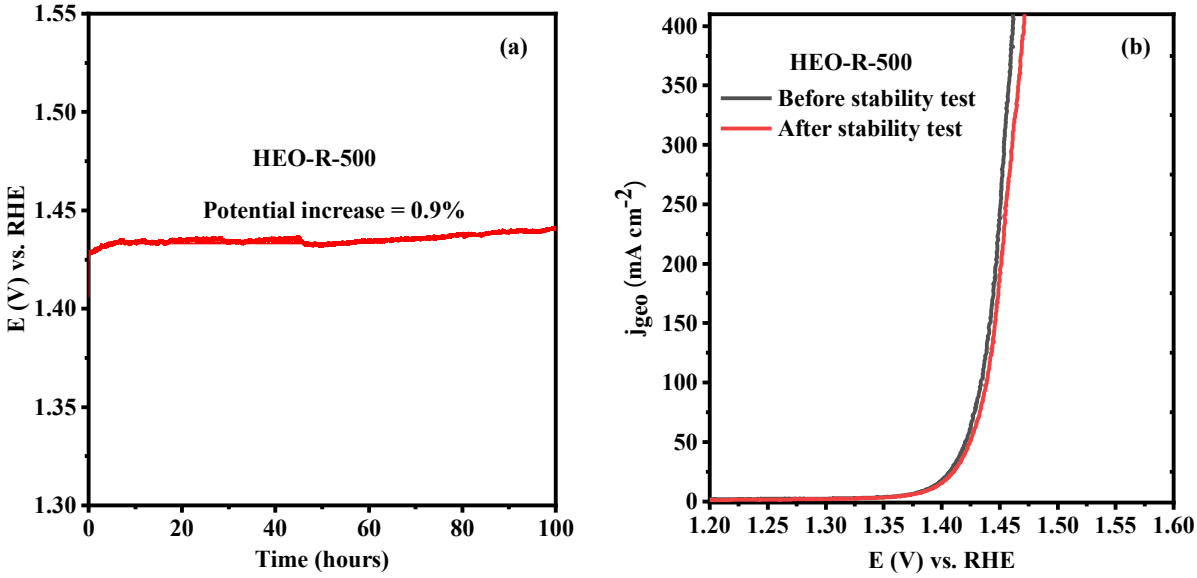


Figure 4.21: (a) Chronopotentiometry test of HEO-R-500 at $j_{geo}$ = 50 mA $cm^{-2}$ in 5.0 M NaCl solution (pH=2) electrolyte for 100 hours; (b) LSV test of HEO-R-500 before and after the 100-hour chronopotentiometry test at $j_{geo}$ = 50 mA $cm^{-2}$ in 5.0 M NaCl solution (pH=2).

# Chapter 5. Conclusion

## 5.1 Contributions to knowledge

The present study comprises the synthesis, analytical characterizations, and electrochemical investigation of rutile structured high entropy oxides as a potential catalyst for chlorine evolution reaction. The following contributions to knowledge are made:

- An effective CER catalyst, HEO-R-500 have been successfully synthesized through solvothermal method at 500 °C. As synthesized HEO-R-500 contains five distributed metal elements (Ru, Ti, Sn, V, and Co) exhibiting a single phase rutile structure and nanoparticle size (10 - 15 nm).
- When used in CER electrolysis, the HEO-R-500 exhibited a high catalytic activity with small overpotential of 1.387 V, 1.417 V, and 1.429 V at 10, 50 and 100 mA $cm^{-2}$ in the saturated 5 M NaCl (pH=2) solution. The electrode resulted in an efficient electron transfer as a result of small charge transfer resistance and increased active sites. The electrocatalytic performance of HEO-R-500 is superior to the synthesized HEO-R-350, HEO-R-700 and commercial $RuO_2$-$TiO_2$ (DSA). As for the stability of HEO-R-500, after a 100 hour chronopotentiometry test at 50 mA $cm^{-2}$ in 5 M NaCl (pH=2) solution, a negligible increase in potential (0.9%) and complete initial activity retention have been observed. In dilute electrolyte (0.5M NaCl) conditions, the HEO-R-500 exhibited a better stability and higher faradaic efficiency (96.0 % and 94.61% at pH 6 and 8) than the commercial $RuO_2$-$TiO_2$ (DSA). This excellent electrocatalytic activity could be attributed to the combined effect of the metals present in the HEO-R-500.

- This work demonstrates that the HEOs are potential catalysts for chlorine electrolysis. They can offer high catalytic activity and durability with small energy consumption.

## 5.2 Suggestions for future study

The following studies may be performed in the future to further evaluate and improve the electrocatalytic activity of the synthesized catalysts.

1. Post analytical characterizations, such as XRD and XPS analysis, will be performed to analyze the changes in elemental concentration and surface oxidation state of the anode materials after the stability tests.
2. Single phase high entropy oxides can be obtained by controlling the hydrothermal and sintering temperature. The influence of the uniform oxidation state of elements in obtaining equimolar composition and single phase could be investigated. The influence of particle size and elemental composition of the HEO on the electrocatalytic activity of CER could be studied.
3. The Ru element present in the HEO-R-500 can be replaced with other active elements for chlorine evolution, such as Ir, Pb, & Mn. The difference in activity, stability and selectivity compared to Ru can be studied.

# References


1. Karlsson, R.K.B., and A. Cornell, Selectivity Between Oxygen and Chlorine Evolution in the Chlor-Alkali and Chlorate Processes. *Chemical Reviews*. **116**(5), 2982-3028, (2016).
2. Thummar, K., R. Abang, K. Menzel, and M.T. de Groot, Coupling a Chlor-Alkali Membrane Electrolyzer Cell to a Wind Energy Source: Dynamic Modeling and Simulations. *Energies*. **15**(2), 606, (2022).
3. Wang, Y.T., Y.D. Xue, and C.H. Zhang, Rational Surface and Interfacial Engineering of $IrO_2/TiO_2$ Nanosheet Arrays Toward High-Performance Chlorine Evolution Electrocatalysis and Practical Environmental Remediation. *Small*. **17**(17), (2021).
4. Huber, M.M., S. Korhonen, T.A. Ternes, and U. von Gunten, Oxidation of Pharmaceuticals During Water Treatment with Chlorine Dioxide. *Water Research*. **39**(15), 3607-3617, (2005).
5. Hey, G., R. Grabic, A. Ledin, J. la Cour Jansen, and H.R. Andersen, Oxidation of Pharmaceuticals by Chlorine Dioxide in Biologically Treated Wastewater. *Chemical Engineering Journal*. **185-186**236-242, (2012).
6. Fang, W.-Y., L. Ravindar, K.P. Rakesh, H.M. Manukumar, C.S. Shantharam, N.S. Alharbi, and H.-L. Qin, Synthetic Approaches and Pharmaceutical Applications of Chloro-Containing Molecules for Drug Discovery: A Critical Review. *European Journal of Medicinal Chemistry*. **173**117-153, (2019).
7. *Benefits of Chlor-Alkali Chemistry*. 03:00 pm (HKT), 22/12/2022; Available from: https://worldchlorine.org/chlorine-chemistry-benefits/healthcare/.

8. Bedner, M., W.A. MacCrehan, and G.R. Helz, Production of Macromolecular Chloramines by Chlorine-Transfer Reactions. *Environmental Science & Technology*. **38**(6), 1753-1758, (2004).

9. Joshi, K., R. Mahendran, K. Alagusundaram, T. Norton, and B.K. Tiwari, Novel Disinfectants for Fresh Produce. *Trends in Food Science & Technology*. **34**(1), 54-61, (2013).

10. Wang, Y., Y. Liu, D. Wiley, S. Zhao, and Z. Tang, Recent Advances in Electrocatalytic Chloride Oxidation for Chlorine Gas Production. *Journal of Materials Chemistry A*. **9**(35), 18974-18993, (2021).

11. Dong, H., W. Yu, and M.R. Hoffmann, Mixed Metal Oxide Electrodes and the Chlorine Evolution Reaction. *The Journal of Physical Chemistry C*. **125**(38), 20745-20761, (2021).

12. O'Brien Thomas, B.V.T., Hine Fumio, Handbook of Chlor-Alkali Technology. Volume 1, Volume 1. (2005).

13. Gendel, Y., G. Amikam, and P. Nativ, *Chapter 9 - Seawater Electrolysis*, in *Electrochemical Power Sources: Fundamentals, Systems, and Applications*, T. Smolinka and J. Garche, Editors. 2022, Elsevier. p. 305-326.

14. Chen, S., Y. Zheng, S. Wang, and X. Chen, Ti/$RuO_2$–$Sb_2O_5$–$SnO_2$ Electrodes for Chlorine Evolution from Seawater. *Chemical Engineering Journal*. **172**(1), 47-51, (2011).

15. Jeong, H.J., H.R. Kim, K.I. Kim, K.Y. Kim, K.H. Park, S.T. Kim, Y.D. Yoo, J.Y. Song, J.S. Kim, K.A. Seong, W.H. Yih, S.J. Pae, C.H. Lee, M.D. Huh, and S.H. Lee, NaOCl Produced by Electrolysis of Natural Seawater as a Potential Method to Control Marine Red-Tide Dinoflagellates. *Phycologia*. **41**(6), 643-656, (2002).

16. Huskinson, B., J. Rugolo, S.K. Mondal, and M.J. Aziz, A High Power Density, High Efficiency Hydrogen–Chlorine Regenerative Fuel Cell with a Low Precious Metal Content Catalyst. *Energy & Environmental Science*. **5**(9), 8690-8698, (2012).

17. Jameson, A., and E. Gyenge, Halogens as Positive Electrode Active Species for Flow Batteries and Regenerative Fuel Cells. *Electrochemical Energy Reviews*. **3**(3), 431-465, (2020).

18. Sun, Y., and S. Dai, High-Entropy Materials for Catalysis: A New Frontier. *Science Advances*. **7**(20), eabg1600, (2021).

19. Albedwawi, S.H., A. AlJaberi, G.N. Haidemenopoulos, and K. Polychronopoulou, High entropy oxides-exploring a paradigm of promising catalysts: A review. *Materials & Design*. **202**109534, (2021).

20. Miao, X., Z. Peng, L. Shi, and S. Zhou, Insulating High-Entropy Ruthenium Oxide as a Highly Efficient Oxygen-Evolving Electrocatalyst in Acid. *ACS Catalysis*. **13**(6), 3983-3989, (2023).

21. Gao, Y., Y. Liu, H. Yu, and D. Zou, High-entropy oxides for catalysis: Status and perspectives. *Applied Catalysis A: General*. **631**118478, (2022).

22. Oses, C., C. Toher, and S. Curtarolo, High-entropy ceramics. *Nature Reviews Materials*. **5**(4), 295-309, (2020).

23. Zeradjanin, A.R., N. Menzel, W. Schuhmann, and P. Strasser, On the Faradaic Selectivity and the Role of Surface Inhomogeneity During the Chlorine Evolution Reaction on Ternary Ti–Ru–Ir Mixed Metal Oxide Electrocatalysts. *Physical Chemistry Chemical Physics*. **16**(27), 13741-13747, (2014).

24. Sealey, S., *Modern Chlor-Alkali Technology*. Vol. 7. 1998: Royal Society of Chemistry.

25. Lim, H.W., D.K. Cho, J.H. Park, S.G. Ji, Y.J. Ahn, J.Y. Kim, and C.W. Lee, Rational Design of Dimensionally Stable Anodes for Active Chlorine Generation. *ACS Catalysis*. **11**(20), 12423-12432, (2021).

26. Lim, T., G.Y. Jung, J.H. Kim, S.O. Park, J. Park, Y.-T. Kim, S.J. Kang, H.Y. Jeong, S.K. Kwak, and S.H. Joo, Atomically Dispersed Pt–$N_4$ Sites as Efficient and Selective Electrocatalysts for the Chlorine Evolution Reaction. *Nature Communications*. **11**(1), 412, (2020).

27. Trasatti, S., Progress in the Understanding of the Mechanism of Chlorine Evolution at Oxide Electrodes. *Electrochimica Acta*. **32**(3), 369-382, (1987).

28. Faita, G., and G. Fiori, Anodic Discharge of Chloride Ions on Oxide Electrodes. *Journal of Applied Electrochemistry*. **2**(1), 31-35, (1972).

29. Janssen, L.J.J., L.M.C. Starmans, J.G. Visser, and E. Barendrecht, Mechanism of the Chlorine Evolution on a Ruthenium Oxide/Titanium Oxide Electrode and on a Ruthenium Electrode. *Electrochimica Acta*. **22**(10), 1093-1100, (1977).

30. Krishtalik, L.I., Kinetics and Mechanism of Anodic Chlorine and Oxygen Evolution Reactions on Transition Metal Oxide Electrodes. *Electrochimica Acta*. **26**(3), 329-337, (1981).

31. Suen, N.-T., S.-F. Hung, Q. Quan, N. Zhang, Y.-J. Xu, and H.M. Chen, Electrocatalysis for the Oxygen Evolution Reaction: Recent Development and Future Perspectives. *Chemical Society Reviews*. **46**(2), 337-365, (2017).

32. Fabbri, E., and T.J. Schmidt, Oxygen Evolution Reaction—The Enigma in Water Electrolysis. *ACS Catalysis*. **8**(10), 9765-9774, (2018).

33. Guerrini, E., V. Consonni, and S. Trasatti, Surface and Electrocatalytic Properties of Well-Defined and Vicinal $RuO_2$ Single Crystal Faces. *Journal of Solid State Electrochemistry*. **9**(5), 320-329, (2005).

34. Exner, K.S., Controlling Stability and Selectivity in the Competing Chlorine and Oxygen Evolution Reaction Over Transition Metal Oxide Electrodes. *ChemElectroChem*. **6**(13), 3401-3409, (2019).

35. Anantharaj, S., S.R. Ede, K. Karthick, S. Sam Sankar, K. Sangeetha, P.E. Karthik, and S. Kundu, Precision and Correctness in the Evaluation of Electrocatalytic Water Splitting: Revisiting Activity Parameters With a Critical Assessment. *Energy & Environmental Science*. **11**(4), 744-771, (2018).

36. Anantharaj, S., and S. Noda, Dos and Don'ts in Screening Water Splitting Electrocatalysts. *Energy Advances*(2022).

37. Anantharaj, S., S. Kundu, and S. Noda, Worrisome Exaggeration of Activity of Electrocatalysts Destined for Steady-State Water Electrolysis by Polarization Curves from Transient Techniques. *Journal of The Electrochemical Society*. **169**(1), 014508, (2022).

38. Anantharaj, S., S. Noda, M. Driess, and P.W. Menezes, The Pitfalls of Using Potentiodynamic Polarization Curves for Tafel Analysis in Electrocatalytic Water Splitting. *ACS Energy Letters*. **6**(4), 1607-1611, (2021).

39. Anantharaj, S., H. Sugime, and S. Noda, Why Shouldn't Double-Layer Capacitance (Cdl) be Always Trusted to Justify Faradaic Electrocatalytic Activity Differences? *Journal of Electroanalytical Chemistry*. **903**115842, (2021).

40. Anantharaj, S., and S. Kundu, Do the Evaluation Parameters Reflect Intrinsic Activity of Electrocatalysts in Electrochemical Water Splitting? *ACS Energy Letters*. **4**(6), 1260-1264, (2019).

41. Duby, P., The History of Progress in Dimensionally Stable Anodes. *JOM*. **45**(3), 41-43, (1993).

42. Trasatti, S., Electrocatalysis: Understanding the Success of DSA®. *Electrochimica Acta*. **45**(15), 2377-2385, (2000).

43. Beer, H.B., *Dimensionally Stable Anodes*, in *Electrochemistry In Industry: New Directions*, U. Landau, E. Yeager, and D. Kortan, Editors. 1982, Springer US: Boston, MA. p. 19-28.

44. Beer, H.B., The Invention and Industrial Development of Metal Anodes. *Journal of The Electrochemical Society*. **127**(8), 303C-307C, (1980).

45. Su, J., R. Ge, Y. Dong, F. Hao, and L. Chen, Recent Progress in Single-Atom Electrocatalysts: Concept, Synthesis, and Applications in Clean Energy Conversion. *Journal of Materials Chemistry A*. **6**(29), 14025-14042, (2018).

46. Chen, X., and G. Chen, Stable Ti/$RuO_2$–$Sb_2O_5$–$SnO_2$ Electrodes for $O_2$ Evolution. *Electrochimica Acta*. **50**(20), 4155-4159, (2005).

47. Hu, J., H. Xu, X. Feng, L. Lei, Y. He, and X. Zhang, Neodymium-Doped $IrO_2$ Electrocatalysts Supported on Titanium Plates for Enhanced Chlorine Evolution Reaction Performance. *ChemElectroChem*. **8**(6), 1204-1210, (2021).

48. Ha, H., K. Jin, S. Park, K.-G. Lee, K.H. Cho, H. Seo, H.-Y. Ahn, Y.H. Lee, and K.T. Nam, Highly Selective Active Chlorine Generation Electrocatalyzed by Co3O4 Nanoparticles: Mechanistic Investigation Through in Situ Electrokinetic and Spectroscopic Analyses. *The Journal of Physical Chemistry Letters*. **10**(6), 1226-1233, (2019).

49. Moreno-Hernandez, I.A., B.S. Brunschwig, and N.S. Lewis, Crystalline Nickel, Cobalt, and Manganese Antimonates as Electrocatalysts for the Chlorine Evolution Reaction. *Energy & Environmental Science*. **12**(4), 1241-1248, (2019).

50. Vos, J.G., Z. Liu, F.D. Speck, N. Perini, W. Fu, S. Cherevko, and M.T.M. Koper, Selectivity Trends Between Oxygen Evolution and Chlorine Evolution on Iridium-Based Double Perovskites in Acidic Media. *ACS Catalysis*. **9**(9), 8561-8574, (2019).

51. Ooka, H., J. Huang, and K.S. Exner, The Sabatier Principle in Electrocatalysis: Basics, Limitations, and Extensions. *Frontiers in Energy Research*. **9**(2021).

52. Laursen, A.B., A.S. Varela, F. Dionigi, H. Fanchiu, C. Miller, O.L. Trinhammer, J. Rossmeisl, and S. Dahl, Electrochemical Hydrogen Evolution: Sabatier's Principle and the Volcano Plot. *Journal of Chemical Education*. **89**(12), 1595-1599, (2012).

53. Hansen, H.A., I.C. Man, F. Studt, F. Abild-Pedersen, T. Bligaard, and J. Rossmeisl, Electrochemical Chlorine Evolution at Rutile Oxide (110) Surfaces. *Physical Chemistry Chemical Physics*. **12**(1), 283-290, (2010).

54. Zeradjanin, A.R., N. Menzel, P. Strasser, and W. Schuhmann, Role of Water in the Chlorine Evolution Reaction at $RuO_2$-Based Electrodes-Understanding Electrocatalysis as a Resonance Phenomenon. *Chemsuschem*. **5**(10), 1897-1904, (2012).

55. Wang, S.W., H.L. Xu, P.D. Yao, and X.M. Chen, Ti/$RuO_2$-$IrO_2$-$SnO_2$-$Sb_2O_5$ Anodes for $Cl_2$ Evolution from Seawater. *Electrochemistry*. **80**(7), 507-511, (2012).

56. Exner, K.S., Beyond the Traditional Volcano Concept: Overpotential-Dependent Volcano Plots Exemplified by the Chlorine Evolution Reaction over Transition-Metal Oxides. *The Journal of Physical Chemistry C*. **123**(27), 16921-16928, (2019).

57. Exner, K.S., J. Anton, T. Jacob, and H. Over, Full Kinetics from First Principles of the Chlorine Evolution Reaction over a $RuO_2$(110) Model Electrode. *Angewandte Chemie International Edition*. **55**(26), 7501-7504, (2016).

58. Le Luu, T., J. Kim, and J. Yoon, Physicochemical Properties of $RuO_2$ and $IrO_2$ Electrodes Affecting Chlorine Evolutions. *Journal of Industrial and Engineering Chemistry*. **21**400-404, (2015).

59. Han, S., S. Kim, S. Kwak, C. Lee, D. Hong Jeong, C. Kim, and J. Yoon, Iridium-Cobalt Mixed Oxide Electrode for Efficient Chlorine Evolution in Dilute Chloride Solutions. *Journal of Industrial and Engineering Chemistry*. **108**514-521, (2022).

60. Li, J., X. Qin, G. Chen, and G. Chen, The Effect of Ruthenium Content on the Stability And Activity of Ti/$RuO_2$-$Sb_2O_5$-$SnO_2$ for Oxygen Evolution. *Journal of the Taiwan Institute of Chemical Engineers*. **125**186-194, (2021).

61. Arikawa, T., Y. Murakami, and Y. Takasu, Simultaneous Determination of Chlorine and Oxygen Evolving at $RuO_2$/Ti and $RuO_2$–$TiO_2$/Ti Anodes by Differential Electrochemical Mass Spectroscopy. *Journal of Applied Electrochemistry*. **28**(5), 511-516, (1998).

62. Macounová, K.M., R. Pittkowski, R. Nebel, A. Zitolo, and P. Krtil, Selectivity of Ru-Rich Ru-Ti-O Oxide Surfaces in Parallel Oxygen and Chlorine Evolution Reactions. *Electrochimica Acta*140878, (2022).

63. Takasu, Y., T. Arikawa, S. Sunohara, and K. Yahikozawa, Direct Detection of Competitively Evolving Chlorine and Oxygen at Anodes. *Journal of Electroanalytical Chemistry*. **361**(1), 279-281, (1993).

64. Kokoulina, D.V., and L.V. Bunakova, Oxygen Evolution at the Oxide Electrodes $RuO_2$ and $RuO_2$+$TiO_2$ in Chloride Solutions. *Journal Of Electroanalytical Chemistry And Interfacial Electrochemistry*. **164**(2), 377-383, (1984).

65. Bune, N.Y., V.V. Losev, M.F. Reznik, and E.N. Zaripova, Selectivity and Electrochemical Behavior of Titanium-Ruthenium Oxide Anodes Containing Different Levels of Ruthenium Dioxide. *Soviet Electrochemistry*. **22**(3), 365-368, (1986).

66. Gajić-Krstajić, L.M., T.L. Trišović, and N.V. Krstajić, Spectrophotometric Study of the Anodic Corrosion of Ti/$RuO_2$ Electrode in Acid Sulfate Solution. *Corrosion Science*. **46**(1), 65-74, (2004).

67. Zeradjanin, A.R., A.A. Topalov, Q. Van Overmeere, S. Cherevko, X. Chen, E. Ventosa, W. Schuhmann, and K.J.J. Mayrhofer, Rational Design of the Electrode Morphology for Oxygen Evolution – Enhancing the Performance for Catalytic Water Oxidation. *RSC Advances*. **4**(19), 9579-9587, (2014).

68. Karlsson, R.K.B., A. Cornell, and L.G.M. Pettersson, The Electrocatalytic Properties of Doped $TiO_2$. *Electrochimica Acta*. **180**514-527, (2015).

69. Karlsson, R.K.B., H.A. Hansen, T. Bligaard, A. Cornell, and L.G.M. Pettersson, Ti Atoms in $Ru_{0.3}Ti_{0.7}O_2$ Mixed Oxides Form Active and Selective Sites for Electrochemical Chlorine Evolution. *Electrochimica Acta*. **146**733-740, (2014).

70. Cheng, W., Y. Liu, L. Wu, R. Chen, J. Wang, S. Chang, F. Ma, Y. Li, and H. Ni, $RuO_2$/$IrO_2$ Nanoparticles Decorated $TiO_2$ Nanotube Arrays for Improved Activity Towards Chlorine Evolution Reaction. *Catalysis Today*. **400-401**26-34, (2022).

71. Xiong, K., Z.H. Deng, L. Li, S.G. Chen, M.R. Xia, L. Zhang, X.Q. Qi, W. Ding, S.Y. Tan, and Z.D. Wei, Sn And Sb Co-Doped Ruti Oxides Supported on $TiO_2$ Nanotubes

Anode for Selectivity Toward Electrocatalytic Chlorine Evolution. *Journal of Applied Electrochemistry*. **43**(8), 847-854, (2013).

72. Huang, J., M. Hou, J. Wang, X. Teng, Y. Niu, M. Xu, and Z. Chen, $RuO_2$ Nanoparticles Decorate Belt-Like Anatase $TiO_2$ for Highly Efficient Chlorine Evolution. *Electrochimica Acta*. **339**135878, (2020).

73. Näslund, L.-Å., C.M. Sánchez-Sánchez, Á.S. Ingason, J. Bäckström, E. Herrero, J. Rosen, and S. Holmin, The Role of $TiO_2$ Doping on $RuO_2$-Coated Electrodes for the Water Oxidation Reaction. *The Journal of Physical Chemistry C*. **117**(12), 6126-6135, (2013).

74. Exner, K.S., J. Anton, T. Jacob, and H. Over, Controlling Selectivity in the Chlorine Evolution Reaction over $RuO_2$-Based Catalysts. *Angewandte Chemie-International Edition*. **53**(41), 11032-11035, (2014).

75. Finke, C.E., S.T. Omelchenko, J.T. Jasper, M.F. Lichterman, C.G. Read, N.S. Lewis, and M.R. Hoffmann, Enhancing the Activity of Oxygen-Evolution and Chlorine-Evolution Electrocatalysts by Atomic Layer Deposition of $TiO_2$. *Energy & Environmental Science*. **12**(1), 358-365, (2019).

76. Deng, L., Y. Liu, G. Zhao, J. Chen, S. He, Y. Zhu, B. Chai, and Z. Ren, Preparation of Electrolyzed Oxidizing Water By $TiO_2$ Doped $IrO_2$-$Ta_2O_5$ Electrode With High Selectivity And Stability For Chlorine Evolution. *Journal of Electroanalytical Chemistry*. **832**459-466, (2019).

77. Tilak, B.V., V.I. Birss, J. Wang, C.P. Chen, and S.K. Rangarajan, Deactivation of Thermally Formed Ru/Ti Oxide Electrodes - an AC Impedance Characterization Study. *Journal of the Electrochemical Society*. **148**(9), D112-D120, (2001).

78. Onuchukwu, A.I., and S. Trasatti, Effect of Substitution of $SnO_2$ for $TiO_2$ on the Surface and Electrocatalytic Properties of $RuO_2$+$TiO_2$ Electrodes. *Journal of Applied Electrochemistry*. **21**(10), 858-862, (1991).

79. Chen, A., X. Zhu, J. Xi, H. Qin, and Z. Ji, Ultra-High Oxidation Potential of Ti/$CuSnO_2$ Anodes Fabricated by Spray Pyrolysis for Wastewater Treatment. *Journal of Alloys and Compounds*. **683**501-505, (2016).

80. Chiaki, I., I. Meguru, and T. Hideo, Foreign Metal-Doped $SnO_2$ Film Anodes for Oxygen and Chlorine Evolution. *Chemistry Letters*. **8**(3), 225-228, (1979).

81. Macounová, K., M. Makarova, J. Jirkovský, J. Franc, and P. Krtil, Parallel Oxygen and Chlorine Evolution on $Ru_{1-x}Ni_xO_{2-Y}$ Nanostructured Electrodes. *Electrochimica Acta*. **53**(21), 6126-6134, (2008).

82. Petrykin, V., K. Macounová, M. Okube, S. Mukerjee, and P. Krtil, Local Structure of Co Doped $RuO_2$ Nanocrystalline Electrocatalytic Materials For Chlorine and Oxygen Evolution. *Catalysis Today*. **202**63-69, (2013).

83. Shao, D., W. Yan, L. Cao, X. Li, and H. Xu, High-Performance Ti/Sb–$SnO_2$/$Pb_3O_4$ Electrodes for Chlorine Evolution: Preparation and Characteristics. *Journal of Hazardous Materials*. **267**238-244, (2014).

84. Macounová, K., J. Jirkovský, M.V. Makarova, J. Franc, and P. Krtil, Oxygen Evolution on $Ru_{1-x}Ni_xO_2$ − Ynanocrystalline Electrodes. *Journal of Solid State Electrochemistry*. **13**(6), 959-965, (2009).

85. Petrykin, V., K. Macounova, J. Franc, O. Shlyakhtin, M. Klementova, S. Mukerjee, and P. Krtil, Zn-Doped $RuO_2$ Electrocatalyts for Selective Oxygen Evolution: Relationship

Between Local Structure and Electrocatalytic Behavior in Chloride Containing Media. *Chemistry of Materials*. **23**(2), 200-207, (2011).

86. Ha, H., K. Jin, S. Park, K.G. Lee, K.H. Cho, H. Seo, H.Y. Ahn, Y.H. Lee, and K.T. Nam, Highly Selective Active Chlorine Generation Electrocatalyzed by $Co_3O_4$ Nanoparticles: Mechanistic Investigation Through in Situ Electrokinetic and Spectroscopic Analyses. *Journal of Physical Chemistry Letters*. **10**(6), 1226-1233, (2019).

87. da Silva, L.M., J.F.C. Boodts, and L.A. de Faria, Chlorine Evolution Reaction at Ti/($RuO_2$+$Co_3O_4$) Electrodes. *Journal of the Brazilian Chemical Society*. **14**(3), 388-395, (2003).

88. Mirzaei Alavijeh, M., S. Habibzadeh, K. Roohi, F. Keivanimehr, L. Naji, and M.R. Ganjali, A Selective and Efficient Precious Metal-Free Electrocatalyst for Chlorine Evolution Reaction: An Experimental and Computational Study. *Chemical Engineering Journal*. **421**127785, (2021).

89. Evans, T.A., and K.-S. Choi, Electrochemical Synthesis and Investigation of Stoichiometric, Phase-Pure $CoSb_2O_6$ and $MnSb_2O_6$ Electrodes for the Oxygen Evolution Reaction in Acidic Media. *ACS Applied Energy Materials*. **3**(6), 5563-5571, (2020).

90. Goudarzi, M., and M. Ghorbani, A Study on Ternary Mixed Oxide Coatings Containing Ti, Ru, Ir by Sol–Gel Method on Titanium. *Journal of Sol-Gel Science and Technology*. **73**(2), 332-340, (2015).

91. Chen, R., V. Trieu, A.R. Zeradjanin, H. Natter, D. Teschner, J. Kintrup, A. Bulan, W. Schuhmann, and R. Hempelmann, Microstructural Impact of Anodic Coatings on the Electrochemical Chlorine Evolution Reaction. *Physical Chemistry Chemical Physics*. **14**(20), 7392-7399, (2012).

92. Menzel, N., E. Ortel, K. Mette, R. Kraehnert, and P. Strasser, Dimensionally Stable Ru/Ir/$TiO_2$-Anodes with Tailored Mesoporosity for Efficient Electrochemical Chlorine Evolution. *ACS Catalysis*. **3**(6), 1324-1333, (2013).

93. Zhang, F., X. Gu, S. Zheng, H. Yuan, J. Li, and X. Wang, Highly Catalytic Flexible $RuO_2$ on Carbon Fiber Cloth Network for Boosting Chlorine Evolution Reaction. *Electrochimica Acta*. **307**385-392, (2019).

94. Xiong, K., L. Peng, Y. Wang, L. Liu, Z. Deng, L. Li, and Z. Wei, In Situ Growth of $RuO_2$–$TiO_2$ Catalyst With Flower-Like Morphologies on the Ti Substrate as a Binder-Free Integrated Anode for Chlorine Evolution. *Journal of Applied Electrochemistry*. **46**(8), 841-849, (2016).

95. Jiang, M., H. Wang, Y. Li, H. Zhang, G. Zhang, Z. Lu, X. Sun, and L. Jiang, Superaerophobic $RuO_2$-Based Nanostructured Electrode for High-Performance Chlorine Evolution Reaction. *Small*. **13**(4), 1602240, (2017).

96. Abid, N., A.M. Khan, S. Shujait, K. Chaudhary, M. Ikram, M. Imran, J. Haider, M. Khan, Q. Khan, and M. Maqbool, Synthesis of Nanomaterials Using Various Top-Down and Bottom-Up Approaches, Influencing Factors, Advantages, and Disadvantages: A Review. *Advances in Colloid and Interface Science*. **300**102597, (2022).

97. Liang, J., Q. Liu, T. Li, Y. Luo, S. Lu, X. Shi, F. Zhang, A.M. Asiri, and X. Sun, Magnetron Sputtering Enabled Sustainable Synthesis of Nanomaterials for Energy Electrocatalysis. *Green Chemistry*. **23**(8), 2834-2867, (2021).

98. Zhao, J., Y. Zeng, J. Wang, Q. Xu, R. Chen, H. Ni, and G.J. Cheng, Ultrahigh Electrocatalytic Activity With Trace Amounts of Platinum Loadings on Free-Standing

Mesoporous Titanium Nitride Nanotube Arrays for Hydrogen Evolution Reactions. *Nanoscale*. **12**(28), 15393-15401, (2020).

99. Heo, S.E., H.W. Lim, D.K. Cho, I.J. Park, H. Kim, C.W. Lee, S.H. Ahn, and J.Y. Kim, Anomalous Potential Dependence of Conducting Property in Black Titania Nanotube Arrays for Electrocatalytic Chlorine Evolution. *Journal of Catalysis*. **381**462-467, (2020).

100. Wang, C., B. Yan, Z. Chen, B. You, T. Liao, Q. Zhang, Y. Lu, S. Jiang, and S. He, Recent Advances in Carbon Substrate Supported Nonprecious Nanoarrays for Electrocatalytic Oxygen Evolution. *Journal of Materials Chemistry A*. **9**(46), 25773-25795, (2021).

101. Shi, H., G. Wen, Y. Nie, G. Zhang, and H. Duan, Flexible 3d Carbon Cloth as a High-Performing Electrode for Energy Storage and Conversion. *Nanoscale*. **12**(9), 5261-5285, (2020).

102. Noor, T., L. Yaqoob, and N. Iqbal, Recent Advances in Electrocatalysis of Oxygen Evolution Reaction Using Noble-Metal, Transition-Metal, and Carbon-Based Materials. *ChemElectroChem*. **8**(3), 447-483, (2021).

103. Murthy, A.P., J. Madhavan, and K. Murugan, Recent Advances in Hydrogen Evolution Reaction Catalysts on Carbon/Carbon-Based Supports in Acid Media. *Journal of Power Sources*. **398**9-26, (2018).

104. Huang, Y., K.-D. Seo, K.A. Jannath, D.-S. Park, and Y.-B. Shim, Heteroatoms Doped Carbon Decorated with Tiny Amount Pt Nanoparticles as a Bifunctional Catalyst for Hydrogen and Chlorine Generation from Seawater. *Carbon*. **196**621-632, (2022).

105. Chi, M., B. Luo, Q. Zhang, H. Jiang, C. Chen, S. Wang, and D. Min, Lignin-Based Monolithic Carbon Electrode Decorating with $RuO_2$ Nanospheres for High-Performance Chlorine Evolution Reaction. *Industrial Crops and Products*. **159**113088, (2021).

106. Li, G., J. Yu, W. Yu, L. Yang, X. Zhang, X. Liu, H. Liu, and W. Zhou, Phosphorus-Doped Iron Nitride Nanoparticles Encapsulated by Nitrogen-Doped Carbon Nanosheets on Iron Foam In Situ Derived From Saccharomycetes Cerevisiae for Electrocatalytic Overall Water Splitting. *Small*. **16**(32), 2001980, (2020).

107. Edgington, J., A. Deberghes, and L.C. Seitz, Glassy Carbon Substrate Oxidation Effects on Electrode Stability for Oxygen Evolution Reaction Catalysis Stability Benchmarking. *ACS Applied Energy Materials*(2022).

108. Yi, Y., G. Weinberg, M. Prenzel, M. Greiner, S. Heumann, S. Becker, and R. Schlögl, Electrochemical Corrosion of a Glassy Carbon Electrode. *Catalysis Today*. **295**32-40, (2017).

109. Sivanantham, A., P. Ganesan, and S. Shanmugam, Hierarchical $NiCo_2S_4$ Nanowire Arrays Supported on Ni Foam: An Efficient and Durable Bifunctional Electrocatalyst for Oxygen and Hydrogen Evolution Reactions. *Advanced Functional Materials*. **26**(26), 4661-4672, (2016).

110. Son, Y.J., K. Kawashima, B.R. Wygant, C.H. Lam, J.N. Burrow, H. Celio, A. Dolocan, J.G. Ekerdt, and C.B. Mullins, Anodized Nickel Foam for Oxygen Evolution Reaction in Fe-Free and Unpurified Alkaline Electrolytes at High Current Densities. *ACS Nano*. **15**(2), 3468-3480, (2021).

111. Munnik, P., P.E. de Jongh, and K.P. de Jong, Recent Developments in the Synthesis of Supported Catalysts. *Chemical Reviews*. **115**(14), 6687-6718, (2015).

112. Wang, A., J. Li, and T. Zhang, Heterogeneous Single-Atom Catalysis. *Nature Reviews Chemistry*. **2**(6), 65-81, (2018).

113. Kaiser, S.K., Z. Chen, D. Faust Akl, S. Mitchell, and J. Pérez-Ramírez, Single-Atom Catalysts Across the Periodic Table. *Chemical Reviews*. **120**(21), 11703-11809, (2020).

114. Wang, Y., H. Su, Y. He, L. Li, S. Zhu, H. Shen, P. Xie, X. Fu, G. Zhou, C. Feng, D. Zhao, F. Xiao, X. Zhu, Y. Zeng, M. Shao, S. Chen, G. Wu, J. Zeng, and C. Wang, Advanced Electrocatalysts with Single-Metal-Atom Active Sites. *Chemical Reviews*. **120**(21), 12217-12314, (2020).

115. Xu, H., D. Cheng, D. Cao, and X.C. Zeng, A Universal Principle for a Rational Design of Single-Atom Electrocatalysts. *Nature Catalysis*. **1**(5), 339-348, (2018).

116. Hine, F., M. Yasuda, T. Noda, T. Yoshida, and J. Okuda, Electrochemical Behavior of the Oxide-Coated Metal Anodes. *Journal of The Electrochemical Society*. **126**(9), 1439-1445, (1979).

117. Tian, L., Z. Zhang, S. Liu, G. Li, and X. Gao, High-Entropy Spinel Oxide Nanofibers as Catalytic Sulfur Hosts Promise the High Gravimetric and Volumetric Capacities for Lithium–Sulfur Batteries. *Energy & Environmental Materials*. **5**(2), 645-654, (2022).

118. Qiao, H., X. Wang, Q. Dong, H. Zheng, G. Chen, M. Hong, C.-P. Yang, M. Wu, K. He, and L. Hu, A High-Entropy Phosphate Catalyst for Oxygen Evolution Reaction. *Nano Energy*. **86**106029, (2021).

119. Duan, C., X. Li, D. Wang, Z. Wang, H. Sun, R. Zheng, and Y. Liu, Nanosized High Entropy Spinel Oxide $(FeCoNiCrMn)_3O_4$ as a Highly Active and Ultra-Stable Electrocatalyst for the Oxygen Evolution Reaction. *Sustainable Energy & Fuels*. **6**(6), 1479-1488, (2022).

120. Wang, D., Z. Liu, S. Du, Y. Zhang, H. Li, Z. Xiao, W. Chen, R. Chen, Y. Wang, Y. Zou, and S. Wang, Low-Temperature Synthesis of Small-Sized High-Entropy Oxides for Water Oxidation. *Journal of Materials Chemistry A*. **7**(42), 24211-24216, (2019).

121. Akrami, S., Y. Murakami, M. Watanabe, T. Ishihara, M. Arita, M. Fuji, and K. Edalati, Defective High-Entropy Oxide Photocatalyst with High Activity for $CO_2$ Conversion. *Applied Catalysis B: Environmental*. **303**120896, (2022).

122. Sarkar, A., L. Velasco, D. Wang, Q. Wang, G. Talasila, L. de Biasi, C. Kübel, T. Brezesinski, S.S. Bhattacharya, H. Hahn, and B. Breitung, High Entropy Oxides for Reversible Energy Storage. *Nature Communications*. **9**(1), 3400, (2018).

123. Zheng, Y., Y. Yi, M. Fan, H. Liu, X. Li, R. Zhang, M. Li, and Z.-A. Qiao, A High-Entropy Metal Oxide as Chemical Anchor of Polysulfide for Lithium-Sulfur Batteries. *Energy Storage Materials*. **23**678-683, (2019).

124. Jin, Z., J. Lyu, K. Hu, Z. Chen, G. Xie, X. Liu, X. Lin, and H.-J. Qiu, Eight-Component Nanoporous High-Entropy Oxides with Low Ru Contents as High-Performance Bifunctional Catalysts in Zn-Air Batteries. *Small*. **18**(12), 2107207, (2022).

125. Li, F., G.-J. Zhang, and H. Abe, Low-Temperature Synthesis of High-Entropy $(Mg_{0.2}Co_{0.2}Ni_{0.2}Cu_{0.2}Zn_{0.2})O$ Nanoparticles via Polyol Process. *Open Ceramics*. **9**100223, (2022).

126. SpasojeviĆ, M.D., N.V. KrstajiĆ, and M.M. JakŠIĆ, Optimization of an Anodic Electrocatalyst: $RuO_2/TiO_2$ on Titanium. *Journal Of The Research Institute For Catalysis Hokkaido University*. **31**(2/3), 77-94, (1984).

127. Akbayrak, S., and S. Özkar, Ruthenium(0) Nanoparticles Supported on Multiwalled Carbon Nanotube as Highly Active Catalyst for Hydrogen Generation from Ammonia–Borane. *ACS Applied Materials & Interfaces*. **4**(11), 6302-6310, (2012).

128. Liu, Q.-Y., H.-D. Wang, R. Tang, Q. Cheng, and Y.-J. Yuan, Rutile $TiO_2$ Nanoparticles with Oxygen Vacancy for Photocatalytic Nitrogen Fixation. *ACS Applied Nano Materials*. **4**(9), 8674-8679, (2021).

129. Wang, L., J. Li, Y. Wang, K. Yu, X. Tang, Y. Zhang, S. Wang, and C. Wei, Construction of 1D $SnO_2$-Coated ZnO Nanowire Heterojunction for their Improved N-Butylamine Sensing Performances. *Scientific Reports*. **6**(1), 35079, (2016).

130. Liu, Q., H.Q. Zhan, X.C. Huang, Y.H. Song, S.C. He, X.H. Li, C.A. Wang, and Z.P. Xie, High Visible Light Photocatalytic Activity of $SnO_{2-X}$ Nanocrystals with Rich Oxygen Vacancy. *European Journal of Inorganic Chemistry*. **2021**(42), 4370-4376, (2021).

131. Liardet, L., and X. Hu, Amorphous Cobalt Vanadium Oxide as a Highly Active Electrocatalyst for Oxygen Evolution. *ACS Catalysis*. **8**(1), 644-650, (2018).

132. Chen, G., X. Zhang, L. Guan, H. Zhang, X. Xie, S. Chen, and J. Tao, Phase Transition-Promoted Hydrogen Evolution Performance of $MoS_2/VO_2$ Hybrids. *The Journal of Physical Chemistry C*. **122**(5), 2618-2623, (2018).

133. Kim, K.-H., K.-H. Kim, W. Choi, Y.-M. Kim, S.-H. Hong, and Y.-H. Choi, Mapping the Electrocatalytic Water Splitting Activity of $VO_2$ Across its Insulator-to-Metal Phase Transition. *Nanoscale*. **14**(23), 8281-8290, (2022).

134. Wang, M.H., L.L. Fan, J.M. Bian, D. Zhang, H.Z. Liu, H.J. Sun, and Y.M. Luo, Room-Temperature Metal-Insulator Transition of MBE Grown $VO_2$ Film Investigated by

Temperature Dependent Resistance and Transmittance. *Journal of Materials Science-Materials in Electronics*. **28**(15), 11046-11052, (2017).

135. Ni, J., J. Gao, X. Geng, D. He, and X. Guo, Controllable Synthesis of $TiO_2$ Nanoflowers and Their Morphology-Dependent Photocatalytic Activities. *Applied Physics A*. **123**(3), 186, (2017).

136. Wang, Y.T., H.J. Li, W. Zhou, X. Zhang, B. Zhang, and Y.F. Yu, Structurally Disordered $RuO_2$ Nanosheets with Rich Oxygen Vacancies for Enhanced Nitrate Electroreduction to Ammonia. *Angewandte Chemie-International Edition*. **61**(19), (2022).

137. Tian, Y., S. Wang, E. Velasco, Y. Yang, L. Cao, L. Zhang, X. Li, Y. Lin, Q. Zhang, and L. Chen, A Co-Doped Nanorod-Like $RuO_2$ Electrocatalyst with Abundant Oxygen Vacancies for Acidic Water Oxidation. *iScience*. **23**(1), 100756, (2020).

138. Anantharaj, S., S. Kundu, and S. Noda, Worrisome Exaggeration Of Activity Of Electrocatalysts Destined For Steady-State Water Electrolysis By Polarization Curves From Transient Techniques. *Journal of the Electrochemical Society*. **169**(1), (2022).

139. Sukkurji, P.A., Y. Cui, S. Lee, K. Wang, R. Azmi, A. Sarkar, S. Indris, S.S. Bhattacharya, R. Kruk, H. Hahn, Q. Wang, M. Botros, and B. Breitung, Mechanochemical Synthesis of Novel Rutile-Type High Entropy Fluorides for Electrocatalysis. *Journal of Materials Chemistry A*. **9**(14), 8998-9009, (2021).

140. Chen, A., S. Xia, Z. Ji, and H. Lu, Insights into the Origin of Super-High Oxygen Evolution Potential of Cu Doped $SnO_2$ Anodes: A Theoretical Study. *Applied Surface Science*. **471**149-153, (2019).